Hybrid Organic-Inorganic Materials Synthesized via Vapor Phase Infiltration

A Ph.D. Dissertation
Presented to
The Academic Faculty

By

Collen Leng

In Partial Fulfillment
Of the Requirements for the Degree
Doctor of Philosophy in the
School of Materials Science and Engineering

Georgia Institute of Technology

December, 2018

Hybrid Organic-Inorganic Materials Synthesized via Vapor Phase Infiltration

Approved by:

Dr. Mark D. Losego, Advisor
School of Materials Science and Engineering
Georgia Institute of Technology

Dr. Matthew McDowell
School of Mechanical Engineering
Georgia Institute of Technology

Dr. Karl Jacob
School of Materials Science and Engineering
Georgia Institute of Technology

Dr. Samuel Graham
School of Mechanical Engineering
Georgia Institute of Technology

Dr. Zhiqun Lin
School of Materials Science and Engineering
Georgia Institute of Technology

Date Approved: August 30, 2018

ACKNOWLEDGMENTS

To Dr. Mark Losego, for selecting me as one of his original two graduate students in his newly formed research group at Georgia Tech in 2014, and for teaching me how to think and write quality research throughout the years.

To the entire Losego Lab, for helping me and each other with our research needs, and for making graduate school an exciting and fun experience.

To my family and friends, for supporting me through both good and difficult times. I am blessed to have known each and every one of you.

To Sophie Wang, my fiancée, for bringing me so much laughter and happiness every day and teaching me to become a better man. I will love you always.

This work is financially supported by start-up funds for the Losego Lab as well as the Petroleum Research Fund from the American Chemical Society.

TABLE OF CONTENTS

LIST OF TABLES

LIST OF FIGURES

LIST OF ABBREVIATIONS

ALD	Atomic Layer Deposition
BCP	Block Co-Polymer
CF	Conflat Flange
CVI	Chemical Vapor Infiltration
DEZ	Diethyl Zinc
EDS/EDX	Energy-Dispersive X-Ray Spectroscopy
EELS	Electron Energy Loss Spectroscopy
FIB	Focused Ion Beam
FTIR	Fourier Transform Infrared Spectroscopy
IPA	Isopropanol
KF	Klein Flange / Quick Flange
MPI	Multiple Pulsed Infiltration
P3HT	Poly(3-Hexylthiophene-2,5-Diyl)
PA-6	Polyamide-6
PCBM	Phenyl-C61-Butyric Acid Methyl Ester
PE	Polyethylene
PID	Proportional-Integral-Derivative
PLA	Polylactic Acid
PMMA	Poly(Methyl Methacrylate)
PP	Polypropylene
PS	Polystyrene

PS-r-PHEA	Poly(Styrene-co-2-Hydroxyethyl Acrylate)
PVA	Polyvinyl Alcohol
PVC	Polyvinyl Chloride
QCM	Quartz Crystal Microbalance
SEM	Scanning Electron Microscopy
SIMS	Secondary Ion Mass Spectrometry
SIS	Sequential Infiltration Synthesis
STEM	Scanning Transmission Electron Microscopy
SVI	Sequential Vapor Infiltration
TEM	Transmission Electron Microscopy
TGA	Thermogravimetric Analysis
THF	Tetrahydrofuran
$TiCl_4$	Titanium Tetrachloride
TIP	Titanium Isopropoxide
TMA	Trimethylaluminum
UGA	University of Georgia
VPI	Vapor Phase Infiltration

SUMMARY

Polymers are used in a wide range of applications, from high-tech devices to everyday products, yet they suffer from limitations such as poor chemical stability in certain environments and low mechanical strength. Inorganic materials like silicon and glass have higher mechanical strength, but they are heavier and more brittle as well as more susceptible to certain chemical degradations. For example, polymers are easily dissolved in organic solvents whereas inorganics like glass remain stable, but glass can be etched by hydrofluoric acid, to which some polymers are immune. By incorporating inorganic constituents into these materials, we can bring about the best of both worlds in terms of new properties that might not be offered by either material alone.

This thesis presents a processing theory created from experimental measurements to allow precise control of vapor phase infiltration (VPI) used to create new organic-inorganic hybrid materials. VPI works by allowing metalorganic precursors commonly used in chemical vapor deposition to diffuse into polymers and react with polymer functional groups or co-reactants at low processing temperatures (below 200 ^{o}C). This process can transform nanometers to microns of polymer into hybrid material. While several research groups have explored various materials properties of VPI-modified polymers, the research community still does not understand the exact processing kinetics and thermodynamics of VPI. By using *ex situ* and *in situ* characterization techniques, we calculate energy parameters for VPI processing kinetics and thermodynamics for the commonly studied trimethylaluminum and poly(methyl methacrylate) system. This thesis also presents new properties in the hybrid materials including chemical stability and

water absorption that provides more insight about the chemical and physical structure of these materials.

This thesis provides new knowledge to help guide the hybrid materials research community towards developing new processes and materials through vapor phase infiltration for both fundamental scientific studies and commercial products.

1. INTRODUCTION

This chapter begins with a brief history of vapor phase infiltration and a discussion of nomenclature found in the literature for this process. Next, it describes the physiochemical factors affecting VPI processes such as free volume of polymers and reactivity between polymers and precursors. Considering these physiochemical factors, we set up a processing theory based on vapor-sorption thermodynamic equilibrium, Fickian diffusion, and reaction equilibrium that can extract relevant energy parameters from each individual step within a general VPI process: sorption, diffusion, and reaction.

This chapter then presents characterization methods used to study the VPI process and hybrid materials created. These methods include quartz crystal microbalance (QCM) gravimetry, FTIR spectroscopy, ellipsometry, and cross-sectional scanning electron microscopy. The chapter concludes with an overview of applications from materials transformed by VPI. These new applications include improved 3D imaging, strengthened mechanical properties, and improved electronic transport in polymer solar cells.

1.1. VPI Overview

Most organic-inorganic hybrid materials are currently produced via liquid chemical solution methods.[1-7] In the mid-2000's, a new approach emerged in which organic polymers were exposed to gaseous metalorganic precursors that diffuse and react within the polymer to transform the polymers into a hybrid material. Examples of metalorganic precursors used for this VPI process include trimethylaluminum (TMA), diethyl zinc (DEZ), and titanium tetrachloride ($TiCl_4$). Following the exposure to precursors, co-reactants like water can be introduced to react with precursors inside the polymer and physically trap precursors via steric hindrance. This process originated from researchers in 2004 attempting to use atomic layer deposition (ALD) to deposit thin (< 10 nm), conformal, inorganic films on the surface of polymeric materials.[8] It was soon discovered

that, unlike inorganic substrates, polymers were porous to many of ALD's gas phase precursors. The cyclic dosing of ALD precursors permitted sufficient time for these gaseous chemicals to diffuse into the polymer and become trapped below the surface (sub-surface deposition). At the time, this result was inconvenient, and schemes were developed (e.g., the use of plasma treatments) to activate the surfaces of chemically inert polymers, like polyethylene (PE) and polypropylene (PP), with reactive groups, like hydroxyls, to accommodate more ideal layer-by-layer ALD film growth from the polymer surface. However, other researchers saw potential opportunity in this "vapor phase infiltration" (VPI) process for producing unique organic-inorganic hybrid materials.[9-12]

In 2009, the Knez group published a seminal paper for the field, describing how VPI could enhance the mechanical strength and toughness of spider dragline silks.[9] This demonstration of VPI as a means to enhance the properties of polymeric materials initiated a surge of exploratory research that continues today. Since 2009, various researchers have demonstrated enhanced properties using VPI generated organic-inorganic hybrid materials, including stronger cellulosic fibers,[10] more etch-tolerant photoresists,[11] and more efficient hybrid solar cells.[12]

1.1.1. VPI Nomenclature

Vapor phase infiltration currently suffers from a lack of identity. Today's literature is interspersed with various terminologies describing effectively the same process. Examples include: *"Multiple Pulsed Infiltration" (MPI),*[9, 13] *"Sequential Infiltration Synthesis" (SIS),*[11, 14-16] *and "Sequential Vapor Infiltration" (SVI).*[17-19] While these processes are differentiated by precursor dosing sequence, the atomic-level mechanisms are essentially the same. Each process entails diffusing inorganic precursor molecules into a polymer and then entrapping them in the solid. While gas delivery pulse times, hold times, and cycle repetitions may vary, we argue that these processes ultimately yield similar — *if not identical*— material, albeit the volume transformed may be different. Thus, we propose unifying the nomenclature. *We suggest the name* ***"Vapor Phase***

Infiltration (VPI)" *because of its simplicity and its ability to capture the fundamental phenomenology of this process.* Establishing a single nomenclature will bring together the community and consolidate research efforts towards developing a universal understanding of the processing chemistry, thermodynamics, and kinetics. Practically, it will also simplify literature searches for this topic, bringing more unified and broader exposure to this important emerging processing technology.

It is worth noting that some similarities exist between VPI and Chemical Vapor Infiltration (CVI). CVI is a processing technique whereby metalorganic vapors are permeated through fibrous ceramic or carbon preforms to produce ceramic matrix composites.[20-21] However, CVI and VPI vary sufficiently in precursor transport mechanisms (CVI undergoes convective or Knudsen flow versus VPI's solution diffusion), precursor delivery sequencing, and processing temperatures. These differences preclude any co-categorization.

1.1.2. Taxonomy of VPI Based on Processing Kinetics

Vapor phase processing of materials is commonly divided into physical vapor methods and chemical vapor methods. Physical vapor methods use physical means (thermal energy, ablation, irradiation, etc.) to create mostly elemental vapors for deposition. Chemical vapor methods employ volatile chemical compounds for processing. **Figure 1** presents a classification scheme that uses differences in atomic scale processing kinetics to sub-divide chemical vapor phase processing into three important classes: (1) chemical vapor deposition (CVD), (2) atomic layer deposition (ALD), and (3) vapor phase infiltration (VPI). While this diagram is not intended to be comprehensive (e.g., CVI could likely be added as a fourth class), it is useful to understand how VPI and its subclasses fit into the larger chemical vapor processing family.

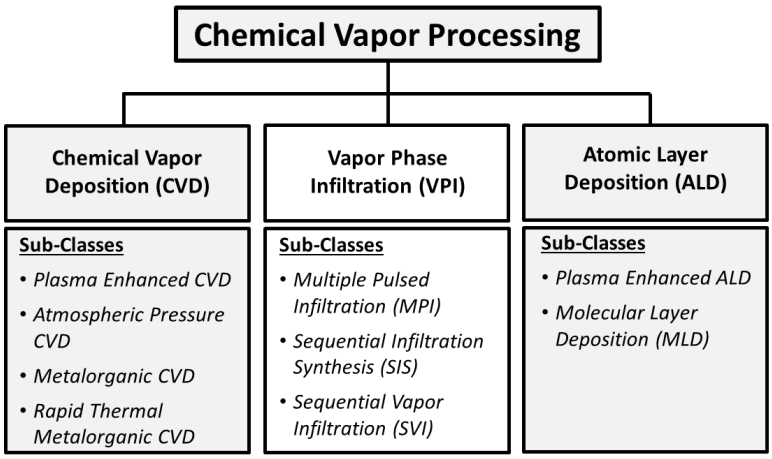

Figure 1: *Diagram for the taxonomy of chemical vapor phase processing based upon atomic-scale processing kinetics (3 main classes) and variations in processing conditions (sub-classes).*

CVD is likely the most common of the chemical vapor processing methods. CVD is accomplished via gas phase diffusion and reaction of precursor(s) near a surface, resulting in the deposition of a coating (film) on the surface.[20] CVD has many sub-classes including metalorganic chemical vapor deposition (MOCVD), atmospheric pressure chemical vapor deposition (APCVD), and plasma enhanced chemical vapor deposition (PECVD). These subclasses can be thought to arise from differences in processing conditions (e.g., precursor chemistry, deposition pressure, energy activation mechanism, wall temperature, etc.), not the fundamental atomic-scale processing kinetics. A second class of chemical vapor processing is ALD. In ALD, a material is again deposited as a coating (film), but through sequential delivery of gas phase precursors, restricting reactions to surface sites in a self-limited (single "monolayer") manner.[22-26] ALD also has sub-classes reflective of differences in processing conditions or precursor types, like plasma enhanced ALD[27-29] and molecular layer deposition.[30-31] While ALD and VPI share a similar processing scheme—one that temporally separates the delivery of precursors—bulk diffusion of precursors into the subsurface of the substrate is unique to VPI. As pictured in **Figure 2**, precursor diffusion through the polymer is a critical step in the VPI process. A typical VPI process includes (1) sorption of the gas phase precursor into the polymer, (2) diffusion of the precursor within the bulk polymer, and (3)

entrapment of the precursor within the polymer. The resulting "deposition" of VPI is also distinct from ALD and CVD. Rather than depositing a coating (film) on the surface of a material, VPI "infuses" new constituents into the sub-surface or even the bulk of a material. Like CVD and ALD, the published reports of different processing schemes for VPI (like MPI, SIS, and SVI) could be considered sub-classes of VPI.

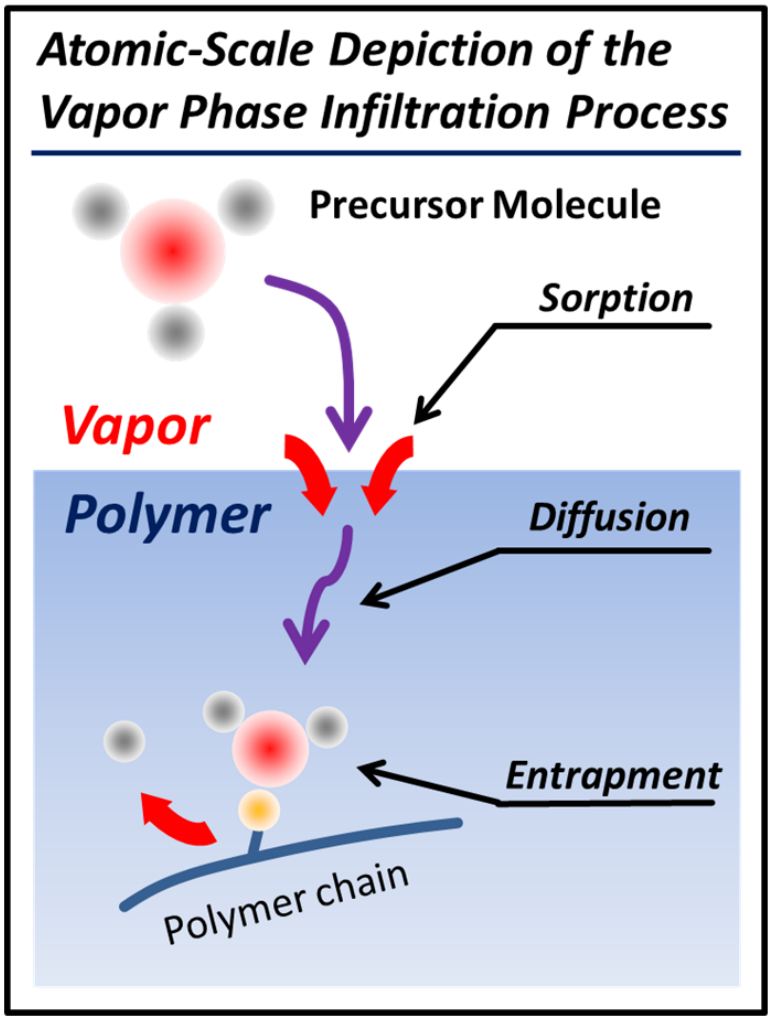

Figure 2: *Schematic for a typical vapor phase infiltration (VPI) process.*

1.1.3. Processing Sequences for Vapor Phase Infiltration

The importance of bulk diffusion in VPI necessitates prolonged exposure of polymeric materials to gaseous precursors. To achieve this prolonged exposure, “holds” are added to the processing sequence. These holds are often accomplished by isolating the deposition chamber in a static gas environment. This sequencing of doses and holds is one way to sub-classify VPI processes. Different dosing sequences commonly discussed in the literature are schematically depicted in **Figure 3**. These sequences typically include exposure to two precursors, often a metalorganic and a co-reactant (like the oxidant water or the reducing agent SiH_4), although other sequences of one, three, or more precursors are conceivable. To be consistent with current literature, VPI subclasses are briefly reviewed in the following sections. However, as the understanding of the chemical mechanisms and processing kinetics for VPI mature, new classification schemes should be developed to provide insight about VPI process design. For example, classification schemes based upon the fundamental understanding of precursor-polymer reaction pathways, precursor entrapment mechanisms, or kinetic rate limiting steps would better inform the design of VPI processes for new classes of materials.

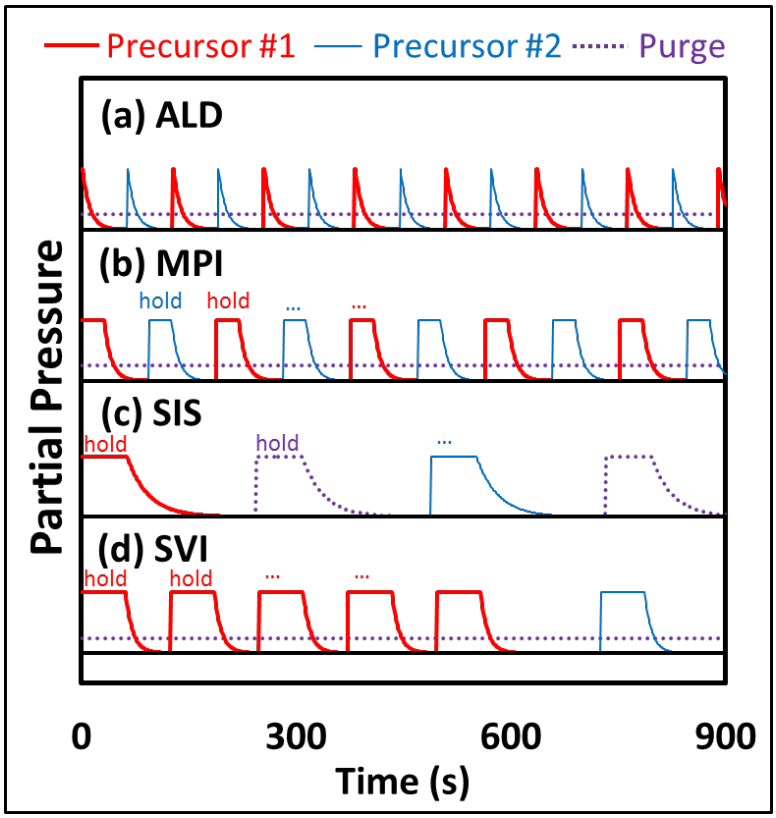

Figure 3: *Schematic of the partial pressure profiles for various precursor pulsing sequences used for vapor phase infiltration: (a) atomic layer deposition (ALD); (b) Multiple Pulsed Infiltration (MPI); c) Sequential Infiltration Synthesis (SIS); and (d) Sequential Vapor Infiltration (SVI). The red (thin), blue (thick), and purple (dotted) lines represent partial pressures of precursor #1, precursor #2 (co-reactant), and carrier/purge gas, respectively. A flat purple line indicates continuous presence of carrier gas. Note that this carrier gas is even present during hold steps as a static partial pressure background. Only for cases like SIS, where active pumping is used, is purge gas fully removed from the reaction environment. The black baselines represent background vacuum pressure or effectively zero partial pressure.*

i. Atomic Layer Deposition on Polymers

Figure 3a depicts the prototypical ALD dosing sequence. Precursors are sequentially introduced at defined time intervals that are temporally separated. These precursors join an inert gas stream that continuously flows reactants and byproducts through the reactor. Gas flow is never stagnant. Applied to an impermeable inorganic substrate, this process deposits a thin film coating onto the material's surface, but when applied to many organic polymers, vapors begin to permeate the subsurface of the substrate. While likely not the

"optimal" processing scheme for VPI, ALD-type sequencing can lead to vapor phase infiltration of polymers.[8, 32-34] The short precursor exposure times and continuous purging from the ALD process limit diffusion distances, resulting in typically shallow infiltration of inorganic species.

ii. Multiple Pulsed Infiltration (MPI)

Figure 3b depicts the multiple pulsed infiltration (MPI) dosing scheme. MPI is similar to ALD with an added "hold" step. During this hold step, the reaction chamber is isolated in a non-flowing mode, permitting direct exposure to a static atmosphere containing the precursor gas. A general dosing schedule is: dose precursor / hold / purge / dose co-reactant / hold / purge. These steps may then be repeated multiple times. Hold steps for MPI processes are usually less than 60 s.[9, 35-36]

The MPI process was introduced by the Knez group in 2009.[9] Initial studies examined the use of MPI to form metallic crosslinks in spider silk using diethylzinc (DEZ), trimethylaluminum (TMA), and titanium isopropoxide (TIP).[9, 36] Subsequent studies have used MPI to infiltrate collagen membranes with metals (Al, Ti, and Zn).[13] The Parsons group effectively used an MPI scheme to study precursor chemistry inside various polymers as well as mechanical behaviors of infiltrated polymers.[37-38] however, in these reports, the process is simply described as a modified ALD sequence.

iii. Sequential Infiltration Synthesis (SIS)

In 2011, Elam and colleagues introduced sequential infiltration synthesis (SIS, **Figure 3c**).[39] Precursors and co-reactants undergo static hold steps similar to MPI but at the conclusion of each hold step, the chamber is fully evacuated to baseline vacuum (typically ~20 mTorr) and then refilled with an inert carrier gas (usually nitrogen). Each dose and purge step usually takes several minutes, with a single SIS cycle possibly lasting more than one hour. SIS has been used to infiltrate polystyrene-*block*-poly(methyl methacrylate) (PMMA) with TMA/H_2O, TMA/tri(tert-pentoxyl) silanol, DEZ/H_2O, and photoresist films with TMA/H_2O.[11, 14-15]

iv. Sequential Vapor Infiltration (SVI)

Sequential vapor infiltration (SVI) was introduced by the Parsons group in 2011.[17] Unlike the two prior methods, SVI repetitively delivers the same precursor via multiple dose steps before exposing the co-reactant. As depicted in **Figure 3d**, pulses are often held for short hold periods of about 30 to 60 seconds as a means to study saturation limits.[17-18, 40] For example, Padbury and Jur used SVI to gravimetrically study TMA uptake in a variety of poly-*n*-methacrylates and polyesters.[34] When the polymer becomes fully saturated, subsequent pulses cause no further change in polymer mass. SVI has also been used in the modification of PDMS and polyester fibers.[17, 41]

1.2. Physiochemical Features Affecting VPI Processing

Three key physiochemical features likely contribute to the sorption, diffusion, and entrapment of gaseous precursor molecules within a polymer during VPI processing: (1) size of the precursor penetrant molecule, (2) free volume of the polymer, and (3) reactivity between precursor and polymer functional groups. The following sections review what is known about how each of these parameters affects the VPI process.

1.2.1. Penetrant Size and Shape

Molecular size and shape likely affect dissolution and diffusion of penetrant molecules in polymers. In 1982, Berens and Hopfenberg[42] conducted fundamental studies of the diffusion rates for differently sized and shaped gaseous molecules in amorphous polymer (e.g., PS, PMMA, and PVC) below their glass transition temperature (T_g). These studies found that the diffusion constant for spherical-shaped molecules (like the noble gases, methane, and SF_6) follow an exponentially decreasing trend with increasing molecular diameter. **Figure 4** reproduces the data for molecular diffusivities in PMMA at 90^o C as a function of the penetrant's mean diameter. The log-linear decrease in diffusion coefficient with increasing molecular size implies a linear increase in diffusion activation energy.[42] A few molecules, like CO_2 and *n*-C_5H_{12}, exhibit higher than expected diffusion

coefficients than their average diameter. These molecules have non-spherical shapes, suggesting that anisometric penetrants preferentially can align themselves with diffusion pathways to potentially enhance diffusion rates.

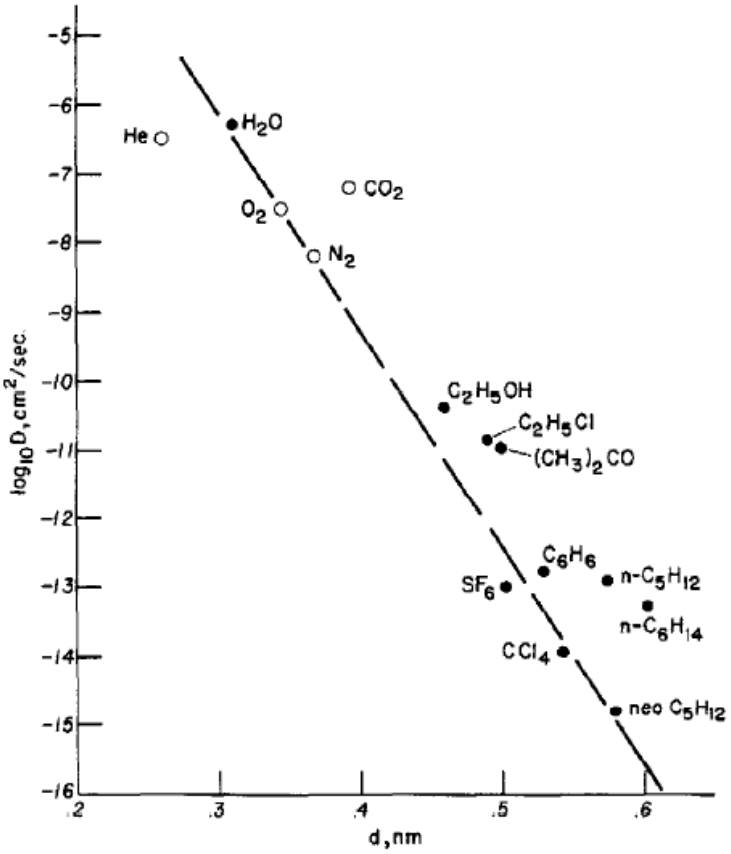

Figure 4: *Measured diffusivities of small molecules in PMMA at 90 ^oC as a function of mean diameter. The slope of the fitted line is proportional to the diffusional activation energy.*[42]

1.2.2. Polymer Free Volume

Atoms pack less densely in amorphous materials than crystalline materials. The atomic-scale porosity generated due to poor atomic packing in amorphous solids is known as "free volume". Free volume in amorphous polymers is the result of bonding constraints and entropic effects that restrict close-packing of the atomic structure. This free volume

can be considered the enabler of small molecule diffusion in "fully dense" polymeric materials.[43]

Figure 5a plots the specific volume (volume per mass) of an amorphous polymer above and below its glass transition temperature (T_g). Note that an increase in specific volume indicates a decrease in mass density (ρ). The specific free volume can be split into (1) the polymer chain volume (red shaded portion) and (2) the free volume (orange shaded portion). At all temperatures the polymer chain volume portion of the specific volume increases monotonically with temperature due to increasing thermal vibrations. Below T_g, the free volume portion of specific volume remains constant. Above T_g, this free volume portion increases rapidly, faster than the chain volume portion. The fractional free volume of a polymer above T_g (i.e., fraction of total specific volume that is free volume, v_{f0}) can be expressed by **Equation 1**.[44]

$$v_{f0} = v_{f0,Tg} + \Delta\alpha\left(T - T_g\right) \qquad \textbf{Equation 1}$$

where $v_{f0,Tg}$ is the fractional free volume at T_g, and Δα is the difference between the thermal expansion coefficient of the polymer above and below T_g.

By adjusting the cooling rate or quench temperature, "kinetic trapping" of free volume is possible. Once the polymer is quenched below T_g, polymer chains "freeze" into a non-equilibrium state with a fixed free volume. The quantity of this free volume depends upon prior processing history.[43, 45] **Figure 5b** demonstrates how quenching an amorphous polymer from different melt temperatures can adjust the fixed fractional free volume. The "fictive temperature" is used to describe differences in fractional free volume of a given amorphous polymer below T_g. A glassy polymer with a fictive temperature T_f will effectively have the same fractional free volume as a rubbery polymer of temperature T_f above T_g. Thus, higher fictive temperature glasses will have greater fractional free volumes, and thus, by quenching polymer glasses from different fictive temperatures it would be possibly to generate polymers of varying free volume below T_g. For reference, the T_g for a number of polymers typically used with VPI processing are summarized in **Table 1**.

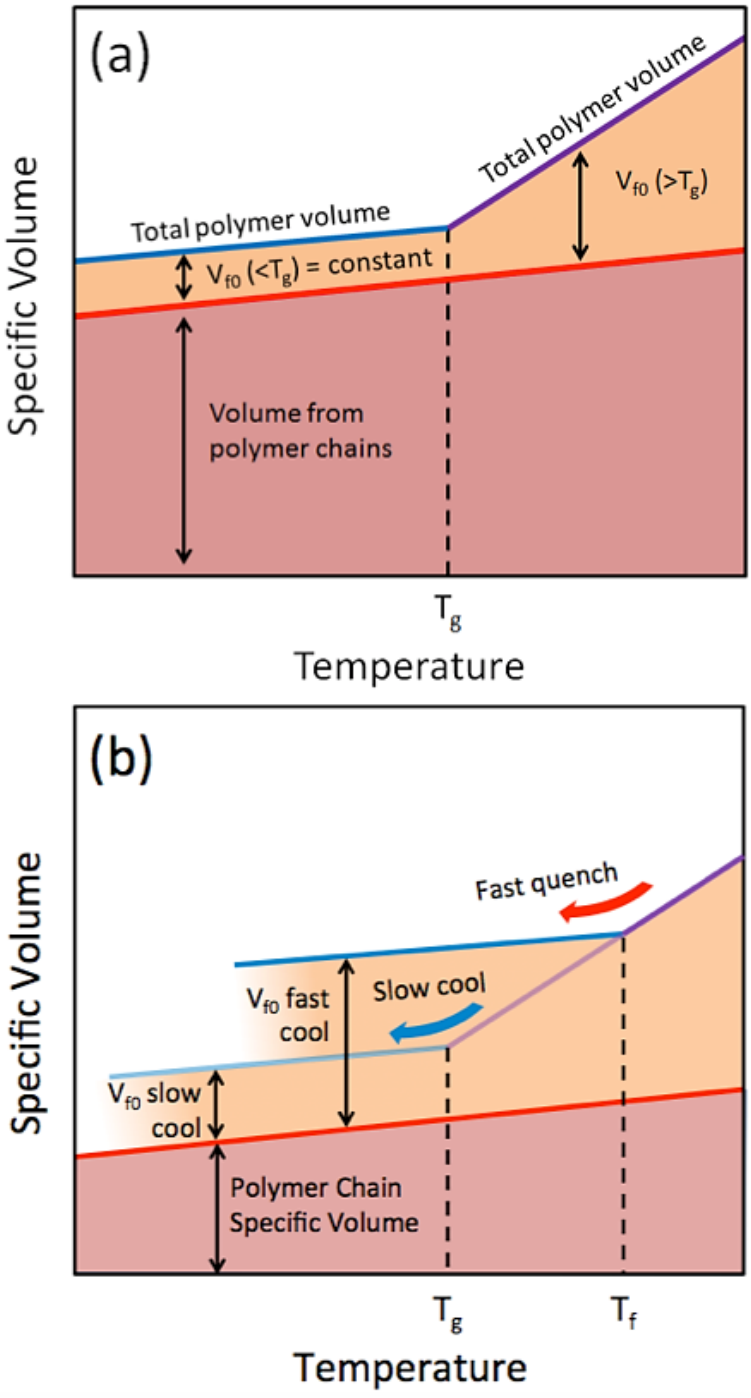

Figure 5: *(a) Schematic plot for the specific volume of a glassy polymer as a function of temperature. Fractional portions of the specific volume are split into the polymer chain volume (red area) and the free volume (orange area). (b) Schematic showing how process conditions (cooling rate and quench temperature) can be used to alter the fractional free volume (V_{f0}) of a glassy polymer below T_g.*

Table 1: *Glass transition temperature of common polymers used for VPI.*

Polymer	**T_g (^oC)**	**Reference**
Polypropylene (PP)	-10	[33]
Poly(butyl methacrylate) (PBMA)	15	[34]
Poly(propyl methacrylate) (PPMA)	35	[34]
Polyamide-6 (PA6)	50	[33]
Poly(ethyl methacrylate) (PEMA)	65	[34]
Polybutylene terephthalate (PBT)	66	[34]
Polyethylene terephthalate (PET)	80	[34]
Polyvinyl alcohol (PVA)	85	[33]
Poly(methyl methacrylate) (PMMA)	115	[34]

In relation to VPI processing, fractional free volume contributes to the precursor diffusion kinetics. Above T_g, the dramatic increase in fractional free volume and enhanced polymer chain motion facilitate more rapid diffusion rates. Below T_g, arrested polymer chain motion and smaller fractional free volumes impede precursor diffusion.

1.2.3. Precursor-Polymer Reactivity

Reactivity between precursor and polymer is critical to determining the mechanism and kinetics of a VPI process. If the precursor chemistry is unreactive towards the polymer, then the VPI kinetics reduce to a purely diffusional process. This case is common for inert polymers like polypropylene and polystyrene. However, when the polymer contains more reactive functional groups like carbonyls or amides, the VPI processing kinetics become a convolution of diffusion and reaction rates. Chemical binding of inorganic precursors to the polymer will also alter the chemical structure and may disrupt subsequent penetrant diffusion.

Reaction rates are also enormously temperature dependent. As process temperature increases, reaction rates increase and gaseous precursors become more likely to react near the polymer's surface. This reacted surface layer can act as a barrier to subsequent diffusion. Sun *et al.*[46] experimentally investigated this phenomenon for VPI of polyamide-6 (PA6, nylon) films with TMA. Electron micrographs illustrating the differences in reaction layers formed at different VPI process temperatures are shown in **Figure 6**. At low temperatures (60 °C) a large sub-surface reaction region with a depth of 120 nm is observed. As temperature increases, the carbonyl groups become more reactive towards TMA and this organic-inorganic hybrid region reduces in thickness. By 120 °C, gaseous precursors immediately react with surface carbonyls, preventing any significant subsurface reaction. Subsequent cycles lead to growth of Al_2O_3 film only on the surface of the fiber. Thus, for modestly reactive polymer-precursor combinations, three VPI processing regimes have been proposed to exist: (1) a diffusion controlled growth regime at low process temperatures, (2) a reaction controlled growth regime at high process temperatures, and (3) a more complicated process regime that depends on both diffusional and reaction kinetics at Intermediate temperatures. **Figure 6d** shows gravimetric measurements of mass gain for PA-6 nylon exposed to TMA at varying VPI process temperatures.[47] Similar to the cross-sectional imaging, this gravimetric analysis indicates less mass gain at higher VPI temperatures, indicating that precursors only react on the surface of the material. At lower VPI process temperatures (30 °C), mass gain is greater because reaction rates are slower and precursors are given the opportunity to permeate the polymer matrix.

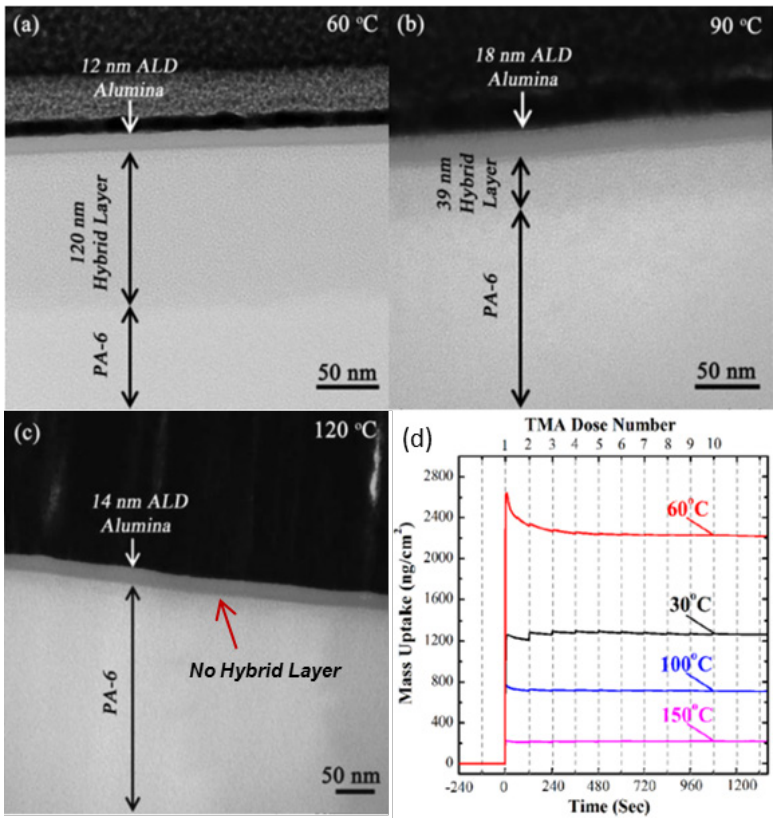

***Figure 6**: Scanning electron microscopy images of PA-6 films vapor phase infiltrated with TMA at varying temperatures: (a) 60 °C, (b) 90 °C, and (c) 120 °C[46] and (d) in situ gravimetric measurements of mass uptake during TMA VPI of PA-6 at varying temperatures.*[47]

1.3. VPI Theory and Kinetics Model

As previously depicted in **Figure 2**, the three key steps in VPI processing are: (1) **sorption** (or dissolution) of a gaseous (usually metalorganic) precursor molecule into an organic (usually polymeric) solid, (2) **transport** (diffusion) of that molecular species into the polymer's matrix and (3) **entrapment** (often through a reaction) of that precursor within the bulk polymer. This section will examine the atomic scale mechanisms and physical and chemical parameters that affect each of these processing steps.

1.3.1. Sorption of Gas Molecules into Polymers

The first step of the VPI process is sorption of the vapor phase molecular precursor into the polymer. Thermodynamically, the concentration (C) of a penetrant (precursor) molecule in a polymer depends upon the partial pressure (P) of that penetrant species and the solubility coefficient (S), via: C = SP (Henry's Law). Here we assume that the low pressures of VPI (< 1 Torr) keep the system sufficiently dilute that Henry's Law is sufficient to describe the sorption equilibrium. Because S is essentially the equilibrium reaction constant for sorption, it scales exponentially with temperature (T) according to the Van't Hoff relationship:

$$S = S_o \exp\left(-\frac{\Delta H_S}{kT}\right) \qquad \textbf{Equation 2}$$

where S_o is a temperature-independent constant based upon the change in entropy for this reaction, k is Boltzmann's constant, and ΔH_S is the enthalpy of sorption. Thus, when the natural log of the solubility coefficient is plotted versus the inverse of absolute temperature, the slope of this line is proportional to ΔH_S. The maximum solubility at a given temperature can be used in subsequent diffusion calculations as the "maximum concentration" (C_{max}) of source precursor at the polymer surface and can also be related to the total mass uptake at infinite time, M_∞ (*vide infra*).

1.3.2. Diffusion of Gas Molecules within Polymers

The gas membrane separations community subdivides transport of gaseous species through polymer films into four primary categories: 1) viscous flow, 2) Knudsen diffusion, 3) molecular sieving, and 4) solution-diffusion.[48-49] Each of these methods is depicted in **Figure 7**. The first three methods are primarily driven by pressure gradients, while solution-diffusion is also driven by chemical potential gradients.[48-49] Once the gas molecule enters the polymer, it is referred to as a "penetrant". In viscous flow and Knudsen diffusion, penetrant molecules enter the polymer through "macro-scale" porosity, making these mechanisms of minimal importance for most VPI processes.

Viscous flow occurs when the pore size is greater than the gas's mean free path (on the order of 0.1 μm or greater), resulting in gas flow similar to fluid flow through macro-scale tubes. As the pore radius shrinks below the size of the gas's mean free path, Knudsen diffusion becomes dominant. In the Knudsen diffusion regime, molecules move independently because molecule-molecule collisions are rare.[48] Molecular sieving occurs when pore sizes approach the size of the gas molecule penetrant (pore sizes approach a few nanometers). While molecular sieving may be important for some VPI processes, solution-diffusion is likely the most common gas penetrant transport method. Solution-diffusion occurs in "fully dense" polymers and relies upon a combination of both gas molecule dissolution and diffusion. Unlike the other three transport mechanisms, solution-diffusion relies on physiochemical interactions between the diffusing molecules and the bulk material.[48]

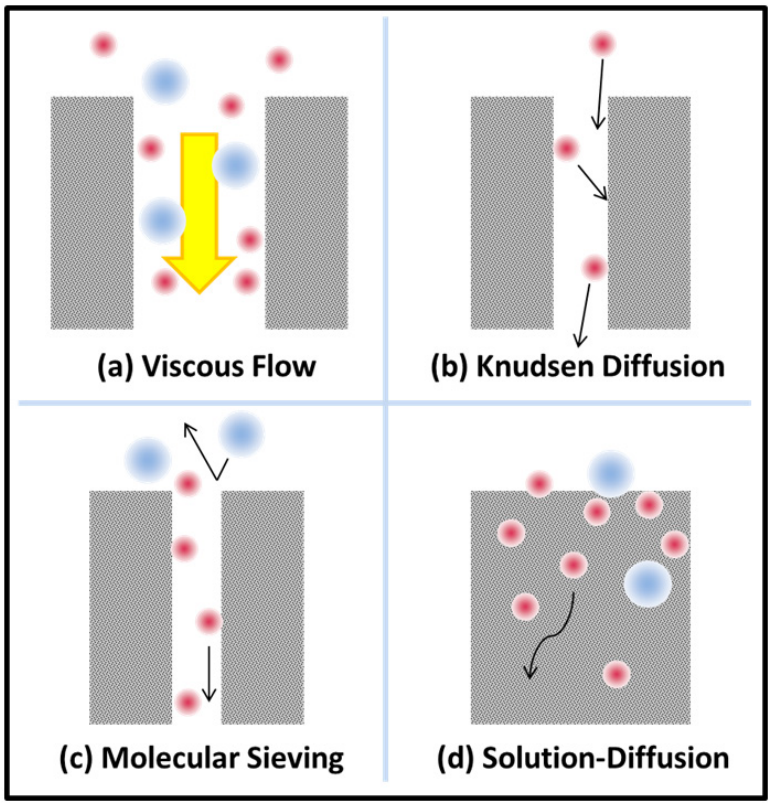

Figure 7: *Depiction of the four primary methods of gas transport through polymer membranes or thin films: a) Viscous flow, b) Knudsen diffusion, c) molecular sieving, and*

d) solution-diffusion. The red and blue circles represent two gaseous species of different sizes, and arrows indicate the direction of gas transport.

The steady-state flux (J) of gas penetrant molecules across a polymer film of thickness (t) is described by Fick's 1st Law:

$$J = -D\frac{(C_2 - C_1)}{t} \qquad \textbf{Equation 3}$$

where D is the diffusivity of the penetrant, $(C_2 - C_1)$ is the concentration gradient across the film, and t is the film's thickness. For a solution diffusion process, concentrations can be substituted with the equilibrium vapor pressures according to Henry's Law, giving:

$$J = -D\frac{S(p_2 - p_1)}{t}. \qquad \textbf{Equation 4}$$

This equation suggests that a new proportionality constant can be defined to relate the diffusing flux to the pressure gradient for a solution-diffusion process. This new proportionality constant is known as the permeation coefficient or permeability (P) of the material:

$$P = D \cdot S. \qquad \textbf{Equation 5}$$

In gas membrane separations research, the permeability of polymer membranes is intently studied to understand gas transport phenomena:

$$J = -P\frac{(p_2 - p_1)}{t}. \qquad \textbf{Equation 6}$$

The permeability of a material can thus be found by measuring the flux across a film with a pressure gradient. The permeability of a material — that is the combined sorption and diffusion properties for a given precursor-polymer couple — is likely of critical importance when designing a VPI process.

1.3.3. Mathematical Framework for VPI Diffusion Model

Precursor diffusion for VPI can be described by Fick's 2nd Law for time-dependent diffusion:

$$\frac{\partial C}{\partial t} = D\frac{\partial^2 C}{\partial x^2} \qquad \textbf{Equation 7}$$

where D is the diffusion coefficient, x is the distance into the film, and t is time. For our experiments, we solve this equation for the case of 1-dimensional diffusion into a film with an impermeable substrate.[50] However, once the diffusional activation energy is measured, Fick's 2nd Law can readily be solved for any diffusional geometry.[51] Initial conditions include zero precursors inside the polymer at time (t) less than zero ($t < 0$) and fixed precursor concentration outside of the polymer for $t \geq 0$. The boundary conditions include (1) no mass flux at the polymer/substrate interface (impermeable substrate) and (2) an unlimited supply of vapor phase precursors at the polymer surface, allowing the saturation concentration (i.e., solubility limit) of precursor ($C_{max} = S \cdot p$) to be retained. The thin film geometric conditions considered are shown in **Figure 8**.

The boundary/initial conditions for 1D diffusion depicted in **Figure 8** are:

$$C(0,t) = C_{\max} \qquad \textbf{Equation 8a}$$

$$\frac{\partial C}{\partial x}(L,t) = 0 \qquad \textbf{Equation 8b}$$

$$C(x,0) = 0. \qquad \textbf{Equation 8c}$$

Here, position 0 is the polymer film surface, L is the film thickness, position L is the polymer/substrate interface, and time 0 is when the polymer surface is initially exposed to the gaseous precursor. These conditions are analogous to a heat diffusion model where one side of the film is exposed to a fixed temperature and the other side is a perfect thermal insulator.

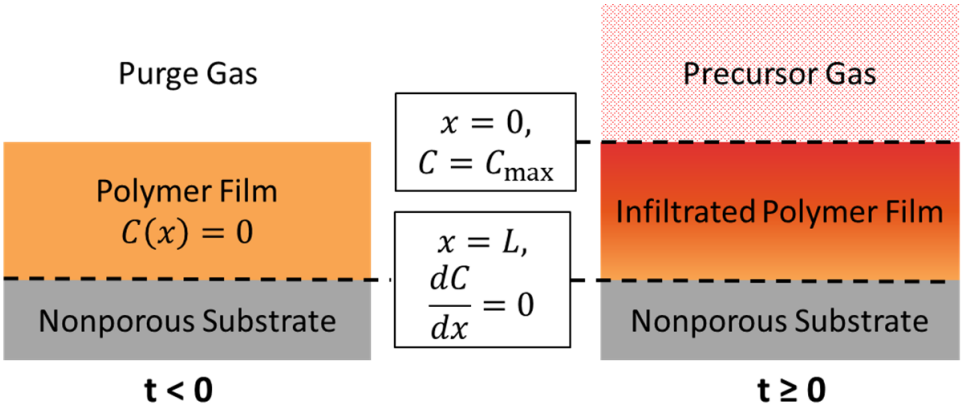

Figure 8: *Depiction of initial and boundary conditions for VPI in a thin film (unidirectional linear) geometry. At $t < 0$ (left), the polymer interior is fully devoid of precursor. At $t \geq 0$ (right), precursors infiltrate the polymer. For polymer films on non-porous substrates, no infiltration occurs from the substrate side. The concentration of precursor gas is assumed to be constant at all times $t \geq 0$.*

Solving Fick's 2nd Law under these constraints yields:

$$C(x,t) = C_{max}\left(1 - \sum_{n=0}^{\infty} \frac{2}{\lambda_n} \sin\left(\frac{\lambda_n x}{L}\right) e^{-\frac{D\lambda_n^2 t}{L^2}}\right) \qquad \textbf{Equation 9}$$

where

$$\lambda_n = \frac{(2n+1)\pi}{2}, n = 0, 1, 2, \ldots \qquad \textbf{Equation 10}$$

and L is the film thickness. Integrating this equation over the entire film thickness yields the total mass uptake as a function of time (M_t). This equation can then be normalized to the total mass uptake at infinite time (M_∞):

$$\frac{M_t}{M_\infty} = 1 - \sum_{n=0}^{\infty} \frac{2}{\lambda_n^2} e^{-\frac{D\lambda_n^2 t}{L^2}}. \qquad \textbf{Equation 11}$$

To gain insight about the VPI process, the solution variables for these equations can be normalized, where distance, time, and concentration are rescaled according to the following factors:

$$X = \frac{x}{L} \qquad \textbf{Equation 12a}$$

$$\tau = \frac{Dt}{L^2} \qquad \textbf{Equation 12b}$$

$$\phi = \frac{C}{C_{max}}. \qquad \textbf{Equation 12c}$$

Figure 9 depicts the normalized concentration profiles calculated from this linear solution. The mass fraction as a function of time is plotted in blue, while the concentration profile as a function of depth at different normalized times are shown in the inset.

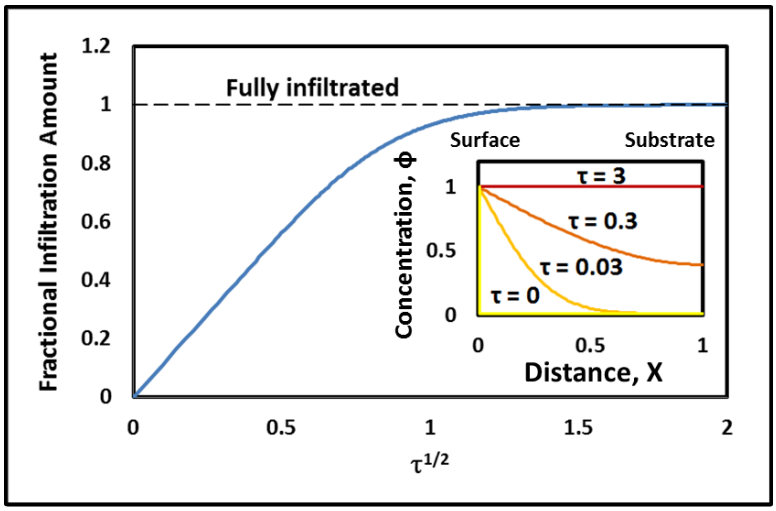

Figure 9: *Calculated fraction of total infiltration as a function of $\tau^{1/2}$ for thin film (unidirectional linear) geometry. Inset: normalized concentrations of precursors as a function of position (distance) for four different normalized times.*

To apply this solution to a real system, X and τ, which are pre-scaled to range from 0 to 1, can be scaled back to x and t if film thickness and diffusivity are known. Both **Equations 9** and **11** can be fit to experimental data to extract diffusivity. **Equation 9** is appropriate when penetrant concentration is measured as a function of diffusion depth (e.g., with secondary ion mass spectrometry) while **Equation 11** is appropriate when total penetrant concentration is measured as a function of infiltration time (e.g., with film swelling or

gravimetry). When **Equation 11** is plotted as a function of the square root of time, the initial linear slope approximates diffusivity through the following relationship:

$$\frac{\frac{M_t}{M_\infty}}{\sqrt{t}} = \frac{2}{L}\left(\frac{D}{\pi}\right)^{\frac{1}{2}}. \qquad \textbf{Equation 13}$$

Being a thermally activated process, diffusivity can be fit to an Arrhenius relationship:

$$D = D_o \exp\left(-\frac{\Delta H_D}{kT}\right) \qquad \textbf{Equation 14}$$

where ΔH_D is the activation energy for diffusion and D_o depends on the vibrational frequency of attempts for a penetrant to make a single diffusional hop. Therefore, temperature dependent measurements of diffusivity can be used to extract the activation energy for diffusion (ΔH_D).

1.3.4. Entrapment of Penetrant Molecules in Polymers

Once the gas molecule enters the polymer, the penetrant must become permanently entrapped within the matrix in order to complete the VPI process. The most direct method for precursor entrapment is the chemical reaction of penetrant molecules with polymer functional groups. For example, *in situ* FTIR studies of TMA VPI of PMMA have revealed reactions between the penetrants and the polymer's carbonyl groups.[18, 52-53] However, other mechanisms, such as reaction with a secondary precursor (co-reactant) or physical entrapment, are also believed to be possible.

Reactivity between the VPI precursor-polymer couple is critical to understanding entrapment. The "ideal" case for VPI is when the precursor-polymer couple is moderately reactive with itself (e.g., many metalorganic precursors have been found to be modestly reactive with polymers containing carbonyl or amide functional groups). For the case of moderate reactivity, precursor penetrants can diffuse substantially into the polymer prior to becoming entrapped via chemical reaction. This situation is depicted in **Figure 10a**. Upon chemical reaction, the inorganic moiety is permanently bound to the polymer and cannot be removed. This type of VPI process may be site-limited and self-terminating

akin to ALD. However, unlike ALD, these self-terminating reactions are not restricted to surface sites. Bulk diffusion to these sites is necessary to reach site saturation. Other considerations, including cross-linking and steric hindrance may also affect saturation concentration.

Precursor-polymer couples that are unreactive towards one another can be difficult to entrap (e.g., in the case of most metalorganic precursors with purely hydrocarbon polymers like polyethylene and polypropylene). While precursor penetrants may be able to sorb and diffuse throughout the polymer, physical binding mechanisms may be insufficient to retain these molecules upon removal of their vapor pressure and followed with a prolonged purge (**Figure 10b**). One approach to compel VPI in unreactive polymers is to introduce a second precursor (co-reactant) to react with the initial penetrant and drive entrapment (**Figure 10c**). For this case, site-saturation is no longer meaningful. No fixed number of reaction sites exists within the unreactive polymer, and deposition becomes completely reliant on the kinetics of precursor and co-reactant diffusion and reaction.

For highly reactive precursor-polymer couples (e.g., TMA and hydroxyl groups), reactions can occur at the surface and create a barrier layer that prevents subsequent precursor diffusion. Because this type of immediate reaction precludes penetrant diffusion within the bulk polymer, it cannot be considered a form of VPI.

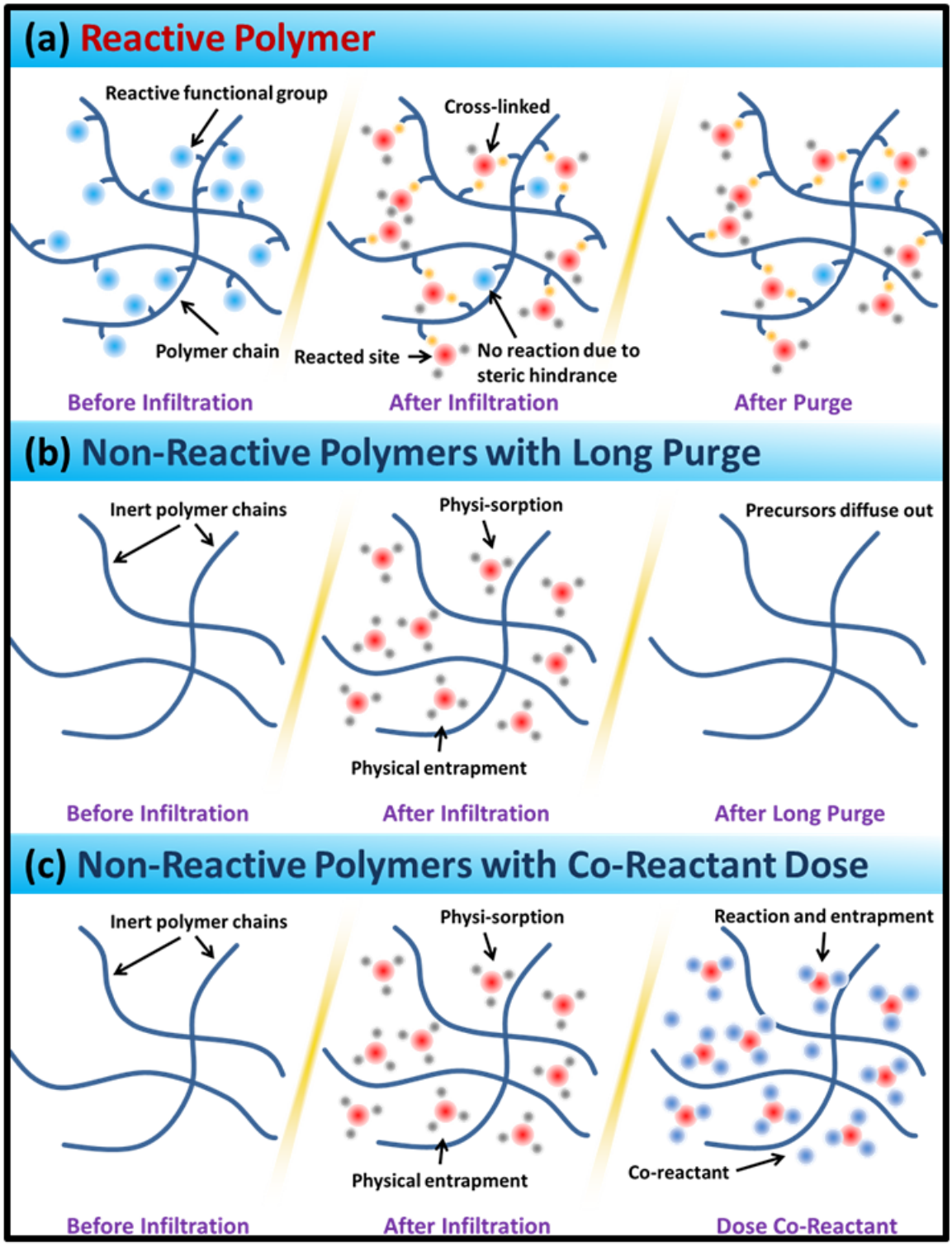

Figure 10: *Schematic of precursor entrapment. (a) VPI with definitive site saturation. Blue dots represent reactive functional groups on the polymer chain. After infiltration, metalorganic precursors (red and gray dot clusters) bind to all available functional group reaction sites. Yellow dots indicate new bond formation between precursor and*

polymer. Full site saturation may be limited by cross-linking and steric hindrances. After purge, reacted precursors remain in place. (b) VPI with indeterminate site saturation. Inert polymer has no reactive sites. Precursors are trapped by physisorption or steric hindrances. No new bonds form between precursor and polymer. After long purge, precursors completely diffuse out of the polymer. (c) Similar case to (b) except with co-reactant dosing after precursor infiltration. Co-reactants lock in some precursors through entrapments like increased steric hindrances.

1.3.5. VPI Kinetics with Chemical Reactions

VPI precursors may react with their host polymer. For example, *in situ* FTIR studies of TMA VPI of PMMA have revealed reactions between the penetrants and the polymer's carbonyl groups.[18, 52-53] These reactions can act as a "sink" for the diffusing penetrants, reducing the unreacted precursor's effective concentration in the polymer. Depending on the reaction rate, this "sink" for penetrants may resemble an increase in diffusional activation energy because penetrants become "trapped" at reaction sites rather than diffusing deeper into the material. At these higher reaction rates, we can assume a local equilibrium in the material that follows a "reaction sink": ($\partial C^*/\partial t$), where C^* is the concentration of precursors that have reacted with the polymer. Assuming a first order immobilization rate the reaction constant (K) can be written as:

$$K = \frac{C^*}{C} \qquad \textbf{Equation 15}$$

This reaction rate can then be added to Fick's 2nd Law:

$$\frac{\partial C}{\partial t} = D\frac{\partial^2 C}{\partial x^2} - \frac{\partial C^*}{\partial t} \qquad \textbf{Equation 16}$$

which by combining with **Equation 15** can be algebraically simplified to:

$$\frac{\partial C}{\partial t} = \frac{D}{K+1}\frac{\partial^2 C}{\partial x^2}, \qquad \textbf{Equation 17}$$

This solution implies that with reactions, an "effective diffusion coefficient" (D^*) can be defined as:

$$D^* = \frac{D}{K+1}. \qquad \textbf{Equation 18}$$

Thus, the solution to Fick's 2nd Law with a reaction sink will have the same functional form as pure diffusion, except the diffusion coefficient will be convolved with the reaction equilibrium constant. As a consequence, diffusion will appear to be slower because the diffusion flux is effectively reduced by reactive consumption of penetrant molecules.

Figure 11 illustrates how increasing the reaction constant (K) decreases the VPI infiltration rate for both linear and radial cases. For non-linear reactions such that $C^* = KC^n$, where $n \neq 1$, the resulting nonlinear equation must be solved numerically,[51] but a similar trend should be observed.

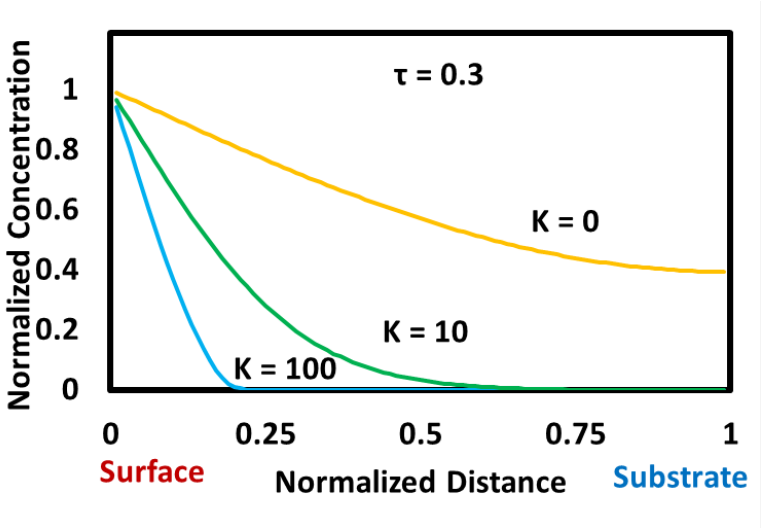

Figure 11: *Calculations of normalized precursor concentration as a function of position in a thin film (unidirectional linear) geometry for varying reaction constant values, K = 0, 10, and 100. K = 0 equates to the purely diffusional condition that was previously plotted in* ***Figure 9****. All concentration profiles are calculated at a normalized time of* $\tau = 0.3$.

Two extreme cases exist for D^*: (1) when the reaction constant is small ($K << 1$), penetrants will freely diffuse with minimal influence from reactions, and (2) when the reaction constant is large ($K >> 1$), reactions will immobilize most penetrants, thereby effectively determining the transport rate. For the former case ($K << 1$), D^* reduces to D,

suggesting that reaction kinetics are "inconsequential" to the total process kinetics. In the latter case (K >> 1), **Equation 18**, can be rewritten as:

$$D^* = \frac{D}{K} \qquad \textbf{Equation 19}$$

A Van't Hoff equation can then be used to describe the temperature dependence of the reaction equilibrium:

$$K = K_o exp\left(\frac{-\Delta H_{rxn}}{kT}\right). \qquad \textbf{Equation 20}$$

where K_o includes the temperature independent entropy change for the reaction. Substituting the temperature dependent reaction (**Equation 20**) and diffusion (**Equation 14**) equations into **Equation 19**, it is possible to write a new Arrhenius-like expression for the effective diffusion coefficient with reaction:

$$D^* = D_0^* \exp\left(-\frac{\Delta H_D - \Delta H_{rxn}}{kT}\right) \qquad \textbf{Equation 21}$$

where ΔH_{rxn} is the reaction enthalpy for the precursor-polymer reaction, D_o^* is a temperature-independent term that combines phenomena related to the entropy of reaction and the attempt frequency for diffusional hopping into a new constant. Assuming the reaction is exothermic (favorable), ΔH_{rxn} would be a negative value and additive with ΔH_D, creating a larger "effective" barrier to diffusion, effectively slowing the diffusion rate.

If the precursor-polymer reaction rate is of similar time-scale to precursor diffusion, the kinetic process can no longer be described by a simple analytical model. For example, reaction rates much slower than diffusion rates may start decreasing precursor concentration near the surface of the polymer, where the earliest precursors have already interacted with polymer functional groups for longer times. The rate of new precursors replenishing the surface region will be difficult to predict, and the infiltration behavior for such systems may need to be studied experimentally and fit to numerical solutions customized for a given set of conditions.

1.3.6. Comprehensive Equation for VPI Processing

Combining sorption, diffusion, and reaction, we present a comprehensive equation based on the solution to Fick's Second Law of diffusion (**Equation 22**) that can be used to describe any VPI system with fast reaction and sufficient Fickian diffusion behavior.

$$C(x,t) = S_o \exp(-\frac{H_s}{kT}) \left[1 - \sum_{n=0}^{\infty} \left(\frac{2}{\lambda_n} \right) \sin\left(\frac{\lambda_n x}{L} \right) \exp\left(- \frac{D_o^* \exp\left(- \frac{\Delta H_D - \Delta H_{rxn}}{kT} \right) \lambda_n^2 t}{L^2} \right) \right]$$

$$\lambda_n = \frac{(2n+1)\pi}{2},\ n = 0,\ 1,\ 2,\ \ldots \qquad \textbf{Equation 22}$$

This equation takes into account sorption enthalpy, activation energy of diffusion, and reaction enthalpy. By knowing the values to these constants and the dimensions of the polymer system, one can use this equation to predict the concentration profiles with different infiltration times.

1.4. Methods for Characterizing VPI Materials

Characterizing the chemical and microstructural features of vapor phase infiltrated polymers is crucial to quantifying VPI processing kinetics and understanding the structure-property relations of the newly formed hybrid materials. Perhaps the most important feature to characterize is the "depth" of inorganic infiltration. Other structural features of interest include the chemical bonding between organic and inorganic components and the size of the inorganic phases. Characterizing organic-inorganic hybrid materials presents several challenges also seen in purely organic systems, including how to manage radiation damage and avoid sample charging. Here, we review the opportunities and limitations for several key characterization tools used for analyzing the structure and chemistry of vapor phase infiltrated polymers. Methods reviewed include cross-sectional electron microscopy, quartz crystal microbalance (QCM) gravimetry, Fourier transform infrared (FTIR) spectroscopy, secondary ion mass spectrometry (SIMS), spectroscopic ellipsometry, and thermogravimetric analysis (TGA).

1.4.1. Cross-Sectional Electron Microscopy

Cross-sectional electron microscopy is ideally suited to probe the infiltration depth of a VPI processed polymer material. Electron microscopy's inherent atomic number contrast enables direct visualization of inorganic constituents infiltrated within an organic matrix. However, difficulty with preparing cross-sectional samples and managing electron beam damage pose significant challenges to implementing this technique. **Figure 12** provides several examples of successful cross-sectional microscopy studies conducted on VPI modified polymer systems.[37, 46, 54]

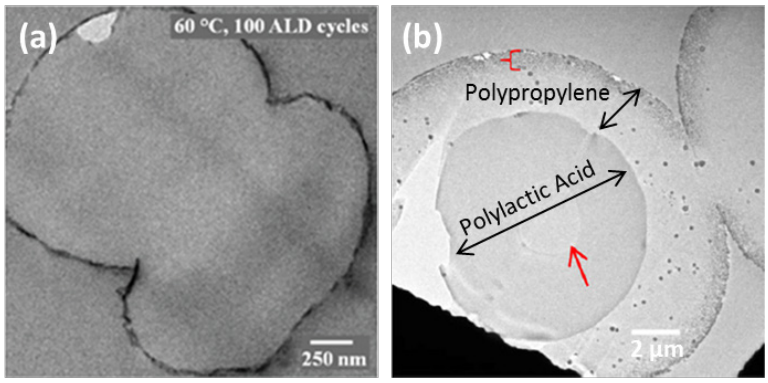

Figure 12: *Cross-sectional electron microscopy images of (a) PP fibers with 100 short TMA/H_2O infiltration cycles and (b) PLA/PP core/sheath fibers with 100 long TMA/H_2O infiltration cycles. While only a thin outer shell is evident in (a), TMA is observed to diffuse through the PP shell in (b) and react with the interior PLA section.*[37, 54]

Preparation of high-quality cross sectional samples is a critical obstacle to microscopic imaging. One of the most successful approaches has been the cross-sectional microtoming of VPI modified fibrous materials.[37, 54] To reduce artifacts, fibers are typically embedded inside a block of epoxy resin prior to microtoming with a diamond blade. Thin slices of ~100 nm thickness are cut, collected on conductive grids, and imaged in a transmission electron microscope (TEM). While the organic material is

relatively soft and easily sliced with a microtome, inorganic surface layers are susceptible to fracture and delamination. Water soluble fibers, like polyvinyl alcohol (PVA), are also incompatible with common aqueous microtoming conditions.[33] Preparation of cross-sectional samples from VPI polymer films on rigid substrates (e.g., silicon) is more difficult. Obuchovsky et al.[55] have had success with cryo-fracturing while Sun et al.[46] have prepared samples using focused ion beam (FIB) machining. Once the cross-section is prepared, sample charging in SEM and sample damage in TEM can also pose challenges. Attempts at compositional analysis with electron spectroscopy techniques like EDS and EELS have also been fairly limited and qualitative at best.[15]

Despite these limitations, electron microscopy has proven useful in elucidating the complex relationship between VPI process temperature and inorganic infiltration depth. Polymers that are unreactive toward gaseous precursors show increased diffusion depths with increased process temperature. Electron microscopy has also revealed that polymers with more reactive functional groups often show reduced infiltration depths at higher temperatures, presumably due to faster reaction kinetics (e.g. **Figure 6a-c**). Electron microscopy can also reveal whether the distribution of inorganic material is homogeneous or heterogeneous (e.g. **Figure 12**).

1.4.2. Quartz Crystal Microbalance (QCM) Gravimetry

Gravimetry, the measurement of mass change, is commonly used *in situ* for monitoring VPI processing. In QCM gravimetry, a thin piezoelectric AT-cut quartz crystal is oscillated at its resonance frequency with an applied AC electric field. Deposition of material onto the quartz crystal adds mass which alters the crystal's resonance frequency according to the Sauerbrey equation:

$$\Delta f = -\frac{2f_o^2 \Delta m}{A\sqrt{\mu\rho}}. \qquad \textbf{Equation 23}$$

Here, Δf is the change in frequency, f_o is the fundamental resonance frequency for the unloaded crystal, Δm is the mass change, A is the surface area, μ is the shear modulus of

the quartz crystal, and ρ is the density of the quartz crystal. This shift in resonance frequency can easily detect mass changes as small as 0.4 ng/cm^2, enabling monolayer sensitivity.[56]

Mass changes during polymer infiltration are sufficiently small to maintain the linear behavior predicted by the Sauerbrey equation.[56-57] For a typical AT-cut quartz oscillator of mass 0.5 g/cm^2, linearity is maintained up to mass changes of 20x to 50x (10 to 25 μg/cm^2). Mass uptake during VPI of a polymer film typically ranges between 100 to 3000 ng/cm^2 during the first cycle and saturates below 10 μg/cm^2 after many cycles or under longer holds.[18, 47, 56-58]

When performing *in situ* QCM gravimetry of a VPI process, the quartz crystal is first coated (usually by spin-casting) with the polymer. The QCM is then equilibrated in the vacuum environment and subsequently exposed to the gaseous precursor. Temporal variations in the resonance frequency can then be equated to mass uptake or loss. QCM has been frequently used to study VPI since the mass changes give insight into how much infiltration is occurring at different stages of an experiment. QCM is a fairly simple *in situ* monitoring tool for such processes and the time-dependent gravimetric data can be used to quantitatively assess the process kinetics.

Figure 13 shows example data from a QCM gravimetric study for the exposure of TMA vapors to polyamide-6 (PA-6), polyethylene terephthalate (PET), poly(methyl methacrylate) (PMMA), and polyacrylic acid (PAA) at 60 ^{o}C.[47] In all cases, the polymer was exposed to a 0.2 s dose of TMA followed by a 2 min purge. This process was repeated 10 times without a water dose. Important information is gained from both the mass change after the first dose and after subsequent doses. For the case of PA-6, high quantities of TMA are absorbed after just a single dose (2625 ng/cm^2) with a significant fraction (~80%) retained after the 2 min purge. This behavior suggests significant diffusion of TMA into PA-6 concurrent with permanent binding of the TMA to the PA-6 polymer chemistry. Negligible increases in TMA loading after this initial pulse suggest a saturation behavior in this system. In contrast, PET and PMMA exhibit less sizable initial sorption of TMA, but can continue to sorb TMA after the initial dose. This behavior suggests that diffusion of TMA is slower in these polymers at this temperature. However,

this diffusion is not significantly impeded with repeated cycling. After 10 doses, PET has sorbed 750 ng/cm^2 of TMA and PMMA has sorbed 250 ng/cm^2 of TMA. Finally, PAA, which has a hydroxylated surface chemistry, exhibits behavior consistent with surface-confined reactions without any significant infiltration into the polymer. After 10 pulses of just TMA, the mass gain is only about 90 ng/cm^2, which is near the expected value for a surface-limited ALD process (~35 ng/cm^2).[56]

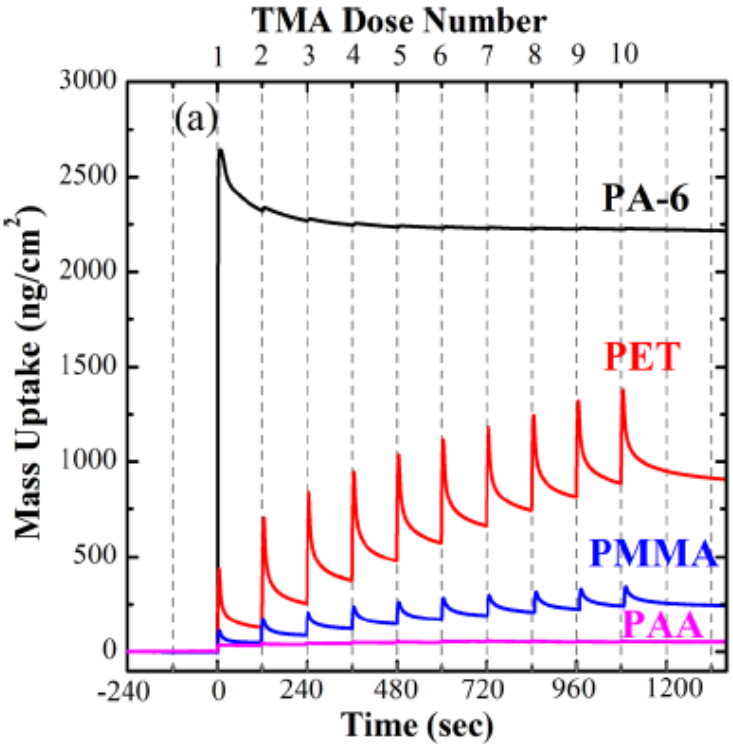

***Figure 13**: In situ QCM gravimetric measurements of mass uptake as a function of time and cycling for TMA VPI of various polymer films at 60 °C.*[47]

1.4.3. Fourier Transform Infrared Spectroscopy (FTIR)

FTIR is used in VPI processing to observe chemical changes. FTIR can detect both the introduction of inorganic species and changes to the organic polymer chemistry. For example, *ex situ* FTIR studies have revealed changes to the chemistry and structure of the

extremely inert polymer polytetrafluoroethylene (PTFE) when VPI treated with diethyl zinc (DEZ). As illustrated in **Figure 14a**, DEZ VPI leads to structural changes in the PTFE chain ends and a reduction in the amorphous fraction of the polymer.[59-60]

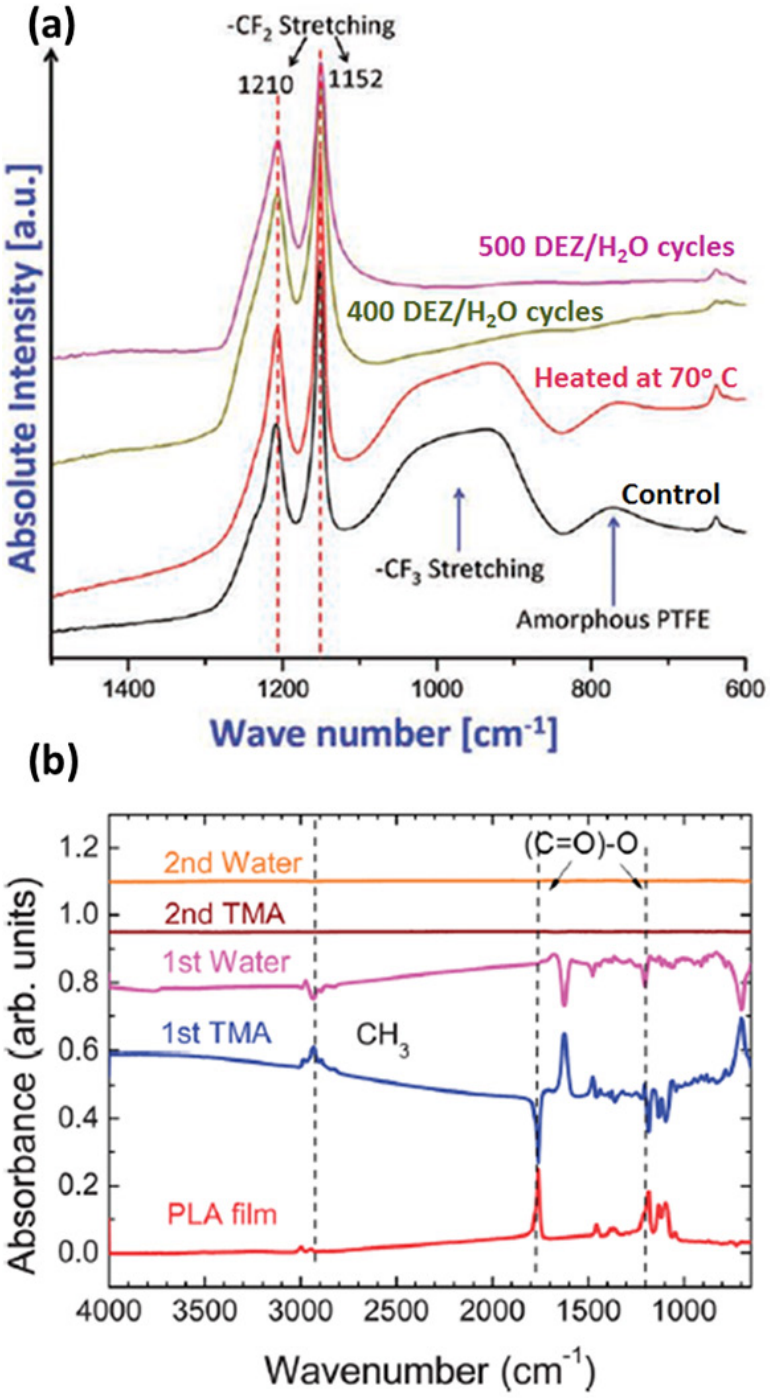

Figure 14: *FTIR analyses of VPI modified polymers. (a) Ex situ FTIR measurements of DEZ VPI of PTFE at varying cycle numbers. (b) In situ FTIR measurements of TMA VPI of PLA films after each processing step.*[59, 61]

In situ FTIR has been conducted to study real-time reactions of VPI processing.[18, 33, 37, 52, 61-62] Functional groups like hydroxyls (-OH), carbonyls (C=O) and amines (-NH2) have been identified as reactive sites for various metal organic precursors used in VPI. For example, Gong *et al.* studied TMA VPI of polylactic acid (PLA).[37, 61] Differential FTIR spectra from two TMA-H_2O VPI cycles are shown in **Figure 14b**. The untreated PLA film has C=O ester bonds with absorbance peaks at 1720 cm^{-1} and 1260 cm^{-1}. After a single TMA dose, these C=O absorptions disappear and a new absorption peak emerges at 2960 cm^{-1}. This peak is assigned to the asymmetric stretching of CH_3, presumably from the TMA moiety.[61] After exposing the system to water vapor, the Al-CH_3 rapidly disappears, suggesting that this is only an intermediate chemical state. Subsequent TMA and water doses do not produce any further changes to the polymer chemistry, suggesting that VPI is completed in a single dosing cycle. Because surface reactions would not produce such intense absorption intensities, this study also provides evidence for the subsurface nature of these chemical reactions. Using *in situ* FTIR to identify VPI intermediate states is immensely powerful. These transient chemical states could be used to design new VPI reaction pathways and create entirely different hybrid material chemistries.

1.4.4. Secondary Ion Mass Spectrometry (SIMS)

SIMS is commonly used for compositional depth profiling in inorganic thin films. However, SIMS analysis of polymeric films has only recently become reliable. Conventional ion beams composed of single atoms (e.g., Cs^+ or Ar^+) often create weak inelastic scattering within organic materials, leading to poor secondary ion yield. These ion beams can also create large damage field that disrupt sub-surface composition and

obfuscate the interpretation of collected results from organic samples. Cluster ion sources (e.g., C_{60}^+ or SF_5^+) significantly improve secondary ion yield (1000x) for polymers and reduce subsurface damage.[63] The relative importance of these effects in organic-inorganic hybrid materials is not known.

As a result, few studies of SIMS depth profiling of VPI polymers have been reported. In 2014, Padbury and Jur used SIMS with a Cs^+ source to study the infiltration of TMA in PBT and PA-6 films.[40] This SIMS data, reproduced in **Figure 15**, reveals that after infiltrating with 10 separate TMA dose/hold cycles at 60 °C, Al penetrates the PA-6 film to a depth of 110 nm and the PBT film to a depth of 820 nm. For PBT, this depth was the entire thickness of the film. For PA6, a clear decline in Al concentration was observed prior to sampling the silicon substrate. These SIMS results corroborated QCM data indicating significantly greater mass uptake in PBT than PA6 and suggest that SIMS measurements, even with single atom ion sources, may be a useful technique for future investigations of inorganic infiltration depth in VPI materials.

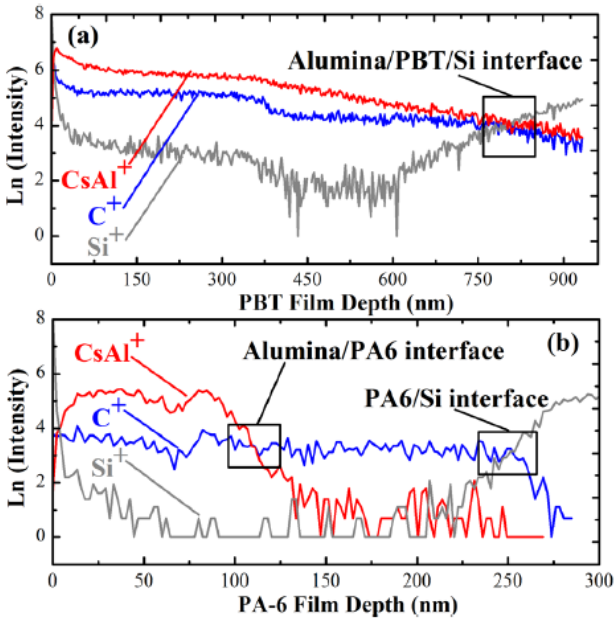

Figure 15: *TOF-SIMS concentration profile of TMA VPI of (a) PBT and (b) PA-6 thin films.*[40]

1.4.5. Spectroscopic Ellipsometry

Spectroscopic ellipsometry is an optical technique commonly used to characterize the thickness and refractive index of thin films.[64] Spectroscopic ellipsometry can be sensitive to sub-nanometer changes in film thickness and < 0.01 changes in refractive index. These changes in refractive index can potentially be used to track changes in film composition, including compositional gradients. However, these sorts of analyses are an indirect measure of film composition and are subject to interpretation of the physical models used to describe the system.

We have used ellipsometry to monitor polymer film thickness before and after VPI modification. **Figure 16** shows representative data for such an experiment. Here, PMMA films are infiltrated with TMA. These films swell significantly (≈20%) after infiltration at 60^{o} C (under T_g of PMMA) for several hours. This change in film thickness and composition is evident both visually and in the raw spectroscopic ellipsometry data (i.e., both the ellipsometric amplitude (psi) and polarization (delta) functions show shifts after infiltration). This data parallels optical measurements taken of film swelling in vapor phase annealing experiments and demonstrate spectroscopic ellipsometry's potential for investigating the structural changes that occur in VPI modified polymer films.[65]

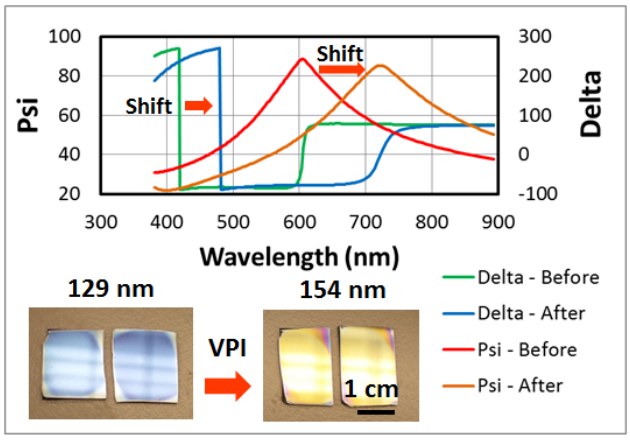

***Figure 16**: Spectroscopic ellipsometry data (psi and delta functions) collected for PMMA films before and after TMA VPI. Inset images show the color change that occurs in these films before and after VPI.*

1.4.6. Thermogravimetric Analysis (TGA)

In thermogravimetric analysis (TGA), the mass of a material is tracked as a function of temperature. If TGA of VPI-treated material is conducted in an oxidizing atmosphere (e.g., air) it is possible to combust the organic portion, leaving only the inorganic fraction remaining. By carefully considering the mass of the remaining oxidized inorganic, it may be possible to determine the mass fraction of inorganic material vapor phase infiltrated into a polymeric material. Gong et al. conducted TGA on TMA/water infiltrated PBT fibers and measured a 75% mass loss, with 25% mass still remaining after heating to 900 ^{o}C, whereas pure PBT fibers exhibited 100% mass loss past 525 ^{o}C.[17] Gong and Parsons also showed that nonwoven PBT fibers infiltrated with one TMA/water cycle (60 min for each precursor) could be annealed at 450 ^{o}C overnight to yield solid inorganic fibers, indicating full infiltration.[61] Dandley et al. conducted a similar evaluation where TMA VPI (or SVI) PMMA films were pyrolyzed in air (i.e, the organic fraction was "burned off"). Instead of measuring mass, these researchers used ellipsometry to measure film thickness after pyrolysis. As shown in **Figure 17**, this film thickness increased with the number of TMA doses until a saturation point was reached.[66]

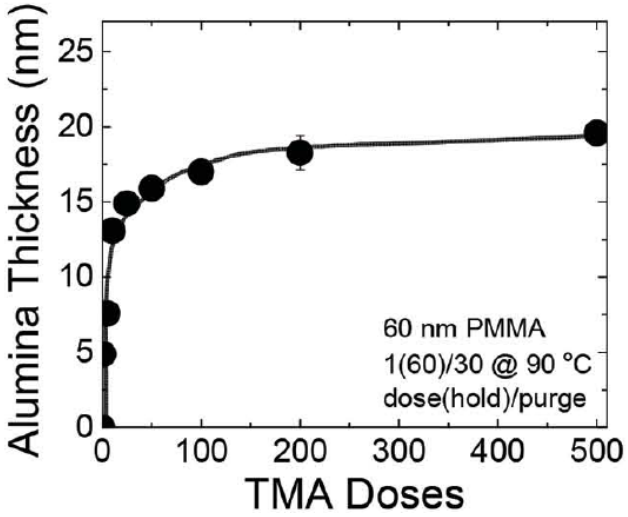

Figure 17: *Thickness of alumina layer as a function of TMA doses for VPI treated (90 °C) 60 nm PMMA films on silicon after pyrolysis at 500 °C in air. Cycles consisted of 1 s TMA doses followed by 60 s holds and 30 s N_2 purges.*[66]

1.5. Applications of VPI

Vapor phase infiltration of polymers creates new organic-inorganic hybrid materials with markedly different properties from the original polymer. Because this vapor phase process can transform polymers of any form factor (e.g., films, fibers, fabrics, or powders) into a hybrid material, VPI has immense potential for adding functionality to numerous products and technologies. Gregorczyk and Knez recently reviewed some of the applications demonstrated for these hybrid materials based upon polymer type (natural and synthetic).[67] In the following sections we focus on potential application areas for VPI processing and the current levels of performance reported.

1.5.1. Mechanical Strengthening

For certain polymer-precursor combinations, VPI can be used as a cross-linking agent. This chemical cross-linking often improves the elastic modulus and/or mechanical toughness of a material. In 2009, Lee *et al.* first demonstrated the use of VPI for mechanical strengthening by infiltrating spider dragline silks with trimethylaluminum, diethyl zinc, and titanium isopropoxide.[9] These infiltrated polymer fibers showed ~4x increase in elastic modulus and ~3x increase in ultimate tensile strength.[9, 36] These authors identified a unique chemical reaction pathway. Water vapor infiltration disrupted hydrogen bonding in amorphous regions of the spider silk. These activated regions then became receptive to covalent bond formation with metal ions upon exposure to a metalorganic precursor. These organic-metal-organic cross-links strengthened the spider silk. Exposure to metalorganic precursors alone provided no benefit in mechanical strengthening. However, when done properly, only a few cycle numbers were necessary to achieve enhanced toughness, precluding the formation of any outer shell oxide coating.

This mechanical strengthening was clearly the result of modification to the bulk polymer chemistry not a surface effect.[36]

VPI can also enhance the elastic modulus and ultimate tensile strength of cellulosic fibers.[10] In cellulose, metalorganic precursors can form cross-links between exposed hydroxyl groups. As reproduced in **Figure 18a**, DEZ is found to be more effective than TMA in increasing the ultimate tensile strength of cellulosic fibers. Optimal DEZ treatments (4 dose / hold cycles) increase the elastic modulus and ultimate tensile strength by about 2x while optimal TMA treatments (5 dose / hold cycles) increase these properties by only about 1.1x. Additional VPI cycles are found to degrade the mechanical properties. Using Raman spectroscopy, Gregorczyk *et al.* determined that both chemistries form cross-links between cellulosic polymer chains but also attack the backbone of the cellulosic molecules. Degradation of this backbone structure is the source of reduced mechanical strength, and TMA, which is a stronger Lewis acid than DEZ, degrades the backbone more rapidly than DEZ.[10]

Infiltration can also affect the mechanical properties of synthetic polymers. Sun *et al.* showed that free-standing PA6 films infiltrated with TMA (alumina) can block crack propagation more effectively than films coated on the surface with alumina.[46] As shown in **Figure 18b**, this slower crack growth rate increases the toughness of the infiltrated PA6 film. Sun *et al.* found that lower VPI temperatures resulted in greater infiltration of PA6 films. This greater infiltration generally reduced the density of cracks with applied strain.

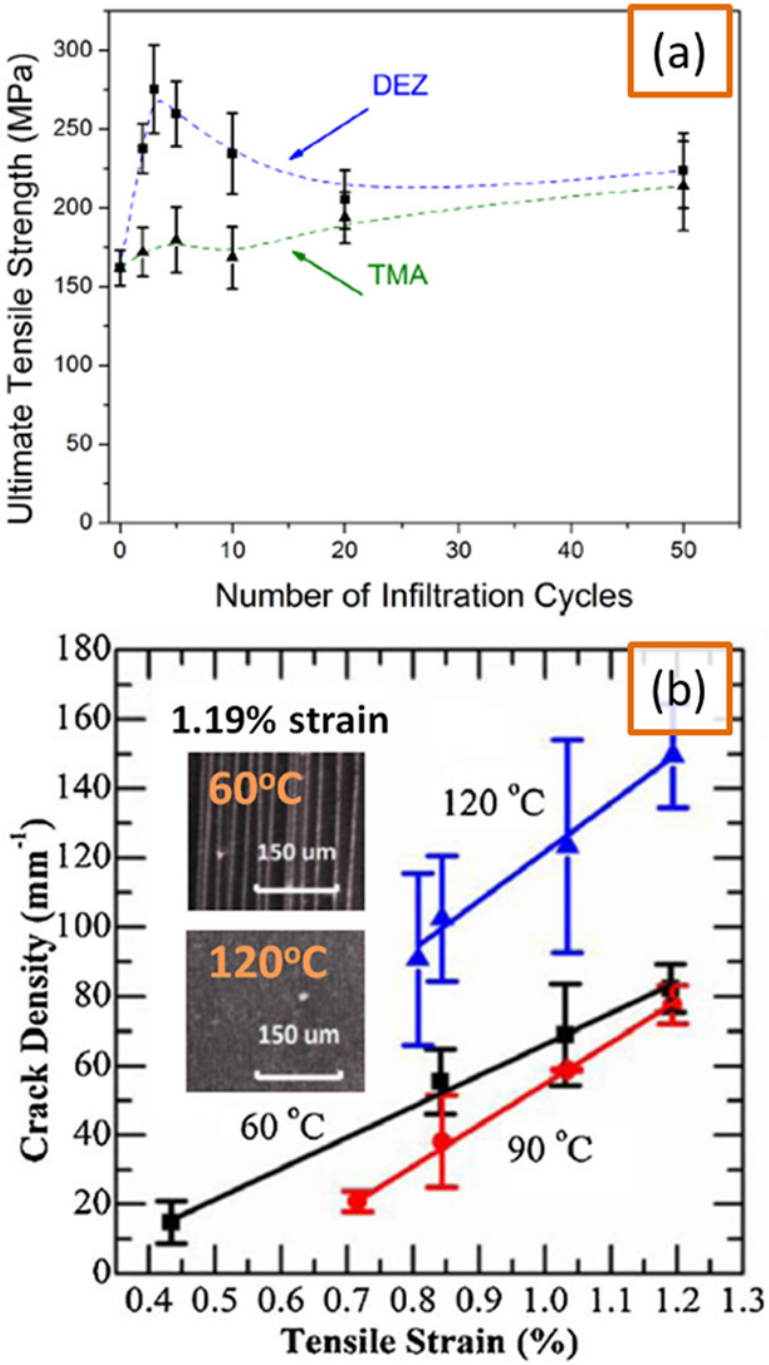

Figure 18: *(a) Ultimate tensile strength of cellulose fibers as a function of TMA and DEZ VPI cycle number.*[10] *(b) Crack density as a function of tensile strain for TMA VPI modified PA-6 films processed at varying temperatures. Inset shows optical images of the crack density for 60 °C and 120 °C processed films at 1.19% strain.*[46]

1.5.2. New Approaches to Micro- and Nano-Patterning

Polymer resist layers used for electron beam lithography must be sufficiently thin to minimize electron scattering and maintain nanoscale pattern resolution. Unfortunately, these thin resist layers are quickly eroded under the plasma etching conditions necessary to achieve high-aspect ratio features in inorganic substrates. To overcome poor durability of polymer resists, intermediate hard mask layers are added. However, these hard mask layers require additional processing steps and can result in a loss of pattern accuracy and registry. Recently, researchers at Argonne National Laboratory have demonstrated the use of VPI resist patterns for improved plasma etch resistance.[11, 14-15] **Figure 19** compares the processing steps necessary for electron beam patterning with VPI versus with a hard mask.

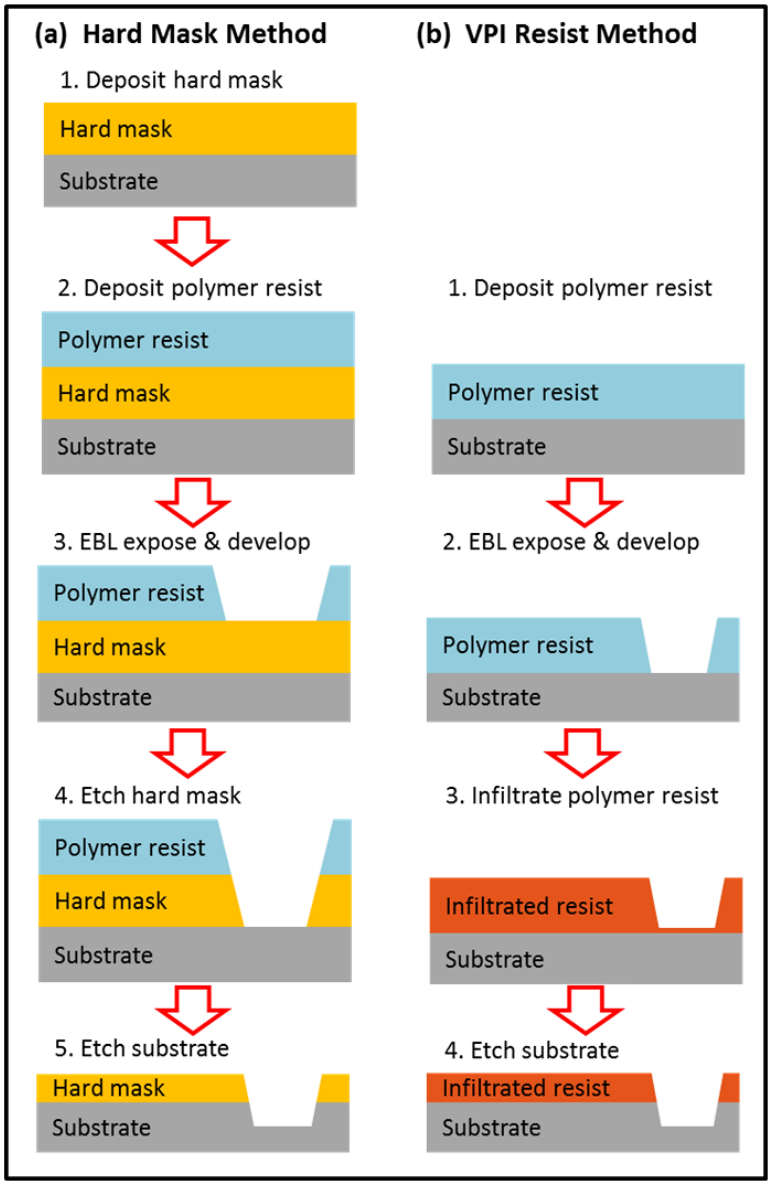

Figure 19: *Flow charts for electron beam lithography patterning using (a) a hard mask and (b) VPI of the polymer resist.*

VPI modified e-beam resists are substantially more tolerant towards HBr plasma etching than untreated resists. For an HBr plasma etch rate of silicon of ~100 nm/min, unmodified PMMA and ZEP520A polymer resist films etch at rates of ~300 nm/min and ~100 nm/min respectively.[15] These etch rates reduce by 40x (~8 nm/min) and 5x (~20 nm/min) for VPI-modified PMMA and ZEP520A films respectively.[15] Using 50 nm thick VPI PMMA, Tseng *et al.* produced high aspect ratio trenches in silicon—50 nm in width

and 300 nm in depth—without an intermediate hard mask.[11] Interestingly, these researchers also reported that looking top-down, sidewalls of the resist pattern were physically higher than the interior regions. This effect is a result of higher precursor diffusion into the sidewalls. Line-edge roughness of the sidewalls was also retained through the VPI process, further preserving feature resolution.[15]

In related work, the Argonne group has also demonstrated the use of VPI to form nano-scale etch resists out of self-organized block co-polymers (BCPs). BCPs have long been investigated as a means for nanolithography.[68-69] Mask patterning is accomplished by allowing the BCPs to self-assemble into precise nanopatterned arrangements and then selectively etching one of the polymer blocks. Similar to the e-beam resists discussed above, these BCP patterns are often thin and susceptible to rapid erosion from etchants including plasmas. Organic-inorganic BCPs containing silicone blocks have been explored, but these require complicated chemistries.[70] Recently, Peng et al. demonstrated that the PMMA block of the common PMMA-b-PS BCP can be selectively converted into an organic-inorganic hybrid layer via VPI. Precursors like TMA and $TiCl_4$ bind to carbonyl groups in the PMMA block while no reactions occur in the polystyrene (PS) blocks. This selective reaction transforms the PMMA into etch-resistant domains similar to those discussed in the prior section.[14, 71] **Figure 20** shows an example of 3-dimensional nanostructures created with this VPI-modified PMMA-b-PS process. Silicon trenches with aspect ratios of up to 10:1 have been reported.[15]

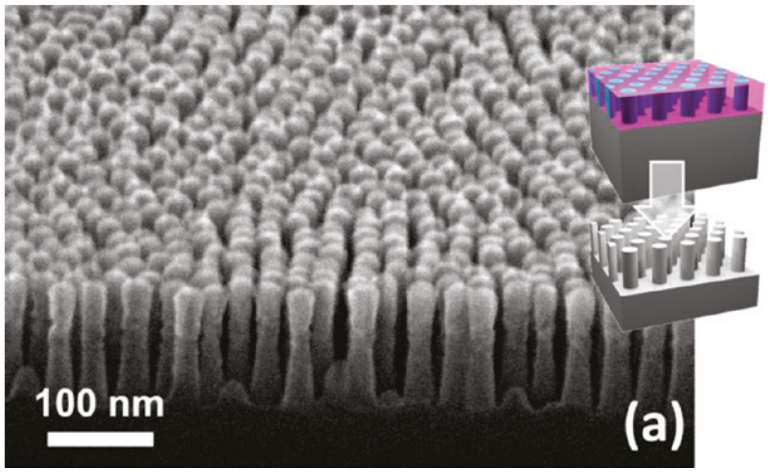

Figure 20: *SEM image of the VPI modified PMMA domains of a self-assembled BCP structure after PS removal.*[14]

Researchers have also converted self-assembled BCPs directly into inorganic nano-patterns. PMMA-b-PS assembled into the hexagonal cylinder phase have been used to create pure aluminum oxide and titanium oxide nano-rods.[39] In this process, VPI precursors become selectively entrapped within the rod-like PMMA phase. Upon organic pyrolysis, the inorganic precursors react to form a nanoporous oxide material that retains the PMMA's original rod-like shape. The size of these nano-rods can further be adjusted by the number of VPI cycles. Rod diameter was also influenced by precursor chemistry, with $TiCl_4$ producing smaller diameter rods than TMA, presumably due to less reactivity towards the PMMA's carbonyl groups.[71] These purely oxide nanomaterials have potential applications in water photoeletrolysis, gas sensing, and heterojunction solar cells.[72]

Dandley *et al.* has used a similar VPI + organic pyrolysis approach to produce oxide nanostructures from e-beam lithography patterned PMMA material [66]. Electron microscopy images of reproduced in **Figure 21** illustrate how lithographic features in the PMMA patterns (**Figure 21a**) can be transferred with high fidelity to the final aluminum oxide material (**Figure 21b**).

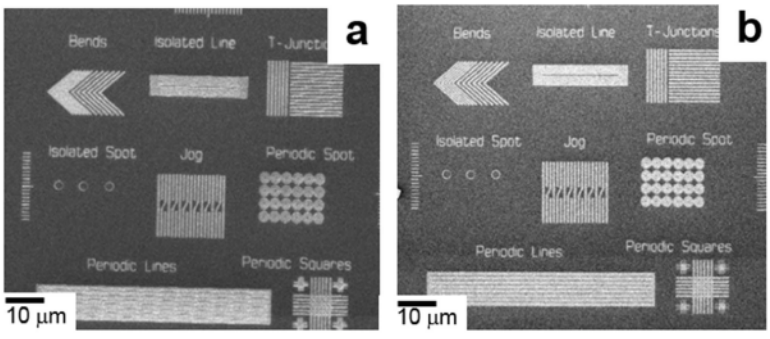

Figure 21: *SEM images of (a) PMMA e-beam lithography patterns and (b) these same patterns after TMA VPI and organic pyrolysis are used to transform these patterns into purely* Al_2O_3 *structures.*[66]

1.5.3. Vapor Diffusion Barriers

Organic-inorganic hybrid layers are of interest for their flexible, vapor-barrier properties.[73-75] While VPI may potentially offer a new approach for forming these barriers, few published examples currently exist. One example, comes from Gong *et al*. who demonstrated vapor barrier properties of PDMS material vapor phase infiltrated with TMA.[41] Maintaining hydrophilicity of a PDMS surface is important in microfluidics. Unfortunately, out-diffusion of organic constituents from the PDMS bulk can lead to a gradual loss of hydrophilicity. Using VPI, Gong *et al.* demonstrated that a mechanical barrier to organic component diffusion is possible. Further investigations of vapor transport properties in VPI modified polymers are warranted for applications like organic electronics packaging.

1.5.4. Hybrid Photovoltaic Cells

ZnO nanoparticles embedded in P3HT via VPI have shown promise for hybrid organic-inorganic solar cell applications.[12, 76] The VPI process allows DEZ and water to infiltrate the entire thickness of a typical 150 nm P3HT thin film and serve as nucleation sites for ZnO nanoparticle growth. Cross-sectional SEM images of this process are reproduced in **Figure 22**. Using an ALD-like cycling recipe (no holds, long purges), Obuchovsky *et al.* found that nucleation requires about 38 DEZ/H_2O cycles (**Figure 22b**). Subsequent cycles further increased the ZnO nanoparticle size. Beyond 55 cycles (**Figure 22d**), ZnO clusters begin to coalesce and form a network within the P3HT film. Concurrently, a layer of ZnO begins coalescing on the exposed P3HT surface (**Figure 22e and 22f**).

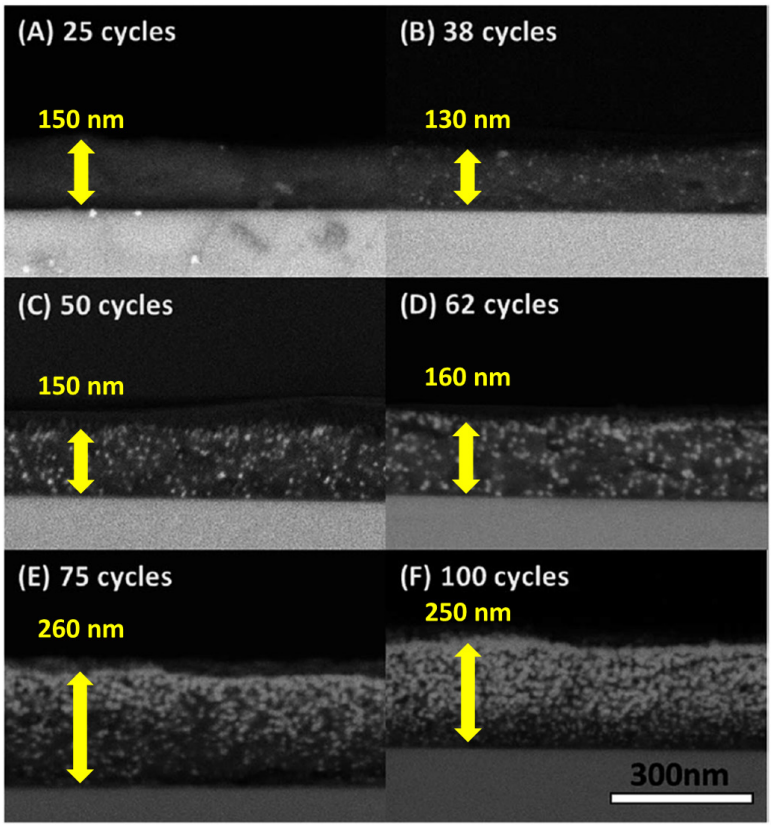

Figure 22: *Cross sectional SEM images of P3HT films infiltrated with (a) 25, (b) 38, (c) 50, (d) 62, (e) 75, and (f) 100 DEZ/H_2O VPI cycles. Dark areas are P3HT and lighter areas are ZnO. Nucleation is visible at 38 cycles. Film thickness is observed to increase with increasing cycle number.*[12]

Photovoltaic devices built from these films exhibit performance comparable to pure P3HT below 25 infiltration cycles, with photoconductivity transient times ($\tau_{1/2}$) around 0.25 μs. These transient times increase to 100 μs at 38 to 55 cycles. However, $\tau_{1/2}$ decreases again at higher cycle numbers (~35 μs at 75 cycles). This decrease in $\tau_{1/2}$ is attributed to the coalesced ZnO network leading to higher electron mobility and faster recombination kinetics. Higher exciton dissociation yields and electron mobilities measured via photoelectron density vs. voltage curves further support this conclusion.[12]

1.5.5. Contrasting Agent for Multi-Phase Polymer Imaging

VPI has also been used as an imaging agent in block co-polymer structures. By infiltrating PS-*b*-PMMA with Al_2O_3, Segal-Peretz *et al*. have improved 3D imaging of the structures inside self-assembled block copolymers (**Figure 23**).[16] The alumina works like a staining agent and selectively reacts with PMMA, thus increasing the z-contrast between PMMA and PS domains for scanning transmission electron microscopy (STEM) tomography imaging. Similar approaches would likely be relevant for micro-CT (computed tomography) x-ray imaging.

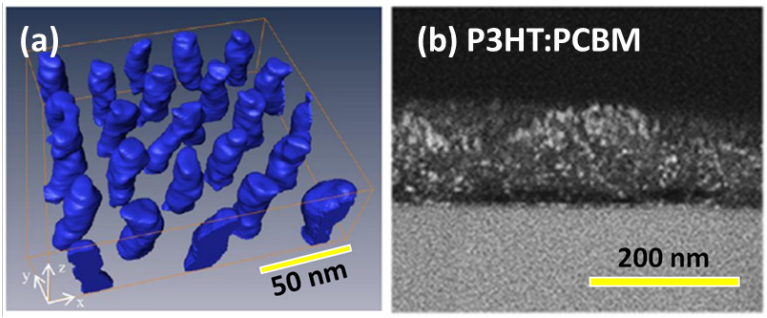

Figure 23: *(a) STEM tomography image of PMMA blocks in a PMMA-b-PS BCP using TMA VPI as a contrasting agent.[16] (b) Cross sectional backscatter electron SEM micrograph of P3HT:PCBM infiltrated with DEZ. ZnO acts as a contrasting agent (bright regions) for the P3HT domains.[55]*

Obuchovsky *et al.* obtained similar contrast using SEM to image P3HT / PCBM organic photovoltaic bulk heterojunctions.[55] Because these two materials have similar z-contrast, they cannot be spatially differentiated in an electron micrograph. By selectively introducing a metal oxide via VPI to the amorphous P3HT domains, the three dimensional structure of P3HT / PCBM domains could be visualized. Using this technique, these researchers were able to determine the maximum solubility of PCBM in P3HT (~17 wt%). Phase separation was immediately evident at higher concentrations. Using VPI to image phase separation in bulk heterojunction organic solar cells could be critically important to further advancing device performance.

2. STATEMENT OF PURPOSE

Compared to solution synthesis of organic-inorganic hybrid materials, vapor phase infiltration offers a number of potential advantages including advanced geometries and new chemical compatibilities. Many works have shown applications of VPI, and some have studied possible chemical reaction pathways between different precursors and polymers. However, the kinetics of VPI is still not well understood, which prevents accurate control of the extent of material transformation. This thesis develops a kinetics and thermodynamics processing theory that serves as a framework to accurately control infiltration depth and the concentration of inorganic loading through an experimentally-validated kinetics model. The theory is then applied to achieve desired properties in VPI created hybrid materials. New material properties from VPI that give additional insights to the processing theory are also analyzed.

2.1. Objective #1: Kinetics Modeling

Maximizing infiltration depth is crucial toward expanding application space (**Figure 24**). Being able to control the exact infiltration depth into a material is also important and therefore requires extracting the necessary values to fit the mathematical model discussed in Section 1.3. The simplest setup for a model uses a polymer film on a non-porous substrate to create a one-dimensional diffusion problem based on Fick's second law. While this mathematical model may not be sufficiently sophisticated to capture all of the complexity of VPI processing, which involves both diffusion and reaction, it is a useful first-step in understanding the mechanisms of VPI processing and serves as a foundation for future model development.

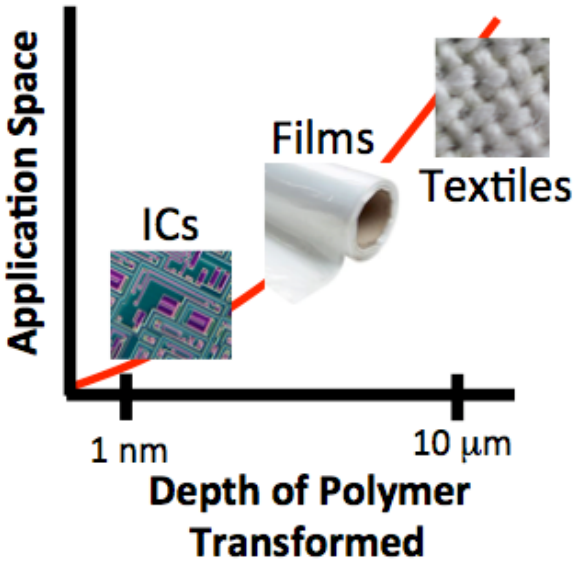

***Figure 24**: Schematic depiction of how an understanding of processing kinetics would enable VPI to impact more product and technology spaces.*

2.1.1. Tools and Approaches for Studying VPI Kinetics

In this thesis, both *ex situ* and *in situ* characterization methods were used to extract data to validate the infiltration processing theory. The following *ex situ* characterization tools have been used to characterize the samples before and after VPI:

- Ellipsometry
- Secondary ion mass spectrometry (SIMS)
- Scanning electron microscope with energy dispersive X-ray spectroscopy (SEM/EDX)
- Fourier transform infrared spectroscopy (FTIR)

Measurements using ellipsometry provide swelling data, which can be used as a proxy for total infiltration amount. SIMS can map the TMA concentration profile as a function of depth into the film to fit to the time-position dependent diffusion model. SEM/EDX and FTIR provide visual and chemical analyses of the films, respectively.

While the *ex situ* characterization methods show how VPI affects films once they are taken out of the reactor, these methods are used after the films have been purged and

exposed to water, and certain phenomena that are unique to a specific VPI step can be overlooked. *In situ* characterization of ongoing infiltration processes can give more accurate data on how the films behave during each VPI step. As part of this thesis, a VPI reactor capable of *in situ* characterization methods via quartz crystal microbalance (QCM) was built. The QCM system utilizes a temperature-controlled sensor head for testing different processing temperatures.

2.2. Objective #2: Investigating Hybrid Material Properties

Precursors infiltrating reactive polymers create chemical reactions that can alter the material properties of the original polymer material. Cross-linking may even occur for certain polymer-precursor systems, which may lead to higher chemical and mechanical stability.[57] Thus, studying changes in material properties of treated films can open up novel applications of these hybrid materials.

2.2.1 Chemical and Physical Changes of VPI-Treated Polymers

Whereas regular polymers can easily dissolve in a variety of organic solvents, VPI-treated polymers can behave quite differently. The precursors can introduce covalent metal oxide bonds on polymer chains and thus alter the polymer's chemical behavior. Precursors that have reacted and attached themselves onto polymer chains may have leftover organic ligands that can react with water to form hydroxyl groups. These hydroxyl groups can then absorb water from the atmosphere and increase water affinity for the VPI-treated polymers. A single precursor molecule can also crosslink polymers by reacting with multiple functional groups from different polymer chains. A crosslinked material can display reduced solubility in organic solvents. Even without crosslinking, inorganic ligands on former polymer functional groups may reduce the new material's affinity toward organic solvents.

2.2.2. VPI Processing on Selectively Reactive Polymers

Polymers without any functional groups should not react with precursors, while polymers that have functional groups, especially hydroxyl groups, can react very quickly with precursors. For this project, random co-polymers of poly(styrene-co-2-hydroxyethyl acrylate) (PS-r-PHEA), which contain a small fraction of chemically bonded hydroxyl groups, were treated with VPI. Changing the percentage of hydroxyl groups in an otherwise inert polymer can theoretically tune the reactivity of the final polymer. The theory is that inert polymers "doped" with a small percentage of functional groups may not be affected by VPI treatments, but inert polymers doped with a greater percentage of functional groups may react noticeably with precursors and effectively behave like a hybrid material.

3. EXPERIMENTAL METHODS

Experiments consist primarily of modifying and characterizing polymer films spun-cast on impermeable substrates like silicon for *ex situ* studies and QCM crystals for *in situ* studies. Using the film-on-substrate approach, we can easily model the precursor infiltration kinetics into the film and study new properties of these hybrid films.

3.1. VPI for *Ex situ* Analysis

PMMA films spun-cast on silicon substrates and infiltrated with TMA at different processing conditions were used as a prototypical system for studying the 1-dimensional VPI processing kinetics (**Figure 25**). The TMA-PMMA system has been commonly studied in past VPI work given that TMA can chemically react with PMMA functional groups, such as the carbonyl group. PMMA (MW = 15 kDa, T_g = 105 ^oC, Sigma-Aldrich) films were spun-cast from solutions of toluene for thinner films (< 200 nm) or cyclohexanone for thicker films (up to 1.5 μm). Spin-casting at 3000 rpm for 60 s from toluene (2 wt% to 6 wt% PMMA) gave films ranging in thickness from 50 nm to 200 nm. Higher concentrations of PMMA could be dissolved in cyclohexanone (up to 20 wt%). These solutions were used to prepare thicker PMMA films up to 1.5 μm. After spin coating, films were placed in a vacuum oven at 160^o C for $\geq$ 1 hour to remove trapped solvent and relax the polymer chains. This annealing step reduces film thickness by about 10% from the original spun-cast state.

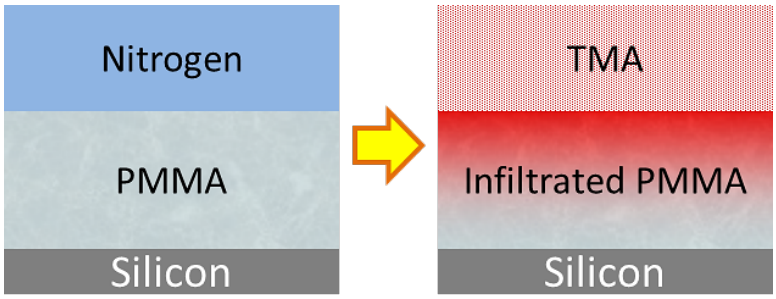

Figure 25: *Schematic of TMA VPI on PMMA films spun-cast on silicon substrates.*

VPI was performed in a custom-built reactor specifically designed for infiltration (**Figure 26**). Two gate valves are incorporated to permit isolation of the reaction chamber in a static VPI atmosphere. By connecting VPI precursors directly to the static reactor, we can better control dosing time and vapor concentration, enabling more fundamental studies of the processing kinetics. Single dose infiltration tests of TMA into PMMA were carried out over a temperature range of 60 ^{o}C to 130 ^{o}C and at exposure times ranging from 1 second to 1000 minutes. (**NOTE**: ***TMA is pyrophoric and must be handled with caution***.) This processing temperature range covers the glass transition temperature (T_g = 105 ^{o}C) of PMMA. Before each infiltration test, the samples were purged with ultra-high purity N_2 for 5 minutes at 150 sccm inside the VPI reactor to allow adequate removal of water and other impurities. The reactor was then pumped down to base pressure (~20 mTorr) for 2 minutes before the two gate valves were closed to isolate the chamber. TMA is then dosed for 1 second directly into the chamber through a diaphragm valve to a pressure of approximately 0.5 Torr. TMA infiltrates the PMMA films for a predetermined time before the gate vales are re-opened and the chamber is purged with about 2 Torr of N_2 for 60 s followed by a 1 s water dose to react with any residual TMA within the film or inside the chamber. We assume that once the material is exposed to water, all TMA becomes trapped within the PMMA film (no further desorption).

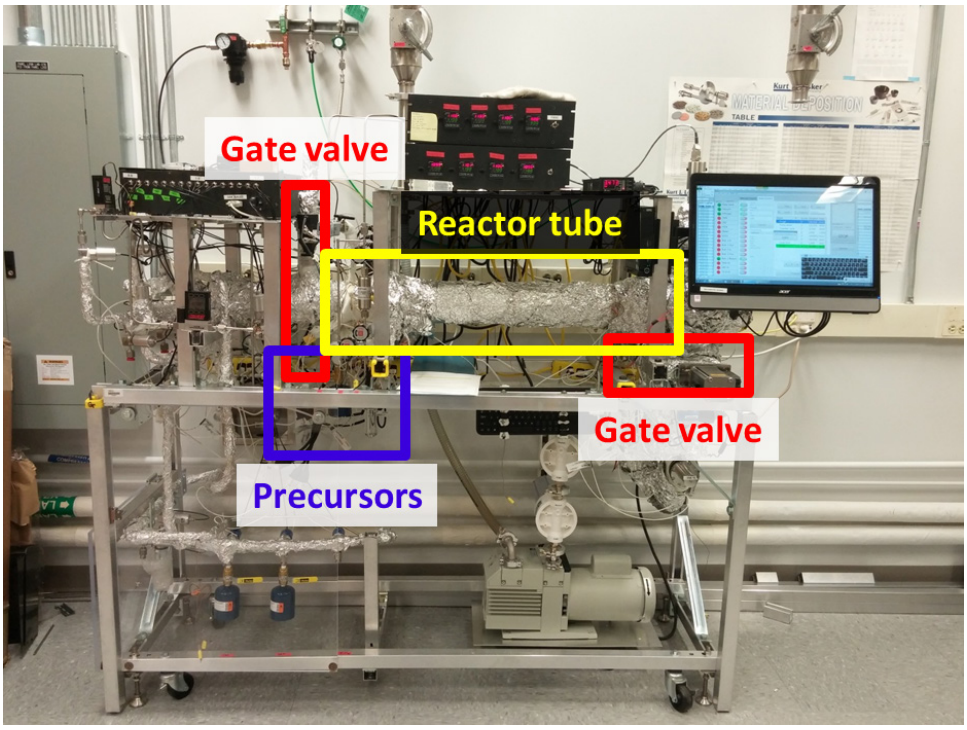

***Figure 26**: Picture of home-made reactor capable of both ALD and VPI. Gate valves (boxed in red) allow precursors dosed from bottles (boxed in blue) to remain inside the main reactor chamber (boxed in yellow) for an arbitrary amount of time. This allows precursors to diffuse into the polymer samples.*

3.1.1. Using Ellipsometry for *Ex situ* VPI Characterization

Swelling of PMMA films was measured *ex situ* with spectroscopic ellipsometry (Woollam Alpha-SE) immediately after VPI treatment. These swollen thicknesses were used as a proxy for total mass uptake by the polymer as a function of time. To measure infiltrated thickness with ellipsometry, films were modeled as a single homogeneous layer with some allowance for adjusting refractive index away from that of pure PMMA to achieve mean square error (MSE) values below 5 for most samples. Ellipsometry models that included roughness and/or graded layers showed no significant improvements in data fitting or changes in layer thickness since the refractive indices of pure PMMA and amorphous aluminum oxide are within 10% of one another. Because infiltration rate increases with higher temperature, films of different thicknesses were used across the temperature range. This ensures that films can reach maximum swelling

within reasonable times without saturating too quickly. To achieve sufficient temporal resolution for the diffusion process, PMMA films of about 150 nm thick were used for process temperatures lower than 100 ^{o}C, and 500 nm thick films were used for process temperatures above 100 ^{o}C.

3.1.2. Using SIMS for *Ex situ* VPI Characterization

Aluminum concentration depth profiles of the infiltrated PMMA films were measured with time-of-flight secondary ion mass spectrometry (ToF-SIMS, IONTOF, 5 Series). For simplicity, only infiltration profiles that could be fit to a semi-infinite diffusion model were evaluated; in other words, no diffusion profile was permitted to reach the substrate in these SIMS studies. To accommodate this constraint, thicker films (~1.4 microns) or shorter infiltration times were used. SIMS spectra were collected using oxygen sputtering (150 μm x 150 μm) and bismuth analyzer beams (50 μm x 50 μm). Positive polarity was used to detect the Al+ signal from infiltrated TMA.

3.1.3. Calibrating and Normalizing SIMS Data

The sputter rate for SIMS depth profiles is calibrated using a contact profilometer to measure the depths of craters from different sputtering times. **Figure 27** shows the correlation between sputter time and sputter depth of untreated PMMA and PMMA fully treated with TMA VPI at 70 ^{o}C and 170 ^{o}C. Treating the polymer with TMA VPI does not significantly change the sputter rate of the material, which from the trendlines in **Figure 27** is about 0.1 nm/s for both treated and untreated PMMA. This rate was then used to create the x-axis depth in each of the SIMS depth profiles.

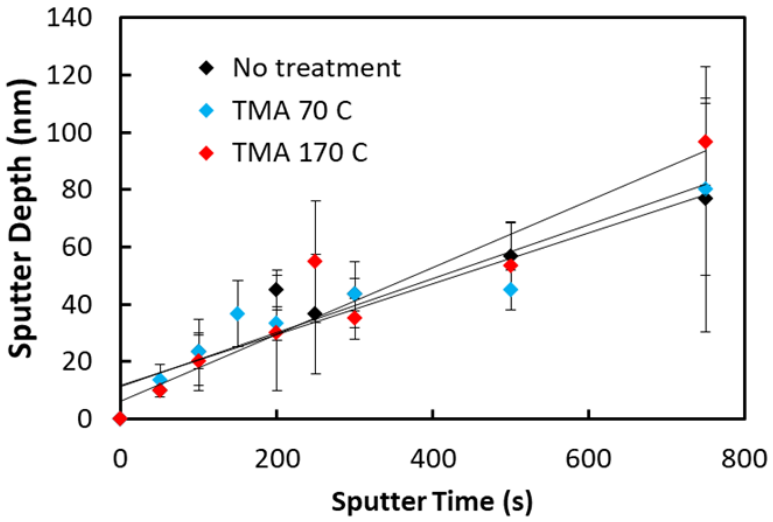

Figure 27: *Sputter depth as a function of sputter time for untreated PMMA, PMMA fully treated with TMA VPI at 70 ^{o}C, and PMMA fully treated with TMA VPI at 170 ^{o}C.*

The intrinsic instability of the SIMS analyzer beam creates noise in the SIMS signal. The top image in **Figure 28** illustrates this raw data and how the noise in each elemental signal follows the noise in the total signal caused by instabilities of the beam. In the bottom image of **Figure 28**, we show how normalizing the raw signal data from each concentration profile to the total count of all ions collected can eliminate this noise. This post-processing was done to all SIMS data prior to analysis.

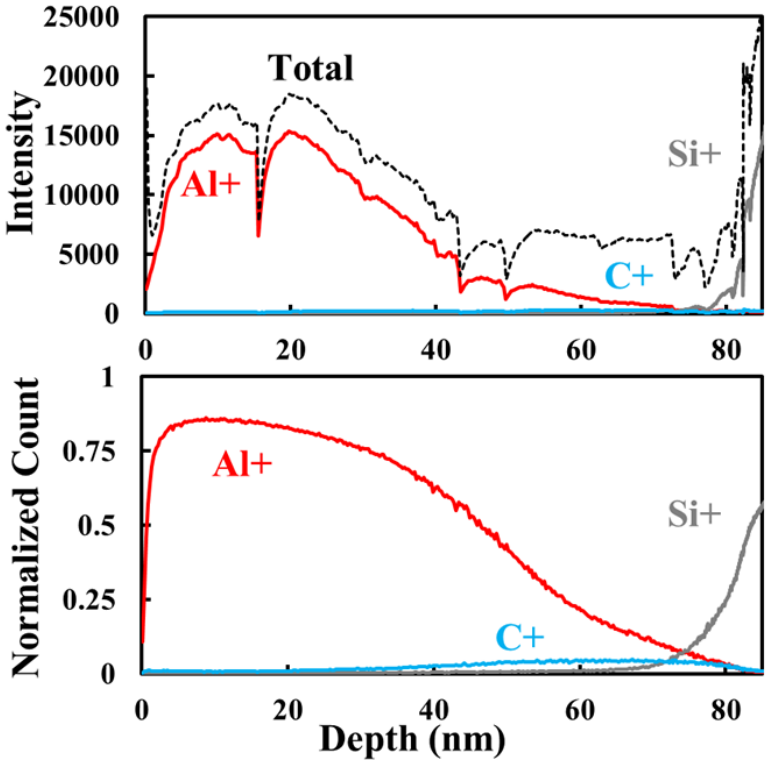

Figure 28: *(Top) Raw SIMS intensity data and (Bottom) normalized SIMS data for Al+, C+, and Si+ as a function of depth into a PMMA sample treated with TMA VPI for 10 s at 70 °C. In the raw intensity profile (top), the black dashed line indicates the total intensity of all detected ions.*

Figure 29 shows the solution to Fick's second law for normalized distance, concentration, and non-dimensional time. Note that the shape of this concentration profile does not match the shape of the SIMS concentration profile shown in **Figure 28b** above. This difference in shape is because the theoretical model provides a normalized concentration profile for a single constituent while the SIMS data is the atomic percent of that constituent relative to all other constituents.

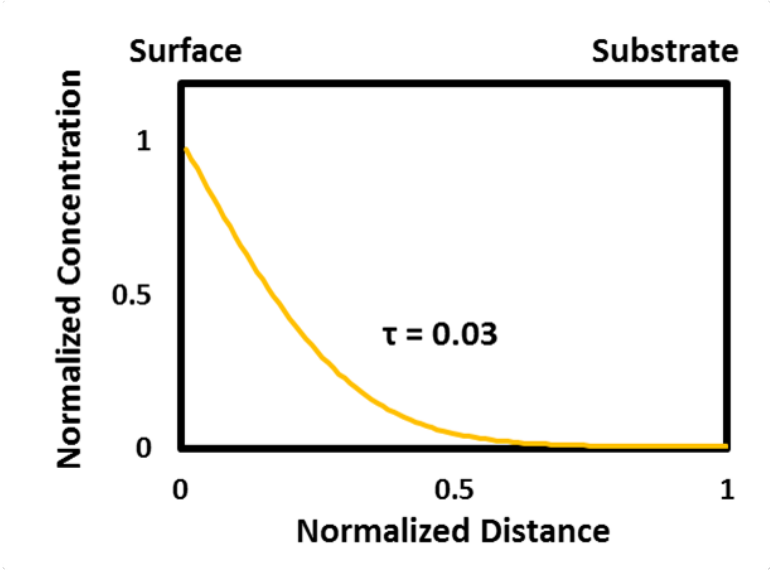

Figure 29: *Representative diffusion equation with normalized distance, concentration, and non-dimensional time.*

To match the theoretical concentration profile to the collected SIMS data, we assume that the other constituents have a constant concentration profile with depth. (See below for verification of this assumption.) **Figure 30** plots the original theoretical concentration profile of the penetrant (Al) with a solid yellow line and the assumed constant background concentration of constituents with a solid blue line. Because positive aluminum ions give off much stronger signal intensities than carbon or other organic ions in the film, the percentage of signals from aluminum ions can exceed 90% of the total signal from all measured ions in a TMA-infiltrated film. The "total" count of constituents (dotted blue line) is calculated by adding together the solid yellow and solid blue lines. Finally we calculate the percentage of aluminum by dividing the penetrants numerical count (solid yellow line) by the total count of constituents (dotted blue line) to get the percent concentration of penetrant (dotted yellow line). Note how this dotted yellow line now has the appropriate functional form to match the collected SIMS data.

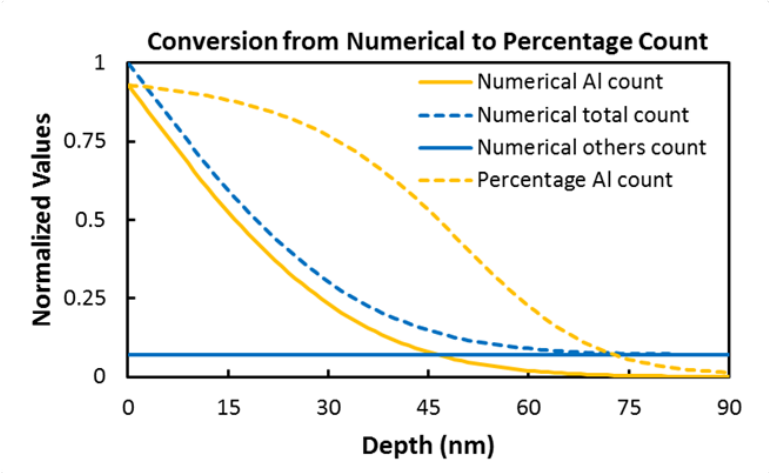

Figure 30: *Plot of various counts as a function of depth assuming a high penetrant signal.*

In **Figure 31** we plot representative raw SIMS signals for aluminum and carbon in a VPI treated PMMA film (partially infiltrated). As illustrated in this plot, the carbon signal intensity is nearly constant with depth, consistent with our assumption above.

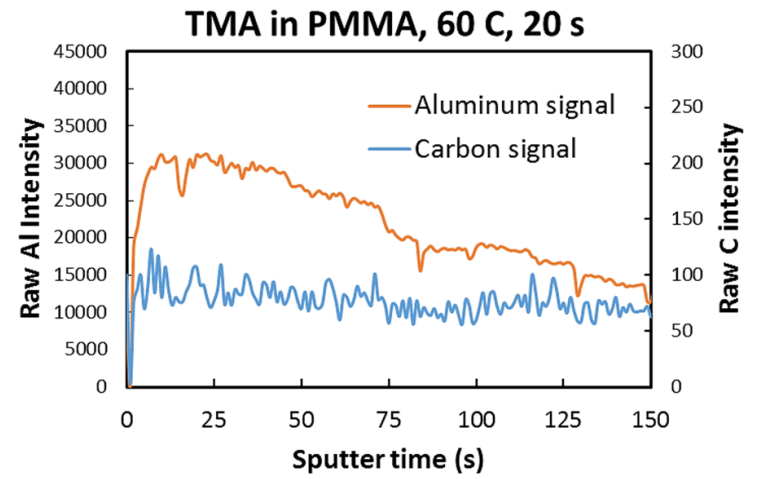

Figure 31: *Raw intensity of aluminum is plotted with raw intensity of carbon as a function of sputter depth into the film. The aluminum signal decreases while the carbon signal stays constant.*

3.1.4. Using FTIR for *Ex situ* VPI Characterization

Fourier transform infrared spectroscopy (FTIR, Thermo Scientific, Nicolet iS5) with a germanium ATR crystal was used to characterize changes within the PMMA chemistry due to VPI processing. To avoid signal interference from the silicon substrate, 1.4 micron thick PMMA films were used for these measurements.

3.1.5. Using SEM/EDX for *Ex situ* VPI Characterization

Cross sections of infiltrated films were visualized with a Hitachi SU8230 SEM with EDX. To prepare cross sections, films on pieces of single crystal silicon wafers were broken in half via a small crack initiated from a diamond scribe. These fractured pieces were then attached with carbon tape to vertical SEM stubs. Approximately 10 nm of carbon was sputtered onto the cross-section to prevent charging but not block the EDX signal. SEM images were taken at an accelerating voltage of 0.5 kV. EDX was taken using an accelerating voltage of 4 kV to reduce film damage but provide sufficient energy to emit characteristic K-shell x-rays from the aluminum atoms (~1.5 keV).

3.2. VPI for *In situ* Analysis

3.2.1. Using QCM for *In situ* Measurements of VPI Kinetics

In situ characterization of the VPI process can be accomplished by measuring mass changes through a quartz crystal microbalance. The crystal is piezoelectric quartz that oscillates through an alternating electric field to form a standing wave. A polymer film is spun-cast onto the crystal, and mass changes from precursor infiltration into the film cause the crystal resonance frequency to shift, which in turn can be calculated for precise mass changes. The Sauerbrey equation (**Equation 23**) is used to calculate mass change

from frequency change data. Frequency is also dependent on temperature, and thus temperature control of the crystal is necessary.

3.2.2. Building the *In situ* VPI Characterization Reactor

Figure 32 shows the current build for this reactor, which primarily consists of a 6-way cross with 2.75" CF flanges connected to various ports and feedthroughs. The entire reactor can be heated via heat tapes underneath aluminum foil covers to reduce water and other contaminant buildup inside the reactor walls. The reactor functions can be controlled via a LabVIEW program.

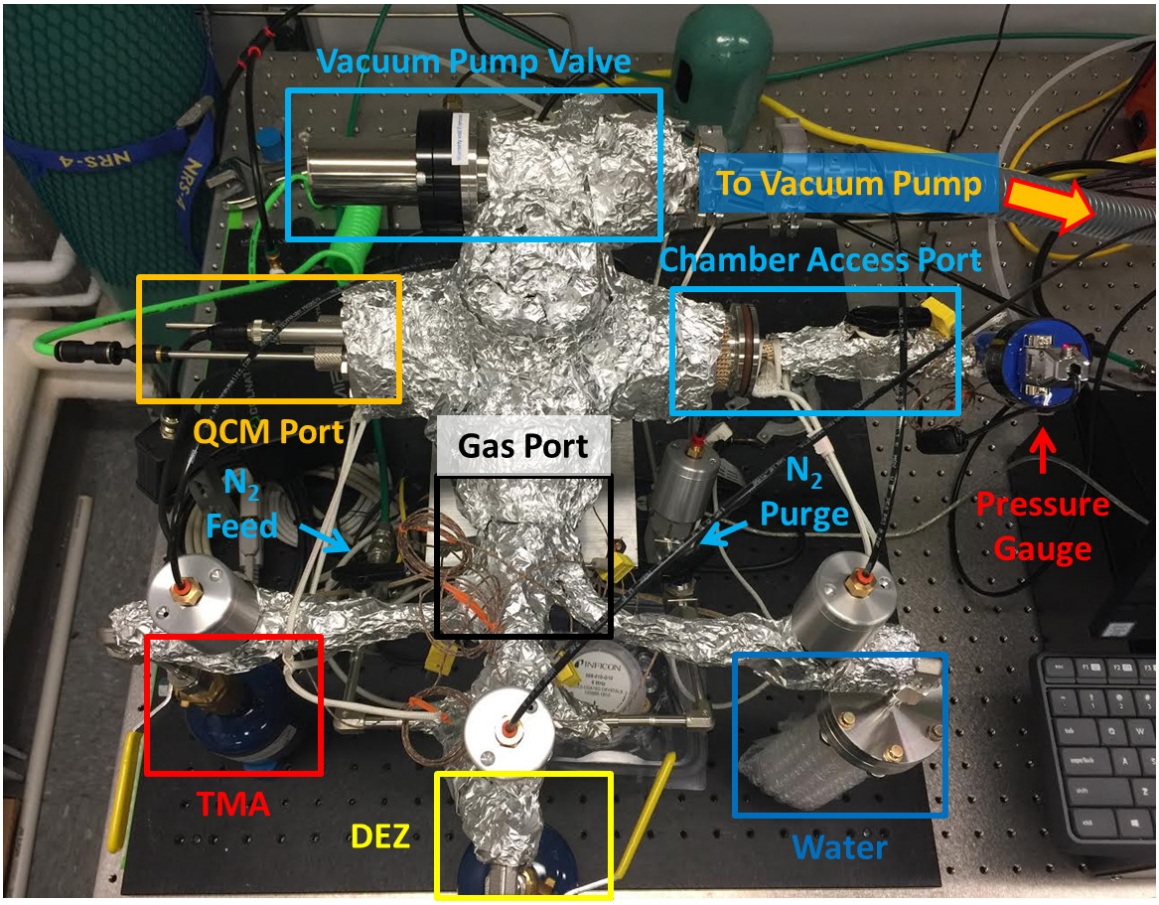

Figure 32: *Top-down view of the in situ VPI characterization reactor with labeled ports and other components.*

For the chamber access port, a CF to KF adapter is installed for ease of sample change through a KF connection, which utilizes a rubber o-ring instead of a copper compression ring bolted between CF flanges. Although KF flanges do not seal as well as CF flanges, ultra-high and ultra-clean vacuum is not needed for these experiments since VPI is not designed to create precise surface chemistries that are sensitive to small amounts of contaminants. Connected to the removable KF cap is a Baratron pressure gauge for reading the chamber pressure. This design frees up space at other ports, and the gauge is light enough where atmospheric pressure is more than sufficient at keeping the cap tightly pressed against the KF adapter flange.

The gas feedthrough port consists of four ¼" stainless steel tubes welded into the CF flange. One tube transports in nitrogen from either the purge line (high purity N_2) or the feed line consisting of low purity N_2 to bring the reactor up to atmospheric pressure. Both N_2 lines have manual shutoff valves, although the purge line also has a pneumatic valve to allow programmed purges. Because the N_2 pressure or flow rate during purge does not need to be precise for VPI purposes, the manual shutoff valve attached to the purge line allows rough control of the N_2 purge pressure inside the reactor. TMA, DEZ, and water are each fed through the gas port via individual tubes and controlled by pneumatic valves.

The QCM system (Tempe System, Colnatec) on the QCM port collects *in situ* gravimetry data inside the chamber. The system has a temperature controlled sensor head that can maintain a set temperature for the QCM crystal up to 500 ^{o}C. The sensor head can move into and out of the chamber along a 10" arm fitted to compression fitting valves at the port flange. The arm consists of two ¼" stainless steel tubes that can flow cool, compressed air from the green plastic gas line through the sensor head for accurate temperature control within 1 ^{o}C. The flexibility of allowing the sensor head to move out of the chamber in turn allows the QCM system to be bolted to the chamber using CF flanges.

The pump port located in the back of the reactor connects the reactor chamber to the filter and vacuum pump system through a 1.5" PVC tubing reinforced with spiral wire. A pneumatically controlled angled gate valve can be programmed to control when the

reactor is being pumped down as opposed to holding in precursors during the infiltration stage of VPI.

The top CF port is currently blanked off but can be fitted with a quartz viewport for future *in situ* optical measurements of polymer films inside during VPI. In addition, a residual gas analyzer can also be fitted to the top flange for additional chemical characterization.

The bottom CF port is blanked off and serves as an anchor to hold the entire reactor in place through six threaded rods bolted to the table.

3.2.3. Experimental Methods with QCM System

VPI parameters follow closely with those described for *ex situ* analysis with the main exception that PMMA films were spun-cast onto polished, alloy-coated QCM crystals instead of silicon wafers. The alloy is a proprietary material from the vendor (Phillip Technologies) that provides high mechanical strength to the crystal. To ensure electrical contact between the electrodes and sensor head, each crystal was gently wiped with toluene around the edges to remove any polymer after spin-casting. A single crystal was then placed inside the QCM sensor head via a twist-cap arrangement. The QCM sensor head is heated via its internal heater to a set temperature between 60 ^{o}C and 130 ^{o}C, and temperature is maintained within 1 ^{o}C by a PID controller in the QCM system. To maintain a crystal temperature of 60 ^{o}C, the maximum heater input is limited to 30%, and the proportional, integral, and differential values for the system are 5000, 60, and 30, respectively. The large proportional value is needed to respond rapidly to the binary, on-off nature of the cooling mechanism. Smaller proportional values would result in repeated temperature oscillations of over 5 ^{o}C around the set temperature. Because QCM crystals are very sensitive to temperature changes, maintaining a set temperature as accurately as possible is required to prevent artificial mass change readings caused by temperature swings. A maximum heater input of 50% is used to maintain a crystal

temperature of 130 ^{o}C, and PID values are unchanged regardless of temperature within this 60 ^{o}C to 130 ^{o}C range.

The QCM allows *in situ* measurements of both precursor absorption (adsorption + infiltration) and desorption, from which diffusion coefficients and various energy values can be extracted. Both absorption and desorption data is collected with the same film. The infiltration time for complete TMA absorption into PMMA films on the QCM crystals is set using diffusion coefficient values extracted from *ex situ* ellipsometry and SIMS data. After complete infiltration (no more significant mass gains), the films are purged with nitrogen at about 3 Torr for a long time until mass stops decreasing. Data recorded during this entire run is fitted to the diffusion model to extract diffusion coefficients for both absorption and desorption of TMA. The recording frequency is one measurement per second.

3.3. Material Properties

With a deeper understanding of VPI kinetics, we use our processing model to infiltrate polymers to precise depths and explore the changes to the resulting hybrid material's properties for application potentials. Studying the hybrid material's properties can also give us more information on how precursors are interacting with and changing the polymers. In this section, we explore the solubility of VPI-treated polymers in various solvents, moisture absorption capability of fully treated polymers in air, and behaviors of selectively reactive polymers when treated with VPI.

3.3.1. Measuring Solubility of VPI-Treated Polymers

For this chemical stability study, spun-cast PMMA films on silicon substrates were infiltrated with TMA at processing temperatures ranging from 70 to 170 ^{o}C. The degree

of infiltration was controlled by varying TMA exposure times according to our TMA-PMMA diffusion model.[50]

The chemical stability test was done by first measuring the initial thickness of the treated PMMA films and then immersing the films in individual vials filled with one (or a combination) of the following solvents: toluene, cyclohexanone, tetrahydrofuran, chloroform, acetone, isopropanol, ethanol, and water. The films were then taken out at predetermined intervals, blow dried with N_2, and then measured for thickness again before being placed back into the solvent. Interesting features observed during the chemical stability tests were characterized using confocal microscopy (Olympus LEXT 3D) with both optical and laser capabilities.

In addition to studying chemical stability in PMMA films, I also tested macro samples to see if infiltrating TMA into the subsurface of bulk PMMA can shield the interior PMMA from solvents. I laser cut two school mascot pictures for Georgia Tech and UGA on acrylic (PMMA) panels to yield samples of about 10 cm in size and 0.6 cm in thickness (**Figure 33**). The laser engraved textures of about 20 to 50 microns deep into the panels to give a milky appearance in some places. I then treated the acrylic panel depicting the Georgia Tech mascot with TMA VPI at 100 ^{o}C for 17 hours using a single dose and hold method. Finally, the two panels were placed in heated toluene at 60 ^{o}C for 10 minutes to speed up any degradation before they were removed to dry.

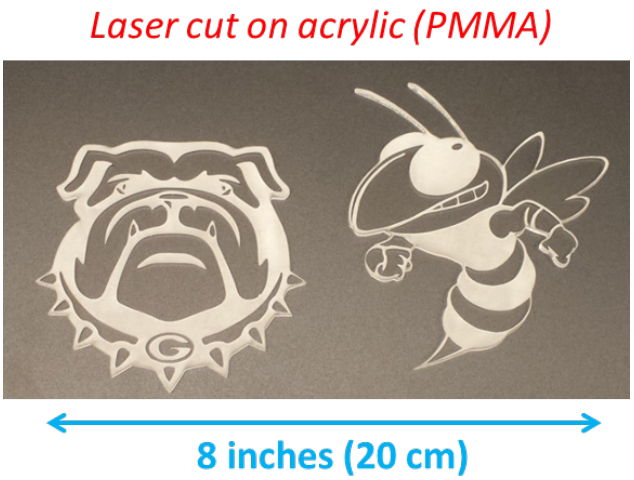

Figure 33: *Acrylic cutouts of mascots for UGA (left) and Georgia Tech (right). The milky sections are due to laser-engraved textures in the otherwise clear panels.*

3.3.2. Moisture Absorption of VPI-Treated Polymers

Infiltrated TMA can have leftover methyl groups that will react with water to form hydroxyl groups. To test the effects of hydroxyl groups on infiltrated PMMA, I placed PMMA films treated with TMA VPI at 70 ^{o}C, 100 ^{o}C, and 130 ^{o}C onto a homebuilt heated ellipsometry stage (**Figure 34**) and measured the film thicknesses as a function of temperature. The stage temperature was raised gradually at a rate of about 0.1 ^{o}C/s from 25 ^{o}C to 160 ^{o}C and then lowered back down to about 30 ^{o}C. Film thicknesses were measured in 5 degree increments during both heating and cooling. The same heat test was also done on a pure, untreated PMMA film for comparison, where coefficients of thermal expansion were then calculated from the slopes.

Figure 34: *Aluminum heated stage attached onto the ellipsometer stage. Temperature is controlled via a heating pad underneath the stage and a thermocouple connected to the temperature controller for accuracy within 1 ^{o}C.*

3.3.3. VPI Processing on Selectively Reactive Polymers

Random co-polymers of poly(styrene-co-2-hydroxyethyl acrylate) (PS-r-PHEA) were made by the Will Gutekunst group in Georgia Tech's chemistry department. The percentages of hydroxyls in the polystyrene are 0% (pure polystyrene), 0.5%, 1%, 3%, and 5%. The PS-r-PHEA were spun cast into thin films and treated with TMA VPI to study the overall polymer reactivity as a function of hydroxyl percentage. To make the films, PS-r-PHEA was dissolved in 4 wt% toluene solution and spun cast on silicon wafers at 3000 rpm for 60 seconds before placed on a hot plate at 90 ^{o}C to remove leftover solvents. The polymer films were then treated with single dose and hold TMA VPI. In order to study the reactivity of TMA in PS-r-PHEA at different processing temperatures, the films were fully infiltrated at either 70 ^{o}C or 100 ^{o}C (TMA exposure times of 300 minutes and 100 minutes, respectively). The TMA exposure time for a "full" infiltration is based on TMA infiltration kinetics using *in situ* QCM measurements of TMA infiltrating PS-r-PHEA. The films are fully infiltrated once QCM data indicate mass gains have stopped. After infiltration, the films were purged with nitrogen for either 1 or 1000 minutes before dosing water. The two purge times can show whether or not infiltrated TMA has undergone irreversible chemical reactions in the PS-r-PHEA at the two processing temperatures since longer purges should remove most of the unreacted TMA inside the polymers. Film thicknesses were measured before and after VPI treatment using spectroscopic ellipsometry (Woollam Alpha-SE). Increases in film thicknesses after VPI treatment indicate TMA loading inside the polymers.

We also tested the solubility of fully treated PS-r-PHEA in toluene since untreated PS-r-PHEA readily dissolves in toluene. How the treated films interact with toluene can tell us the effectiveness of the infiltration. For this solubility test, we fully treated PS-r-PHEA with hydroxyl concentrations of 1%, 3%, and 5% with TMA at 100 ^{o}C and then placed them in individual vials of toluene. We measured the film thicknesses of each film after a certain period of time until the film fully dissolved or a clear trend in thickness change is observed over several weeks of toluene immersion.

To extract thermal expansion coefficients of treated and untreated PS-r-PHEA films, we measured the film thicknesses as a function of temperature up to 160 ^{o}C using the heated stage on our ellipsometer. Film thicknesses were measured at 5 degree intervals during gradual heating and cooling (~0.1 ^{o}C/s).

4. VPI PROCESSING KINETICS

4.1. Kinetics of VPI

As shown in **Figure 2**, vapor phase infiltration is a three step process: 1) sorption of metalorganic gases in the polymer, 2) diffusion of the sorbed gases (penetrants) within the polymer, and 3) entrapment of penetrants within the polymer via either reaction or other mechanism (e.g., steric hindrance or loss of volatility).[50] Here, we fit data collected from both *ex situ* and *in situ* measurement methods to our kinetics model discussed in detail in Section 1.3 and extract energy values that allow better understanding of the thermodynamics and kinetics of the VPI process.

4.1.1. Model Fitting with Ellipsometry and SIMS Data

Figure 35 shows representative data illustrating our approach for extracting diffusion and solubility coefficients from SIMS depth concentration data and film swelling profiles. **Figure 35a** is a representative SIMS depth profile for an 80 nm PMMA film partially infiltrated with TMA for 10 s at 70 ^{o}C. **Figure 35b** fits this SIMS profile to **Equation 9** (dotted line) to extract an effective diffusion coefficient of the TMA penetrant in PMMA of 2.2×10^{-14} cm^2/s.

Figure 35c plots the PMMA film thickness (measured with ellipsometry) after VPI of various process times at the same process temperature (70 °C). We assume that film swelling is a reasonable proxy for the total mass uptake in the film as a function of VPI process time. As highlighted in **Figure 35d**, the saturation value for this mass uptake at long times divided by the process pressure should be proportional to the solubility coefficient (S) of the TMA in PMMA at that process temperature. The temporal dependence of the mass uptake data can be fit to **Equation 11** to extract an independent value for the effective diffusivity. Here we find the diffusivity at 70 °C to be 8.3×10^{-15} cm^2/s, similar to the value calculated with SIMS.

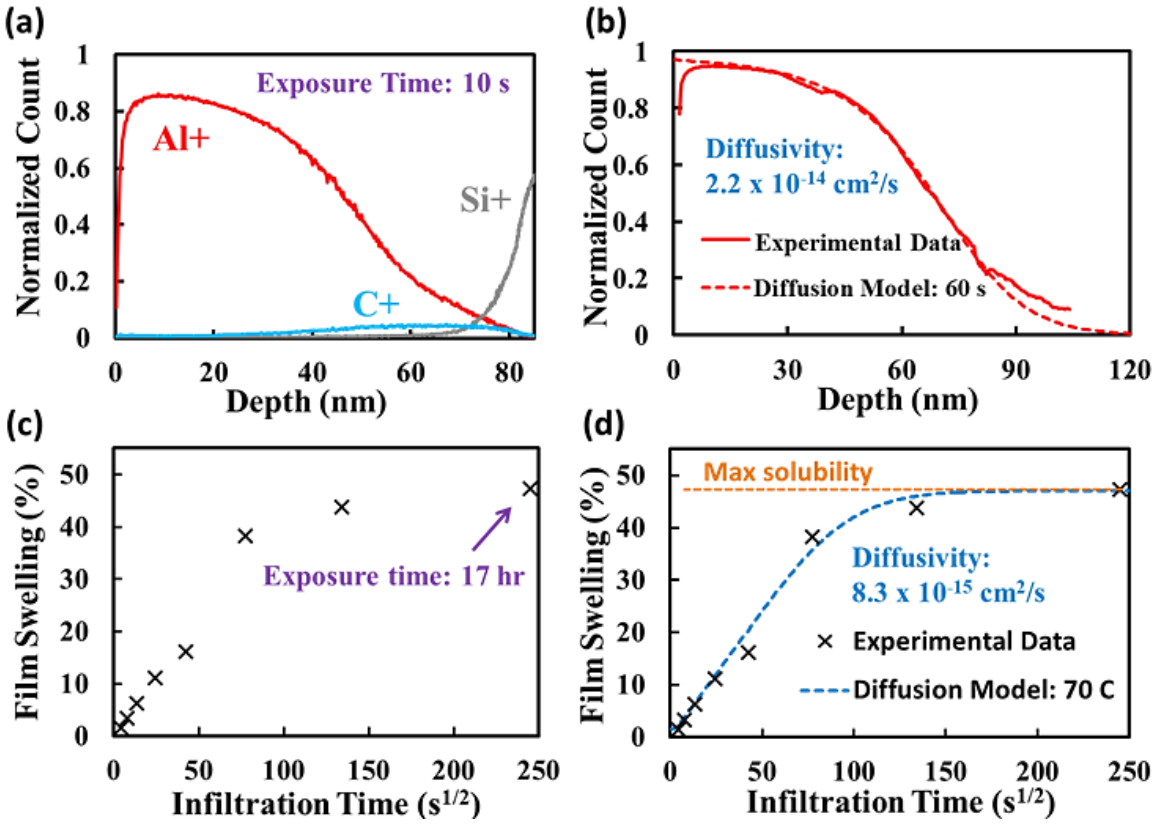

Figure 35: *(a) Normalized count of Al+, C+, and Si+ as a function of depth into an initially 80 nm thick PMMA film treated with TMA VPI for 10 s at 70 °C. (b) Fick's 2nd Law fit to the normalized Al+ SIMS concentration profile for a PMMA film treated with TMA VPI at 70 °C for 60 s. (c) Swelling data for an originally 150 nm thick PMMA film treated with TMA VPI at 70 °C. (d) Swelling data with fitted diffusion model and maximum solubility limit.*

4.1.2. Model Fitting with QCM Data

Figure 36 shows a representative plot of mass changes during TMA absorption and desorption at 100 °C in a PMMA film spun-cast onto a QCM crystal. The mass change is calculated by the QCM program after inputting a film density of 1.2 g/cm^3.

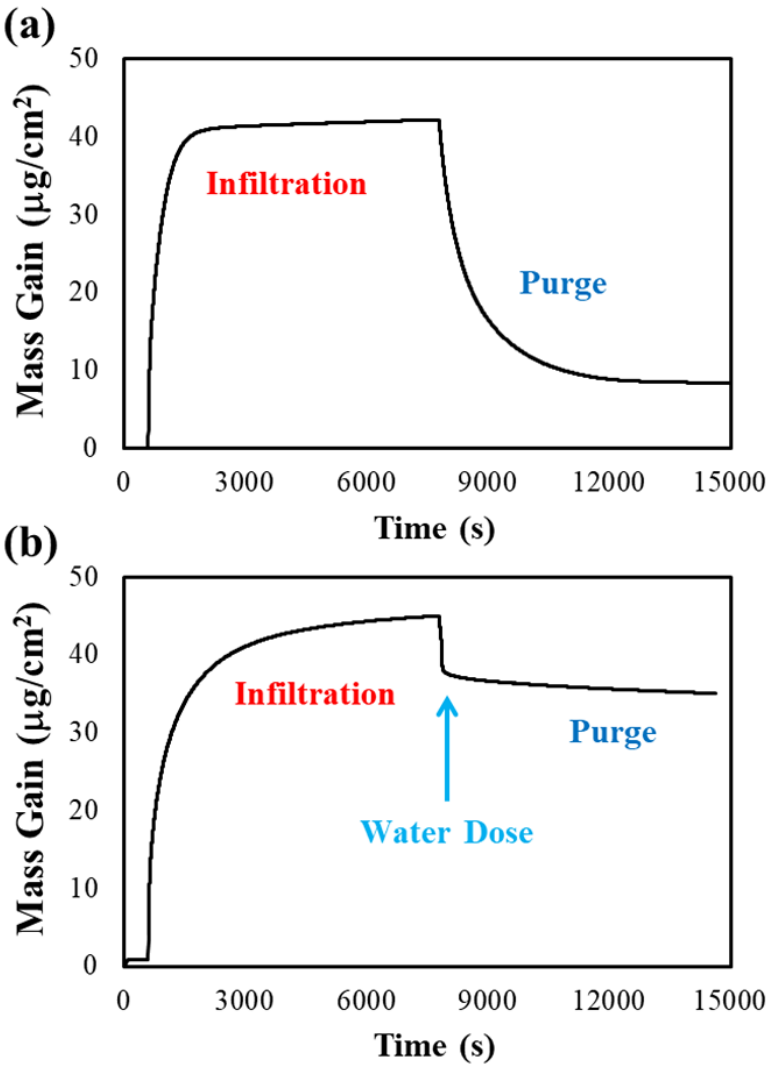

Figure 36: *Mass changes of PMMA during absorption and desorption of TMA at 100 °C. (a) No water is dosed during purge for the film with a thickness of 700 nm. (b) Water is dosed 60 seconds into the purge for the film with a thickness of 900 nm.*

4.1.3. Extracting Energy Values from *Ex situ* Characterization

In **Figure 37a**, we plot representative film swelling data collected at three different VPI process temperatures. Immediately evident is that as process temperature is increased, maximum film swelling decreases. We further qualitatively prove that sorption of TMA in PMMA decreases with increasing temperature. A sample of PMMA film on silicon with original film thickness of 135 nm is cut into three pieces, and each piece is fully

treated with TMA VPI at one of the three processing temperatures: 70 ^{o}C, 100 ^{o}C, and 130 ^{o}C. The three pieces are then placed in a furnace at 700 ^{o}C for 1 hour and exposed to air to burn off the film and leave behind a layer of aluminum oxide. The remaining alumina film thicknesses were measured with ellipsometry and reported in **Figure 38**. Consistent with film swelling, we see thicker Al_2O_3 films (more inorganic mass loading) at lower VPI process temperature. This temperature dependent change in maximum sorption can be used to evaluate the enthalpy of sorption (ΔH_s). **Figure 37b** plots the log of the solubility parameters for TMA in PMMA as a function of inverse temperature (Van't Hoff plot). These values were calculated by assuming that the concentration of TMA is a direct function of the swelling percentage. Because sorption capacity decreases with increasing process temperature, the overall sorption process must be exothermic. This exothermic behavior is consistent with usual measurements of sorption enthalpies of gases in polymers for membrane separations and can be generally attributed to the large exothermic enthalpy of condensation.[77-78] **Figure 38b** also indicates a change in the sorption enthalpy above and below 95 ^{o}C. Below 95 ^{o}C the ΔH_s is near zero (-0.03 eV). Above 95 °C, sorption enthalpy increases in magnitude to -0.33 eV (-31.8 kJ/mol).

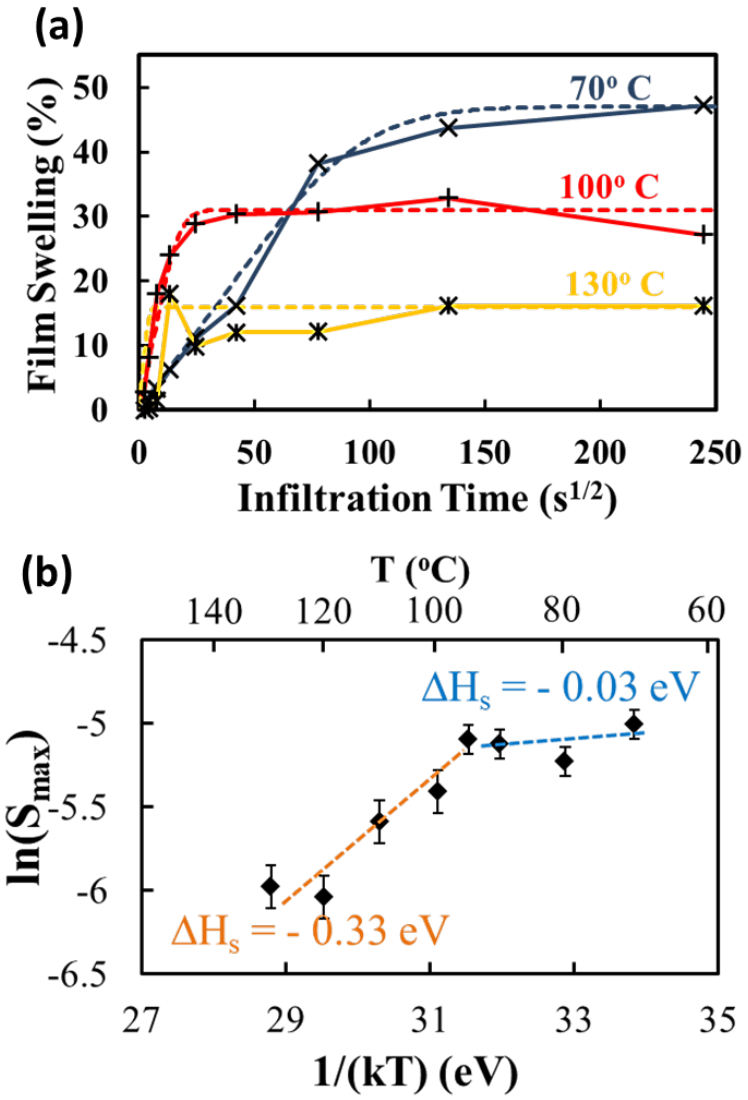

Figure 37: *(a) Plot of PMMA film swelling as a function of TMA VPI process time at three representative process temperatures: 70 °C, 100 °C, 130 °C. Dotted lines are regression fits to Fick's 2nd Law. (b) Van't Hoff plot of the maximum TMA solubility in PMMA as a function of VPI process temperature. Trend lines are added to visually indicate the change in sorption enthalpy at approximately 95 °C.*

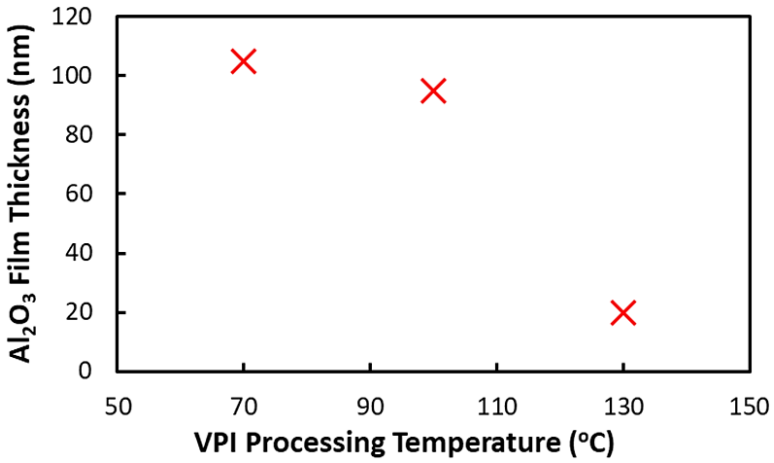

Figure 38: *Alumina film thickness after burn-off of PMMA films fully infiltrated with TMA at different processing temperatures. The original film thickness before VPI treatment is 135 nm for all three samples.*

Figure 39 plots the natural log of the effective diffusivity measured with both SIMS and ellipsometry as a function of inverse temperature for TMA VPI of PMMA over a process temperature range of 60 °C to 130 °C. These measurements agree well with one another, providing us confidence in our accuracy. Again, a distinct change in linear slope occurs at 95 °C. Below 95 °C the effective activation energy for diffusion is 0.8 eV while above 95 °C the effective activation energy for diffusion is 2.2 eV. A full list of these measured effective diffusivities as a function of temperature is provided in **Table 2**.

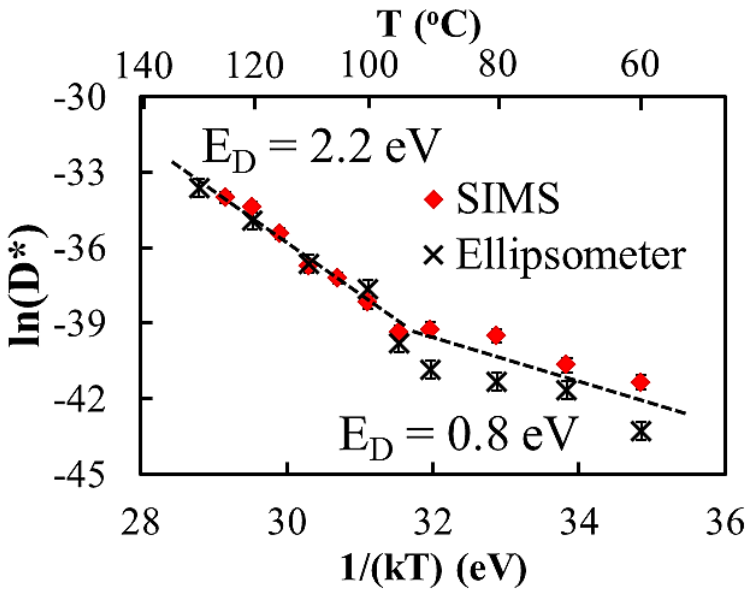

Figure 39: *Arrhenius plot of the effective diffusivity of TMA in PMMA as a function of VPI process temperature. Diffusivity data derived from both SIMS (red diamonds) and ellipsometry analyses (black x's) are included. Activation energies based on the slopes of the linear sections are reported. Linear regression fits (dotted lines) are added to visually emphasize the change in mechanism at about 95 °C.*

Table 2*: Summary of the effective diffusion coefficients measured for TMA VPI of PMMA calculated from SIMS and ellipsometry data at various process temperatures.*

Temperature (°C)	D_{SIMS}^{*} (cm^2/s)	$D_{Ellipsometry}^{*}$ (cm^2/s)
60	1.1×10^{-14}	1.6×10^{-15}
70	2.2×10^{-14}	8.3×10^{-15}
80	7.0×10^{-14}	1.2×10^{-14}
90	9.0×10^{-14}	1.9×10^{-14}
95	8.0×10^{-14}	5.2×10^{-14}
100	2.6×10^{-13}	4.4×10^{-13}
105	7.0×10^{-13}	-
110	1.1×10^{-12}	1.2×10^{-12}
115	4.0×10^{-12}	-
120	1.2×10^{-11}	7.0×10^{-12}
125	1.7×10^{-11}	-
130	-	2.5×10^{-11}

4.1.4. Precursor Sorption Theory

In the Van't Hoff plot for VPI sorption equilibrium (**Figure 37b**), we note a change in the sorption reaction mechanism above and below the new effective glass transition temperature of 95 °C. Specifically, the high-temperature rubbery state has a more exothermic enthalpy of sorption (-0.33 eV) than the low temperature glassy state (-0.03 eV). To better understand these enthalpies, it is useful to further partition this energy into several potential terms:[79]

$$\Delta H_S = \Delta H_{condensation} + \Delta H_{mix} \qquad \textbf{Equation 24}$$

The first term ($\Delta H_{condensation}$) is the condensation of the vapor to the condensed state. While the exact nature of this term is not fully agreed upon (it may be some form of a gas adsorption energy rather than the gas-to-liquid latent heat), it is certainly exothermic in nature and the primary reason for why the Van't Hoff slopes are usually positive for gas sorption equilibria. The second term, the enthalpy of mixing (ΔH_{mix}), can be endothermic or exothermic depending on the penetrant-polymer interaction energy (i.e., related to the χ parameter).

The Van't Hoff data in **Figure 37b** is substantially different from what is typically observed for small molecule (e.g., H_2O, CO_2, N_2, etc.) sorption in polymers.[77] In more commonly studied gas sorption systems, the ΔH_s is usually observed to become more endothermic above the glass transition temperature. This endothermic change in enthalpy is attributed to the loss of free volume, which makes gas molecule sorption energetically less favorable (the dual-mode sorption model) – only solution sorption remains active.[77, 80] Here, we observe the rubbery state to have a significantly more exothermic ΔH_s than the glassy state. We interpret this change in enthalpy as an indication of a change in the enthalpy of mixing (ΔH_{mix}) due to the formation of the organic-inorganic hybrid material. Unlike most commonly studied gas-polymer sorption systems, VPI processing uses gases that can react with the polymer and change its inherent chemistry. Thus, we believe the sudden exothermic change in sorption enthalpy above T_g is indicative of the precursor

molecule reacting with the polymer, creating a hybrid material that better mixes with TMA.

A second, more subtle, observation is the rather low exothermic value for the enthalpy of sorption for TMA in the glassy PMMA polymer (-0.03 eV). Most small gas molecule sorption enthalpies into glassy polymers are within the -0.1 to -0.3 eV range.[77] For example, CO_2 in PMMA has been measured to be -0.16 eV.[81] The low ΔH_s observed for this VPI process suggests the inclusion of another endothermic sub-process occurring upon TMA sorption. We propose this endothermic sub-process to be the de-dimerization of the TMA. Within our VPI process temperature range (< 140 °C), most of the vapor phase TMA is expected to be dimerized.[82] Consequently, as depicted in **Figure 40**, we propose describing the sorption of TMA into PMMA by three distinct steps: (1) condensation of the TMA vapor onto the PMMA surface, (2) dissociation of the dimerized TMA into individual TMA molecules, (3) dissolution (enthalpy of mixing) of the TMA into the PMMA:

$$\Delta H_S = \Delta H_{condensation} + \Delta H_{mix} + \Delta H_{dissociation} \qquad \textbf{Equation 25}$$

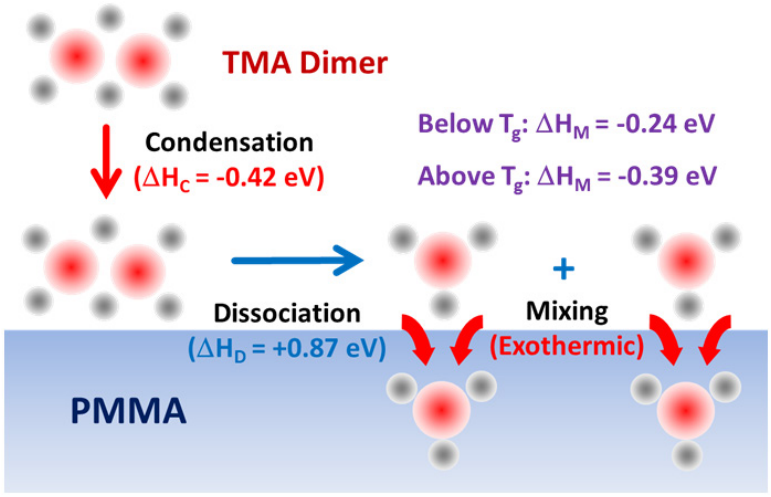

Figure 40: *Schematic of TMA sorption into PMMA assuming dimer dissociation. Exothermic processes are labeled in red, and endothermic processes are labeled in blue.*

Based on the above discussion, we attempt to further quantify the energies associated with these sorption sub-processes. From the literature, the enthalpy for condensation of

TMA in dimer form is approximately -0.42 eV (exothermic),[83] and the enthalpy for TMA dimer dissociation is +0.87 eV (endothermic).[82]

To calculate the enthalpy of mixing (ΔH_{mix}), we have subdivided sorption into three sub-processes as pictured in **Figure 40**: (1) TMA dimer condensation, (2) TMA dimer dissociation, and (3) TMA dissolution (mixing) into the polymer. We can write the following chemical reactions to describe these three sub-processes:

Condensation:	$(TMA)_2$ (v) → $(TMA)_2$ (ads)	ΔH_c = -0.42 eV
Dissociation:	$(TMA)_2$ (ads) → 2(TMA) (ads)	ΔH_{dissoc} = +0.87 eV
Mixing:	TMA (ads) → TMA (ss)	ΔH_{mix} = ?

We note that to arrive at these values, the solubility coefficient is assumed to follow Henry's Law: C = SP. Here, P is the partial pressure of the VPI process, which in this case is the pressure of the dimerized TMA molecule, not the individual TMA molecule. Therefore, the measured sorption enthalpy (ΔH_s) is for the reaction:

$$(TMA)_2 \text{ (v)} \rightarrow 2TMA \text{ (ss)}$$

Accounting for this stoichiometry, **Equation 25** in the text can be appropriately written as:

$$\Delta H_S = \Delta H_{condensation} + \Delta H_{dissociation} + 2 \times \Delta H_{mix} \qquad \textbf{Equation 26}$$

Thereby, the enthalpy of mixing is:

$$\Delta H_{mix} = 1/2 \times (\Delta H_s - \Delta H_{condensation} - \Delta H_{dissocaition}). \textbf{ Equation 27}$$

Accounting for the reaction stoichiometry, we can then use **Equation 26** to estimate that the enthalpy of mixing for TMA-PMMA to be -0.24 eV (single TMA) in the glassy state and -0.39 eV (single TMA) in the rubbery state. We caveat these derived values by re-emphasizing the assumptions made herein: (1) solution behavior is sufficiently dilute to follow Henry's Law, (2) the TMA sorbs dissociated, not as a dimer, and (3) the condensation step can be approximated from the latent heat of fusion.

4.1.5. Critical Processing Temperature

Prior research has used *in situ* FTIR to explore the chemical mechanisms of the TMA-PMMA VPI process.[18, 52] Despite the attention given to this system, the exact reaction pathway is still not very clear. TMA, as a strong Lewis acid, is expected to form a chemical adduct with PMMA's carbonyl groups. **Figure 41** shows two proposed reaction mechanisms of TMA reacting with carbonyl groups in PMMA.[18, 52] Further discussions of the chemical reactions that may occur during VPI can be found in a recent review by Parsons *et al*.[84] These studies have revealed noticeable differences in precursor-polymer "reactivity" above and below 100 °C, near the temperature that we measure abrupt changes in the enthalpies associated with solubility and diffusion for this system. Below ~100 °C, quasi-stable complexes form between the precursor and the polymer. At these low temperatures, this complex formation is reversible, and TMA can fully desorb from PMMA if given sufficient time to do so. Above 100 °C, *in situ* FTIR studies have detected the onset of a permanent chemical reaction that occurs "quickly" between the TMA and PMMA.

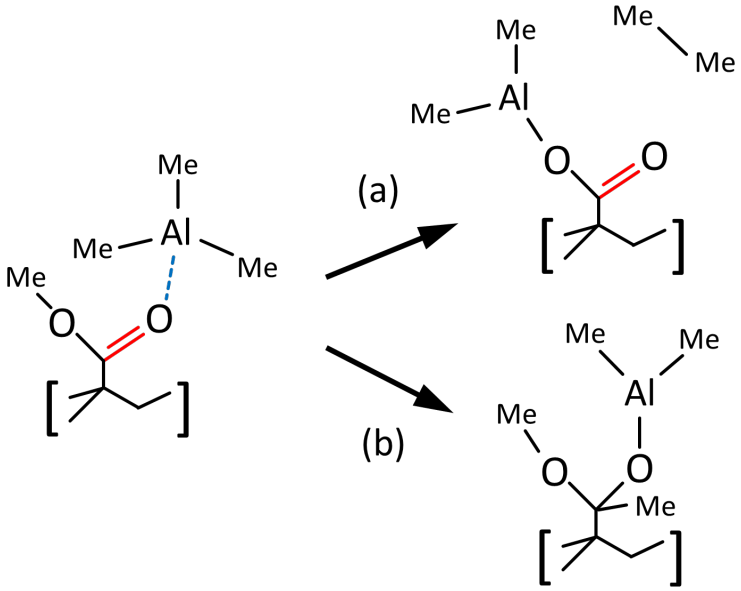

***Figure 41**: Two proposed reaction mechanisms between TMA and PMMA: (a) creation of a metal acetate group stabilized by neighboring C=O esters [18] and (b) methyl group migration to carbonyl carbon.[52]*

Using *ex situ* FTIR, we have confirmed similar reactions in our own material above this critical temperature. **Figure 42** shows FTIR spectra of pure PMMA as well as differential spectra of PMMA treated with TMA at 80 ^{o}C and 115 ^{o}C. TMA reacting with carbonyl and ester groups are indicated by the reduction of the C=O absorption at 1729 cm^{-1} and the $–O–CH_3$ stretching peak at 1145 cm^{-1}, respectively. Features also start appearing between 1500 cm^{-1} and 1700 cm^{-1}, possibly suggesting Al coordination with C=O bonds and even cross-linking.[18] Moreover, the broad peak around 3400 cm^{-1} for the longer treatments indicates a large amount of –OH groups that most likely have taken over $–CH_3$ sites of TMA precursors. An interesting observation is that at 80 ^{o}C, negligible reaction with PMMA has taken place after 20 s of infiltration, but chemical changes are noticeable with the same exposure time at 115 ^{o}C. Based on our extracted diffusion coefficients, an exposure time of 20 s should yield a TMA infiltration depth of about 40 nm into PMMA at 80 ^{o}C and about 300 nm at 115 ^{o}C. While the depth of PMMA modified by TMA is much greater at 115 ^{o}C, 40 nm worth of modified PMMA from VPI at 80 ^{o}C should be sufficient to yield noticeable peaks if reactions were present. The lack of signals suggests that reactions at 80 ^{o}C are much slower, which agree with other works stating that reaction mechanisms change around 100 ^{o}C.[18]

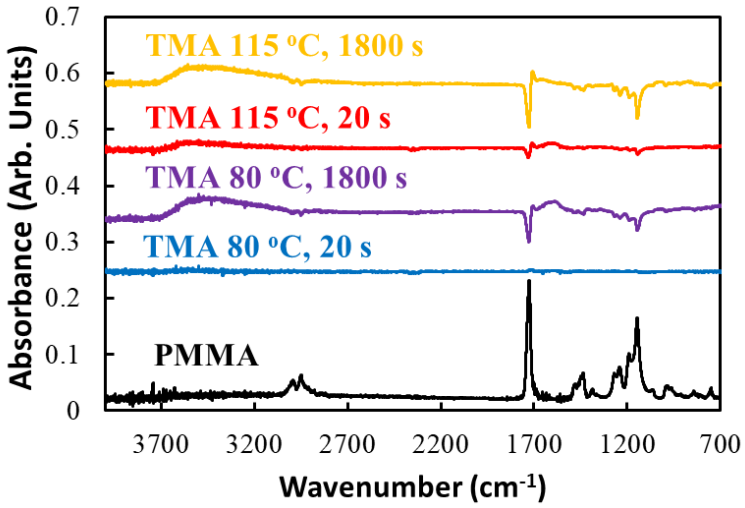

Figure 42: *Four differential FTIR spectra of PMMA films treated with TMA at different processing temperatures and times are compared to pure PMMA spectra, shown in black.*

Here, we propose the following atomic-scale physiochemical mechanisms to better understand the VPI processing in this precursor-polymer system. First, we note that the changes in both the solubility parameter and diffusion mechanism occur at 95 °C or about 10 °C below the expected glass transition temperature of our PMMA (T_g of 105 °C according to the source vendor, Sigma-Aldrich). While this difference in temperature may indicate that these changes in physiochemical mechanism are unrelated to the glassy-to-rubbery transition of PMMA, we believe the more likely explanation is that TMA is acting as a plasticizer for PMMA and effectively lowering its T_g. Thus, we ascribe the observed changes in mechanism to correspond with the glassy-to-rubbery structural change in the polymer.

4.1.6. Precursor Diffusion and Reaction

The net diffusional and reaction processes that occur over the entire VPI process can be explored using the Arrhenius plot presented in **Figure 39**. Here, we plot the natural log of diffusivity versus inverse temperature. A change in the Arrhenius slope is observed at 95 °C, again suggesting a suppression of T_g to this temperature. At low temperatures

(glassy PMMA), the Arrhenius slope (-0.8 eV) can be solely attributed to the activation barrier for TMA diffusion in PMMA, i.e., +0.8 eV (endothermic). Berens and Hopfenberg measured activation energies for diffusion of small molecules of similar size to TMA in PMMA between 30 °C and 90 °C to lie between 0.6 and 1.3 eV, comparable to our measurements.[42] At higher temperatures, the Arrhenius slope increases to -2.2 eV. We propose this increase to be a combination of the diffusional activation energy and the TMA-PMMA reaction enthalpy, as described by **Equation 21** which illustrates that a reaction sink will create an effectively "slower" diffusion rate. Assuming the activation energy for true solution diffusion (ΔH_D) is the same above and below the glass transition, the TMA-PMMA reaction energy (ΔH_{rxn}) is found to be a reasonable exothermic value of -1.4 eV. We believe the effect of transitioning from the glassy-to-rubbery state occurs in the "reaction attempt frequency". Note that the linear intercepts for the Arrhenius plot (**Figure 39**) are equal to D_o*, which is proportional to the "attempt frequency" for a given process. Above the glass transition temperature, more polymer chain motion is expected, and hence, an increase in the Arrhenius intercept (reaction attempt frequency) is observed.

An alternative interpretation of this Arrhenius plot is that the activation energy for diffusion is smaller below the glass transition temperature because of the increase in free volume. Small molecules are known to more easily diffuse through the free volume of a glassy polymer than via solution diffusion in a rubbery polymer.[85] However, because our Van't Hoff plot shows the opposite trend from standard gas sorption, it suggests that the dimerized TMA is not directly accessing the free volume of the polymer. Rather, only solution diffusion mechanisms are presumed active. Furthermore, *in situ* FTIR studies confirm the onset of a permanent chemical reaction between TMA and PMMA near 95°C.[18, 53] Thus, we believe that the onset of a diffusion-reaction mechanism above 95°C is more likely than a change in the polymer's diffusional energy barrier.

4.1.7. Extracting Energy Values from *In situ* Characterization

QCM mass change data at each processing temperature were fit to the diffusion model to extract diffusion coefficients for both in-diffusion and out-diffusion during purge without

dosing water. When water is dosed, TMA movement is largely stopped due to chemical reactions with water, and out-diffusion becomes minimal.

Figure 43a shows the natural logs of diffusivity obtained from QCM, SIMS, and ellipsometry. The activation energy of diffusion is about 1.5 eV at all processing temperatures as measured by QCM during infiltration and during purge at temperatures below 90 ^{o}C, but the value measured during purge is reduced to about 0.8 eV above 90 ^{o}C. This is in contrast to the values calculated from *ex situ* measurements: 2.2 eV and 0.8 eV at processing temperatures above and below 95 ^{o}C, respectively. Comparing the data from all three characterization methods, we also see that QCM consistently shows higher in-diffusion rates at any temperature compared to SIMS and ellipsometry. These discrepancies in both diffusivities and activation energies are largely due to the fact that SIMS and ellipsometry measurements are taken after 60 seconds of purge as well as exposure to water during the water dose and after taken out into the lab air. At processing temperatures below 90 ^{o}C, purge time is much shorter than the time to reach full infiltration, but diffusion speeds during infiltration and purge are similar. A large amount of precursor would diffuse out of the polymer during purge, resulting in a "slower" response to infiltration when measured *ex situ*. At higher processing temperatures, purge time is closer to the amount of time to reach full infiltration, but out-diffusion slows down significantly compared to in-diffusion. Again, *ex situ* measurements would yield a "slower" response but still offer accurate energy values. The difference between diffusivity during infiltration and purge at high temperatures suggests a change in the material where the polymer may be cross-linked and limit TMA movement out of the matrix. This theory is further supported by Figure **43b**, where maximum sorption is nearly the same at all temperatures but maximum desorption increases at higher processing temperatures. The result is a net decrease in sorption when measured *ex situ*, and the sorption energies above and below T_g of PMMA (~ 90 to 95 ^{o}C when exposed to TMA) as measured by ellipsometry follows closely to that of the remaining sorbed TMA when purged for a long time. Therefore, a combination of infiltration and purge mechanisms would yield the two different slopes for activation energy of diffusion as well as sorption energy when measured *ex situ*.

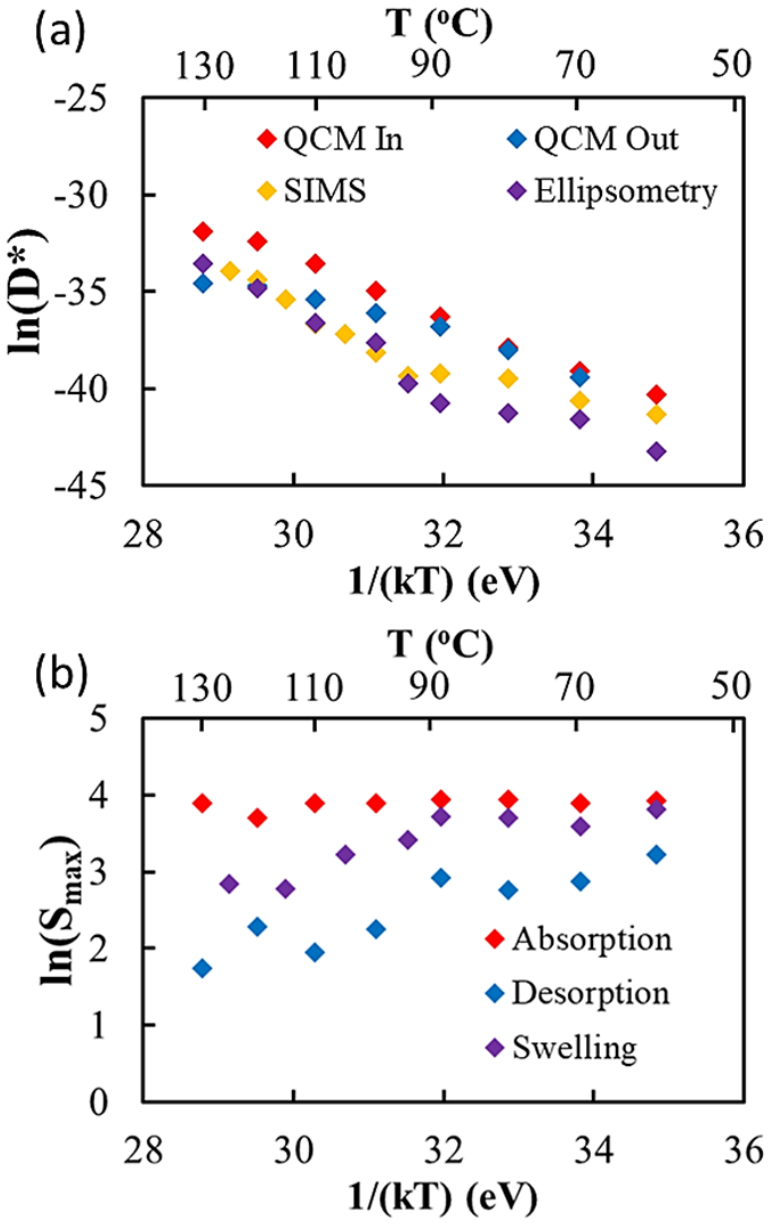

Figure 43: *(a) Natural logs of diffusion coefficients as measured by ellipsometry, SIMS, and QCM during infiltration (QCM In) and purge (QCM Out). (b) Natural logs of sorption as measured by ellipsometry (swelling), QCM during infiltration (Absorption), and QCM during purge (Desorption).*

4.2. Practical Implementation of Rational VPI Process Design

While understanding the atomistic scale mechanisms of VPI sorption, transport, and reaction will be important to developing intuitive predictions about the expected behavior of new precursor-polymer couples, understanding these mechanisms is not important if one simply wants to apply rational design principles for controlling the mass uptake and infiltration depth. To achieve this rational design, one simply needs to measure the ΔH_s and ΔH_{D^*} and the pre-exponential factors as done in this paper. These values can then be used to calculate solubility and diffusivity at any temperature and substituted into the solution for Fick's 2nd Law for any geometry.

For infiltration depths that are far from the substrate boundary such as when treating bulk polymers or thick polymer films, using the complementary error function with the semi-infinite diffusion model avoids the more complicated diffusion equations that take boundary conditions at the impermeable substrate into consideration. Using diffusion coefficients extracted from SIMS and ellipsometry data at different temperatures, we create a graph that shows the time-temperature-position dependence of infiltration for the PMMA-TMA system (**Figure 44**).

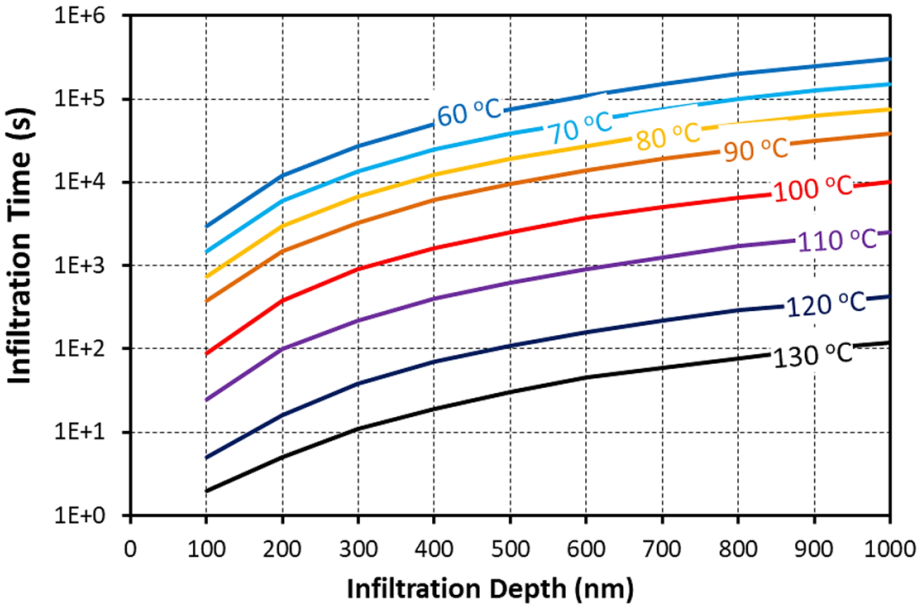

***Figure 44**: Time-temperature-position dependence of TMA infiltrating PMMA.*

The extent of infiltration depth is arbitrarily set as 20% of maximum concentration of the penetrant. If we want to infiltrate 500 nm into a PMMA sample at 130 ^{o}C, then we can refer to **Figure 44** and see that an infiltration time of 20 seconds would be required. For the same infiltration depth at 60 ^{o}C would require an infiltration time of about 80,000 s, or 22 hours. As one can see from the significant difference in required infiltration time, knowing the kinetics is very important when designing a VPI process.

To demonstrate this level of rational design, we have calculated the process time required to infiltrate a 1.4 micron PMMA film on an impermeable substrate to a depth of 400 nm. For a processing temperature of 100 ^{o}C, the infiltration time would be about 1100 s, or about 18 minutes. Alternatively, we can also calculate the time using the average diffusion coefficient calculated from SIMS and ellipsometry. At 100 ^{o}C, the effective diffusion coefficient is about 3.5 x 10^{-13} cm^2/s, and t = 750 s. Although the required infiltration times found from **Figure 44** and from directly using measured diffusion coefficients can vary, they are very similar when taking into account the orders of magnitude difference in diffusion rates at different temperatures. From these calculations, TMA exposure time of about 10 minutes is required for an infiltration depth about a 1/3 of the way into the PMMA film. In **Figure 45**, we show a cross-sectional SEM micrograph of this VPI infiltrated film. The yellow line at the right of **Figure 45** is the EDX line scan of the aluminum signal across the film. The infiltrated region is slightly brighter due to higher atomic number contract, but this layer is essentially homogeneous at the atomic scale (no indication of aggregated Al_2O_3 secondary phases). The EDX line scan shows aluminum concentrated in the top third of the film cross section, or about 400 nm, which is close to our prediction, demonstrating the ability to use these fundamental parameters to help design future VPI processes.

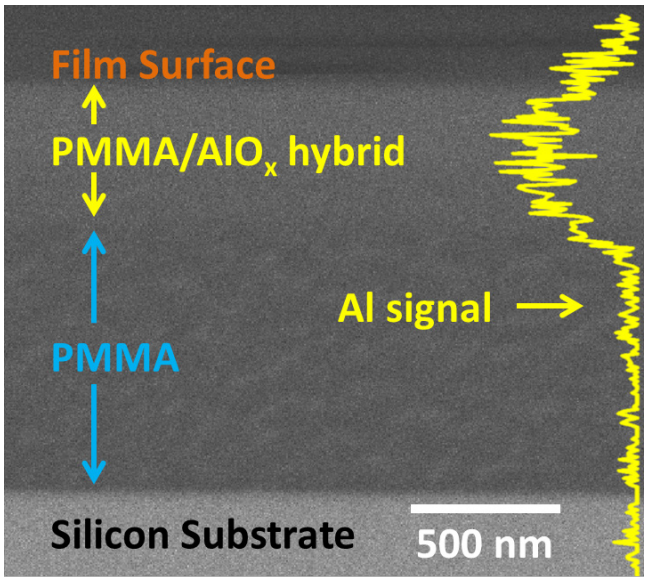

***Figure 45**: SEM image with EDX line scan on a 1.4 micron PMMA film infiltrated with TMA at 100 ^{o}C for 10 minutes.*

5. PROPERTIES OF HYBRID MATERIALS

5.1. Chemical Stability of VPI Treated PMMA

In this section, we look at three potential impacts on the chemical stability of the PMMA films: 1) minimum precursor infiltration depth that would shield pure, untreated PMMA underneath, 2) any dependencies on VPI processing temperature, and 3) behaviors of fully treated PMMA in different solvent types.

5.1.1. Chemical Stability of PMMA-AlO_x Hybrid Films

Building upon this basic understanding of how TMA VPI of PMMA can be used to alter the original material's solubility, we sought to better understand how variations in processing conditions – which we and others have previously shown are known to alter the inorganic loading fraction, chemical bonding between organic and inorganic phases, and potentially other structural features – alter the hybrid material's chemical solubility in a variety of solvents. **Figure 46** plots solvent stability for fully infiltrated PMMA-AlO_x hybrid films created at varying VPI process temperatures and immersed in toluene. Besides some modest measurement noise in a few samples, all hybrid films, regardless of VPI process temperature, remain stable in toluene for over a month with no indication of degradation. This result is somewhat surprising because prior observations have indicated (1) chemical reactions between TMA and PMMA occur much more slowly, if at all, below process temperatures of ~100 °C,[18, 52] and (2) inorganic loading fraction decreases significantly above process temperatures of 100 °C.[86] In fact, at a VPI process temperature of 130 °C, PMMA-AlO_x films likely have no more than 15 % volume fraction of inorganic based upon film swelling. Thus, it is somewhat surprising, that even at these low loading fractions, the hybrids remain chemically insoluble.

To further investigate whether these potential differences in PMMA-AlO_x structure may affect chemical stability, we challenged these materials against a number of different

solvents: toluene, tetrahydrofuran (THF), acetone, isopropanol (IPA), cyclohexanone, chloroform, ethanol, and water. For these experiments, three process temperatures were chosen: 70 °C, 100 °C, and 130 °C. Results are summarized in **Figure 47**. For untreated PMMA, organic solvents quickly dissolved the films entirely, and the two alcohols degraded the films slightly over several days, leaving water as the only solvent that did not affect the polymer. For treated PMMA, immediately evident is that films processed at 70 °C and 100 °C show greater interaction with various solvents than films processed at 130 °C. At 130 °C, little interaction is seen with any solvent except isopropanol. Also important to note is that none of the treated films fully dissolved or delaminated within the test period of 1 month in any solvent.

Further studies will be necessary to fully understand all of the differences in dissolution and swelling behavior observed in films processed at 70 °C and 100 °C and challenged in different solvents. However, a few possible mechanisms are worth conjecturing. First, it is interesting that the polar solvents water and IPA appear to partially dissolve the PMMA-AlO_x processed at 70 °C, but not the polar solvent ethanol. It is thought that these polar solvents are in some way attacking the inorganic component, possibly hydrolyzing the Al-O-Al bonds back to hydroxylated species that break the cross-links or fully dissolve. Second, the two solvents with the closest Hildebrand solubility parameters to PMMA, THF and chloroform, exhibit moderate dissolution of PMMA-AlO_x at 70 °C process temperature and hybrid film swelling at 100 °C process temperature. This suggests that at the lower process temperature, the potential lack of chemical cross-linking may allow for dissolution of the organic component when exposed to an extremely good solvent, while for higher process temperatures when chemical cross-links are formed, the material may swell in these good solvents as expected for a gel. At the highest process temperature, 130 °C, this swelling is not observed due to greater cross-linking that stiffens the elastic modulus of the gel. More detailed studies of these dissolution and swelling behaviors could likely lead to a better understanding of the complex physiochemical structure of the hybrid PMMA-AlO_x materials.

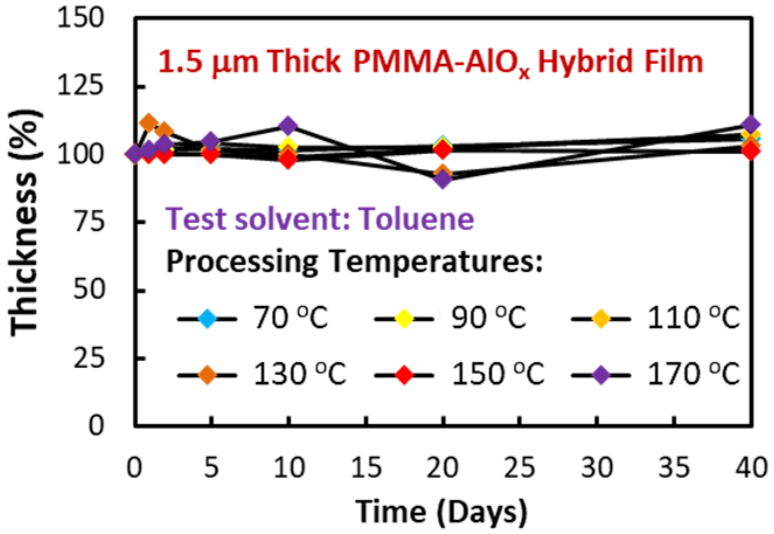

Figure 46: *Toluene solubility test of PMMA films fully infiltrated with TMA VPI at processing temperatures ranging from 70 °C to 170 °C. 100% thickness means no change from initial film thickness prior to solvent exposure.*

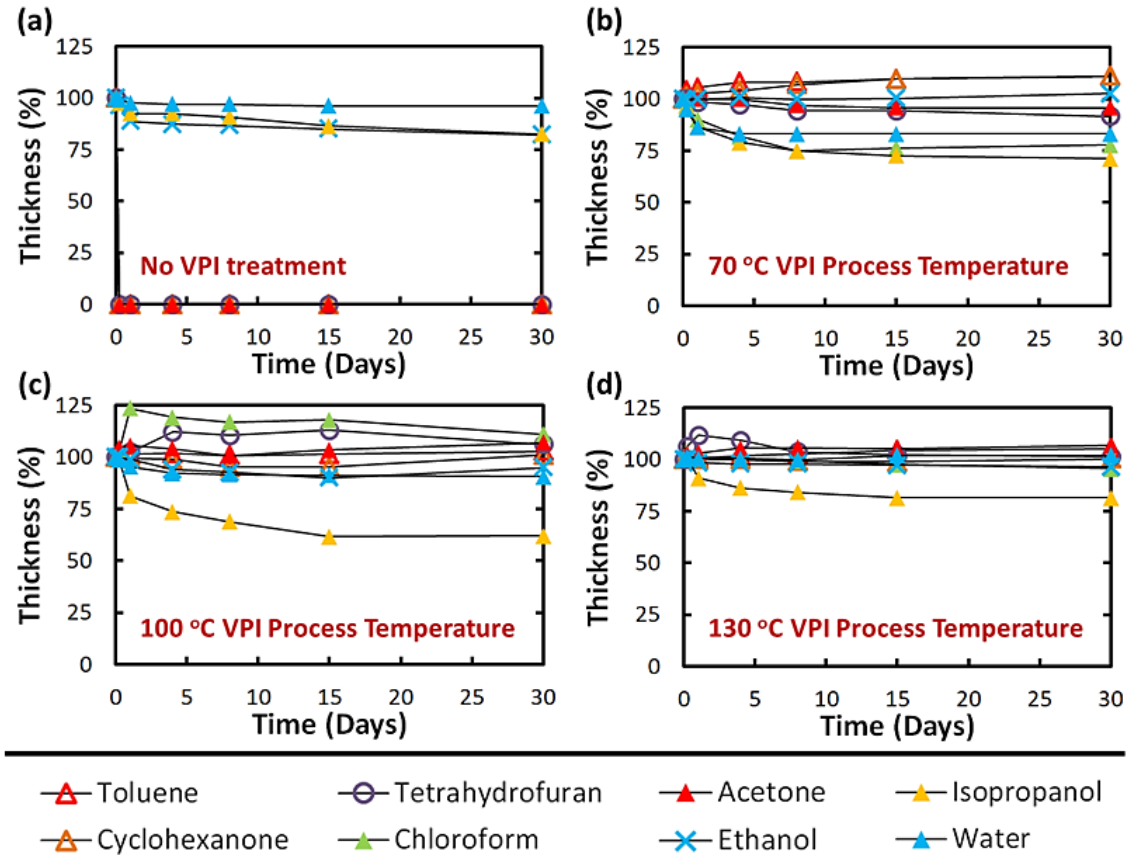

Figure 47: *Long term chemical stability of a) untreated PMMA and PMMA treated with TMA VPI at b) 70 ^{o}C, c) 100 ^{o}C, and d) 130 ^{o}C in the following solvents: toluene, cyclohexanone, tetrahydrofuran, chloroform, acetone, ethanol, isopropanol, and water.*

Processing temperature appears to not affect the ability of the treated film to resist toluene and most other organic solvents, but some degradation is more noticeable for PMMA films treated at lower processing temperatures when immersed in solvents such as chloroform, isopropanol, and water (**Figure 47**). The fact that the films are no longer soluble in organic solvents but show some weakness to polar solvents suggests that the new hybrid material is partially held together by hydrogen bonds in addition to van der Waal forces in non-treated PMMA. The hydrogen bonds should originate from hydroxyl groups attached to aluminum atoms that have covalently bonded with PMMA chains during TMA infiltration.

Crosslinking through TMA reactions could occur through the three ligands on each TMA molecule reacting and bonding to different polymer chains. Crosslinking can also occur through condensation reactions where two hydroxyls from two different PMMA-TMA units react together to form covalent oxygen bonds with water as a byproduct (**Figure 48**). However, the type of crosslinking in the PMMA-TMA hybrid material is at this point still unclear.

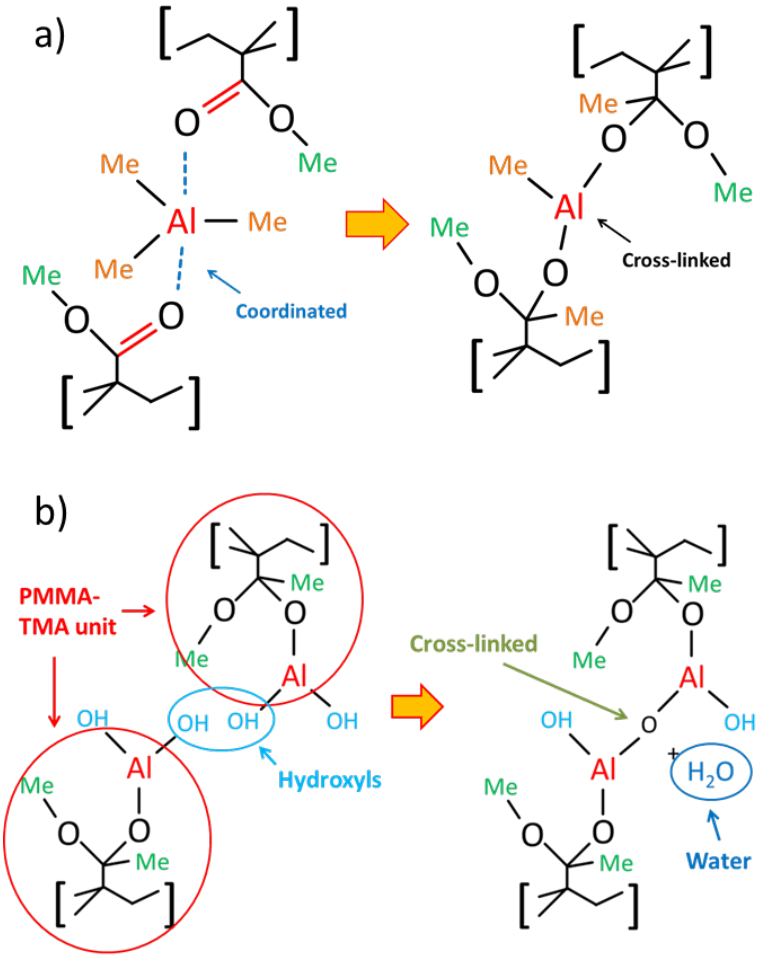

Figure 48: *Possible cross-linking mechanisms through (a) single TMA molecule reacting and attaching to carbonyl groups from two or more PMMA chains and (b) condensation reaction between hydroxyl groups in PMMA-TMA complexes. The placement of TMA with the PMMA unit is based on a plausible structure presented by Biswas et al.*[52]

Next, we sought to understand whether a subsurface infiltrated hybrid layer could serve to protect an underlying PMMA polymer from dissolution. We infiltrated 1.5 μm thick PMMA films with TMA at 100 ^{o}C to depths of up to 1 micron in approximately 100 nm increments and then immersed the films in toluene. Infiltration depth, calculated based on our prior report on the infiltration kinetics for this VPI process [ref us], is defined as the depth where the concentration of the precursor is 20% of the maximum precursor concentration found at the surface of the film (**Figure 49a**). **Figure 49b** presents the

results from toluene dissolution testing for films with varying hybrid infiltration depths. In this figure, X's mark failure points. In some cases, failure resulted from total dissolution while in others a film failed due to significant film structural degradation resulting in an inability to collect an accurate ellipsometry measurement. Films with between 100 nm and 400 nm infiltration depth show some resistance to toluene but eventually fail after several hours of immersion in toluene. As infiltration depth increased in this range (300 and 400 nm), the films dissolved less but started exhibiting rough surface features. Films with infiltration depths of over 500 nm are determined to be insoluble and stable for at least 40 days with no significant thickness change or visual damage.

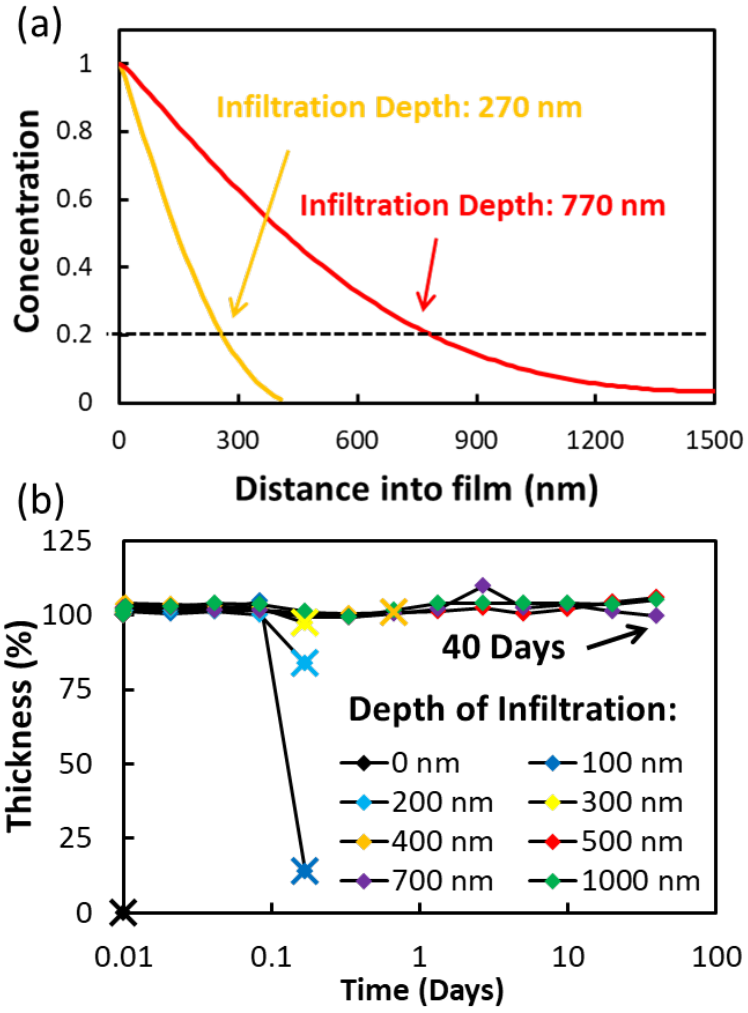

Figure 49: *(a) Example depth profiles with infiltration depth defined as 20% of maximum concentration and (b) PMMA films with varying TMA infiltration depths immersed in toluene at room temperature.*

Using confocal microscopy, we studied how PMMA films with shallow TMA infiltration depths fail. **Figure 50a-e** shows optical images depicting the dissolution process of a 1.4 μm PMMA film infiltrated with TMA to about 200 nm at a processing temperature of 100 ^{o}C. Rather than displaying a gradual thinning of the entire film, the progression shows a clear nucleation and growth pattern of bubbles (**Figures 50b** and **50c**) that ultimately results in film buckling and delamination (**Figures 50d** and **50e**). The bubbles in the artificially colored height image (**Figure 50f**) and 3D rendering of the height image (**Figure 50g**) show up as noticeably lower in height compared to the surrounding film as indicated by the blue and green shades inside the bubble areas. The yellow to red areas adjacent to the bubbles indicate thicker film. A possible explanation for the difference in height is that the bubbles are the result of toluene seeping through small holes in the hybrid upper layer and dissolving the pure PMMA layer underneath. When the film is dried, toluene along with the dissolved PMMA is removed, leaving behind the hybrid film that collapses over the bubble regions (**Figure 50h**). Red slivers inside the bubble areas indicate much higher topography and appear to be raised folds. The folds left in the collapsed bubbles may be caused by the hybrid film swelling from the original TMA infiltration process. Since the film cannot expand laterally due to strong steric constraints by the PMMA material underneath, a partially infiltrated film appears smooth prior to immersing in solvents. Once the film is placed in solvents like toluene, the PMMA material underneath dissolves away and the film is free to expand laterally and buckle. Given long enough immersion times, the bubbles will increase in size to combine into a loose film on top of the silicon.

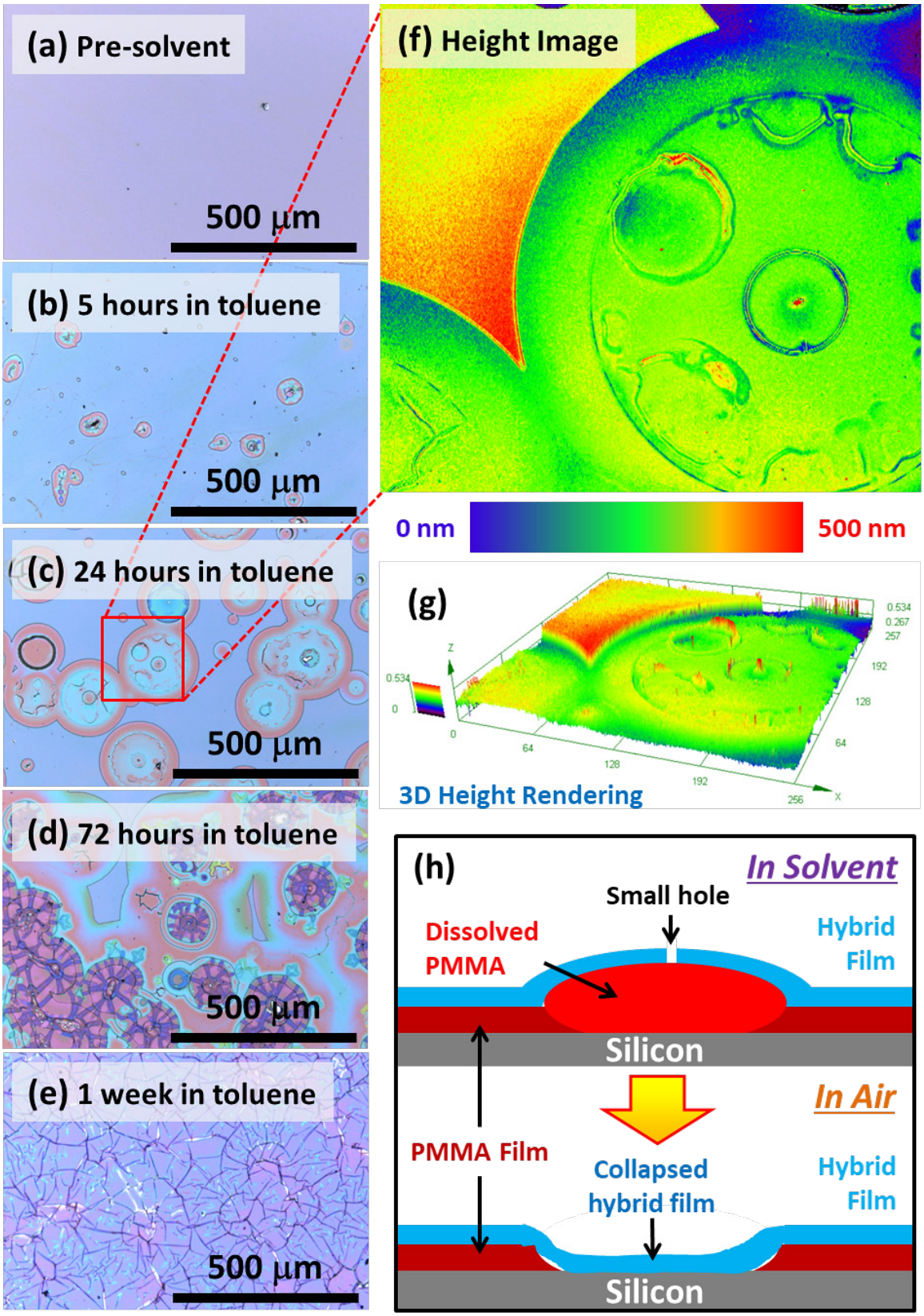
(a) Pre-solvent
500 µm
(b) 5 hours in toluene
500 µm
(c) 24 hours in toluene
500 µm
(d) 72 hours in toluene
500 µm
(e) 1 week in toluene
500 µm
(f) Height Image
0 nm
500 nm
(g)
3D Height Rendering
(h)
In Solvent
Small hole
Dissolved PMMA
Hybrid Film
Silicon
In Air
PMMA Film
Collapsed hybrid film
Hybrid Film
Silicon

Figure 50: *Dissolution in room temperature toluene of a 1.4 μm PMMA film infiltrated with TMA to a depth of 200 nm at a processing temperature of 100 °C. The pictures taken using real-color confocal microscopy describe the following: (a) original treated film, (b) "nucleation" bubbles at 5 hours, (c) growth of bubbles at 24 hours, (d) encroachment of bubbles leading to film buckling at 72 hours, and (e) severe buckling of the entire film at 1 week. A close-up of bubbles in (c) is visualized through a height image (f) and the 3D rendering of the height image (g) as measured using confocal laser scans. A color bar translates the colors in (f) and (g) to height in nanometers. (h) Schematic shows the cross sectional view of a bubble inside toluene solution and in air. The light blue layer represents the hybrid material, and the dark red layer represents pure PMMA. The bright red bubble represents PMMA dissolved in toluene solution.*

5.1.2. Chemical Stability Application on Macro Samples

Infiltrating a preformed PMMA object with TMA can create a hybrid material outer layer that protects the interior PMMA from solvent attacks. This processing technique works very well for both micro and macro objects. **Figure 51**shows how TMA VPI can create an effective solvent barrier for large objects. The two PMMA panels representing the school mascots of UGA and Georgia Tech were both placed in toluene heated to 60 °C, but because the Georgia Tech mascot panel was treated with TMA VPI, it showed minimal solvent damage. The UGA mascot panel was not treated and suffered severe solvent damage to the point that surface engravings and patterns were lost. Interestingly, TMA VPI treatment causes the original clear and smooth PMMA surface to become textured and milky in appearance. We attribute this to the hybrid material swelling due to TMA infiltration, and the swelling creates enough stress to buckle the surface and creates light diffractions, thus resulting in a milky appearance (**Figure 52**). We do not see this buckling behavior in our treated PMMA films due to fewer degrees of freedom in a film compared to bulk, but as discussed in the dissolution of partially infiltrated films, the hybrid film will buckle when the PMMA layer underneath is removed.

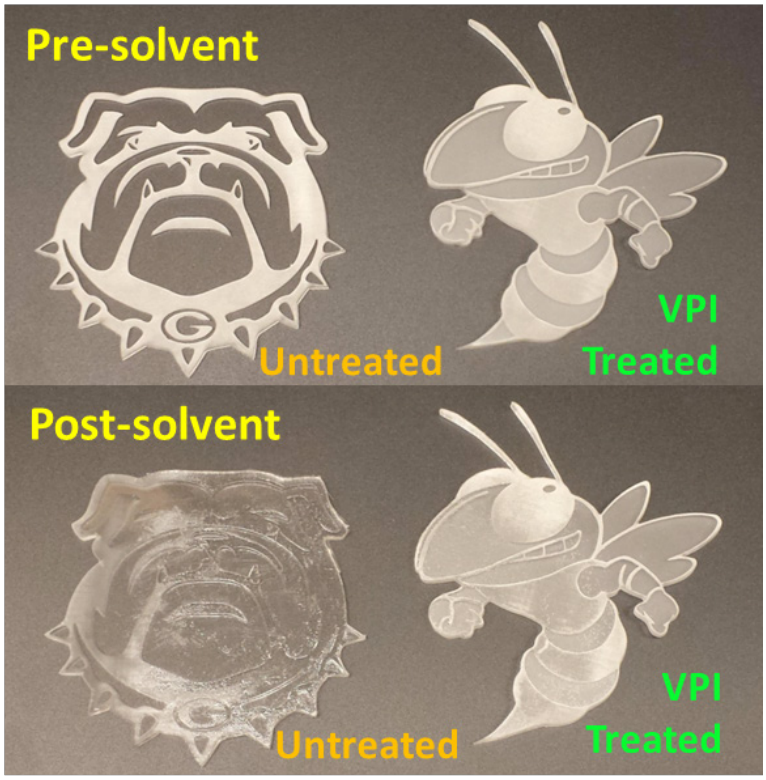

Figure 51: *Comparison of two PMMA objects, one with pure PMMA on the surface and the other with a protective outer layer made from TMA VPI, after submersion in toluene heated at 60 ^{o}C for 10 minutes.*

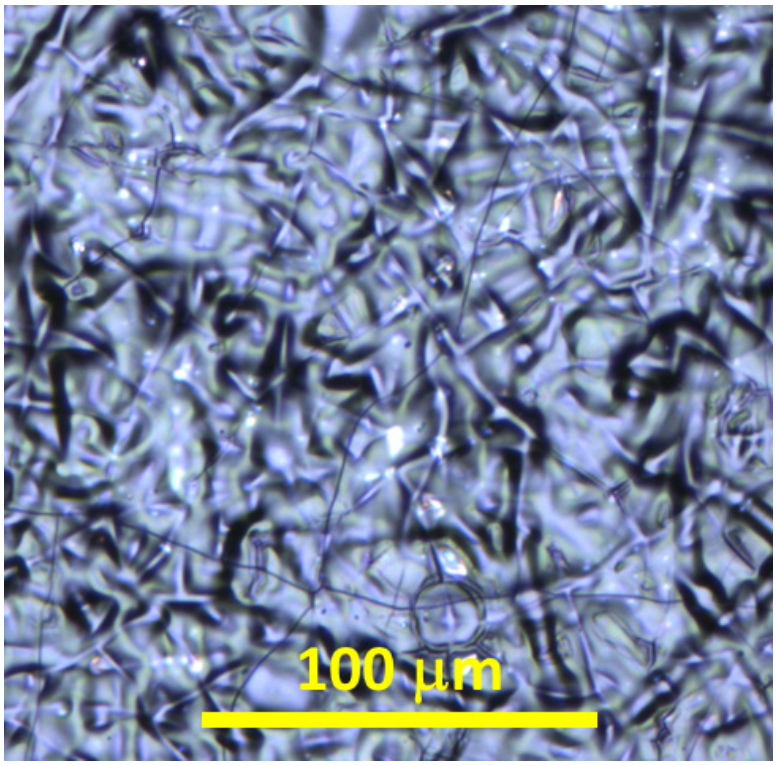

Figure 52: *Optical image of the TMA VPI treated PMMA panel depicting the Georgia Tech mascot.*

5.2. Moisture Absorption of PMMA-AlO_x Hybrid Films

After full TMA VPI on PMMA at processing temperatures ranging from 70 ^{o}C to 130 ^{o}C, the treated films can absorb a noticeable amount of water from the air, whereas untreated films do not. This is because treated PMMA contains hydroxyl groups from TMA ligands reacting with water (**Figure 53**), and the hydroxyl groups have high water affinity. The difference in behavior between a treated and untreated PMMA film can be observed when heating up the films to 160 ^{o}C and measuring their chemical changes with FTIR (**Figure 54**) and their thicknesses as a function of temperature using ellipsometry.

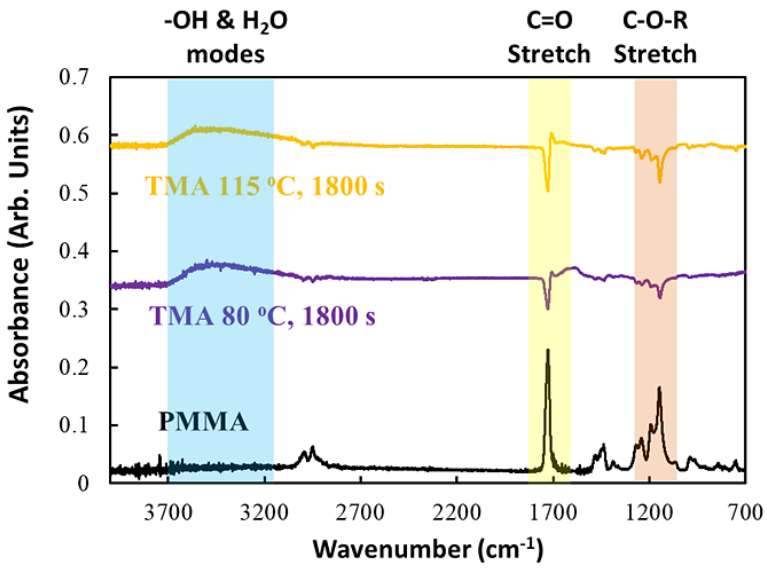

Figure 53: *FTIR spectra of untreated 1.4 μm thick PMMA film (black). FTIR difference spectra of 1.4 μm thick PMMA films treated with TMA VPI at 80 °C (purple) and 115 °C (orange). Changes to C=O stretch, C-O-R stretch, and -OH modes are highlighted in yellow, orange, and blue, respectively.*

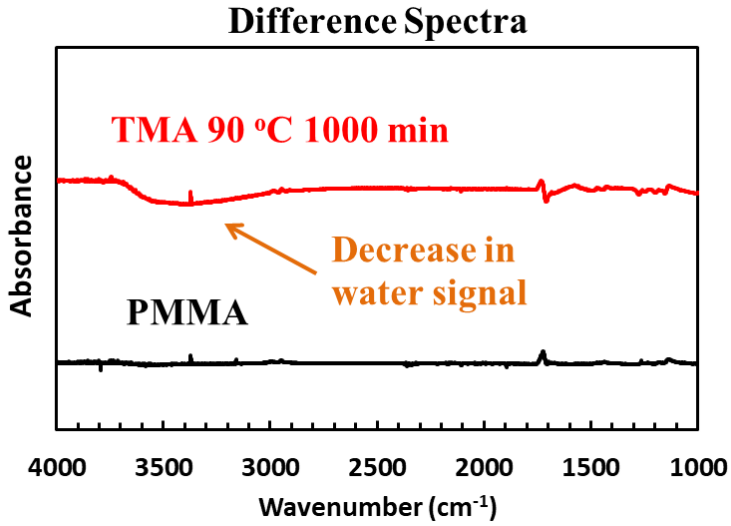

Figure 54: *FTIR difference spectra of untreated (black) and treated (red) 1.4 μm thick PMMA films before and after heating at 160 °C for 10 minutes.*

Figure 55 shows percentage thickness change of a pure, untreated PMMA film when slowly heated from 25 °C to 160 °C. Two distinct slopes are noticeable above and below

T_g = 105 °C. Below T_g, the polymer chains do not move around as easily in the glassy phase, resulting in a lower CTE of about 2.6 x 10^{-4} K^{-1}. Above T_g, CTE is higher at about 6.2 x 10^{-4} K^{-1}. These two CTE values agree very well with literature values of 1.7 x 10^{-4} K^{-1} and 6.7 x 10^{-4} K^{-1} below and above T_g, respectively, for PMMA films on silicon.[87]

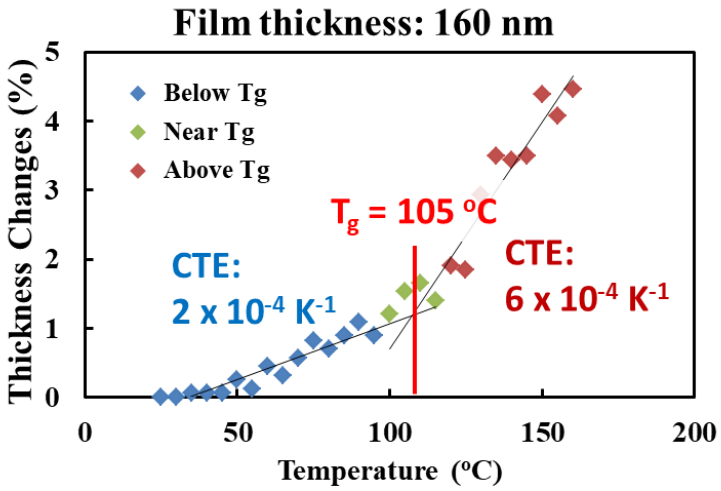

Figure 55: *Thickness changes of pure, untreated 160 nm PMMA film as a function of temperature. Coefficients of thermal expansion is calculated and labeled for the regions above and below* T_g.

Figure 56 shows percentage thickness changes of 160 nm PMMA films fully treated with TMA at 70, 100, and 130 °C. Instead of increasing in thickness with increasing temperature, the films decreased in thickness when heated. The shrinking behavior of the infiltrated PMMA is likely due to desorption of water from the films at higher temperatures. When cooled, the films do not quickly expand back to its original thickness, and there are also no clear signs of a glass transition temperature. This hysteresis can be explained by the porosity of the treated film. When the treated film is saturated with absorbed water, the polymer chains are pushed further apart. Heating the films allow the water molecules to quickly leave the polymer matrix, which then collapses slightly to fill up the voids left by the escaped water. Film thickness does increase back to its original, pre-heated value over a couple of hours, but the rate of water absorption is relatively slow

because the “collapsed” matrix needs time to occasionally open up a void for a water molecule to fill back in.

Processing temperature also affects the amount of water uptake. Higher processing temperature appears to have a smaller impact on water uptake since film contraction is less, and the material almost exhibits a glass transition behavior when cooling down. A larger amount of TMA appears to be locked inside the PMMA at lower temperatures.

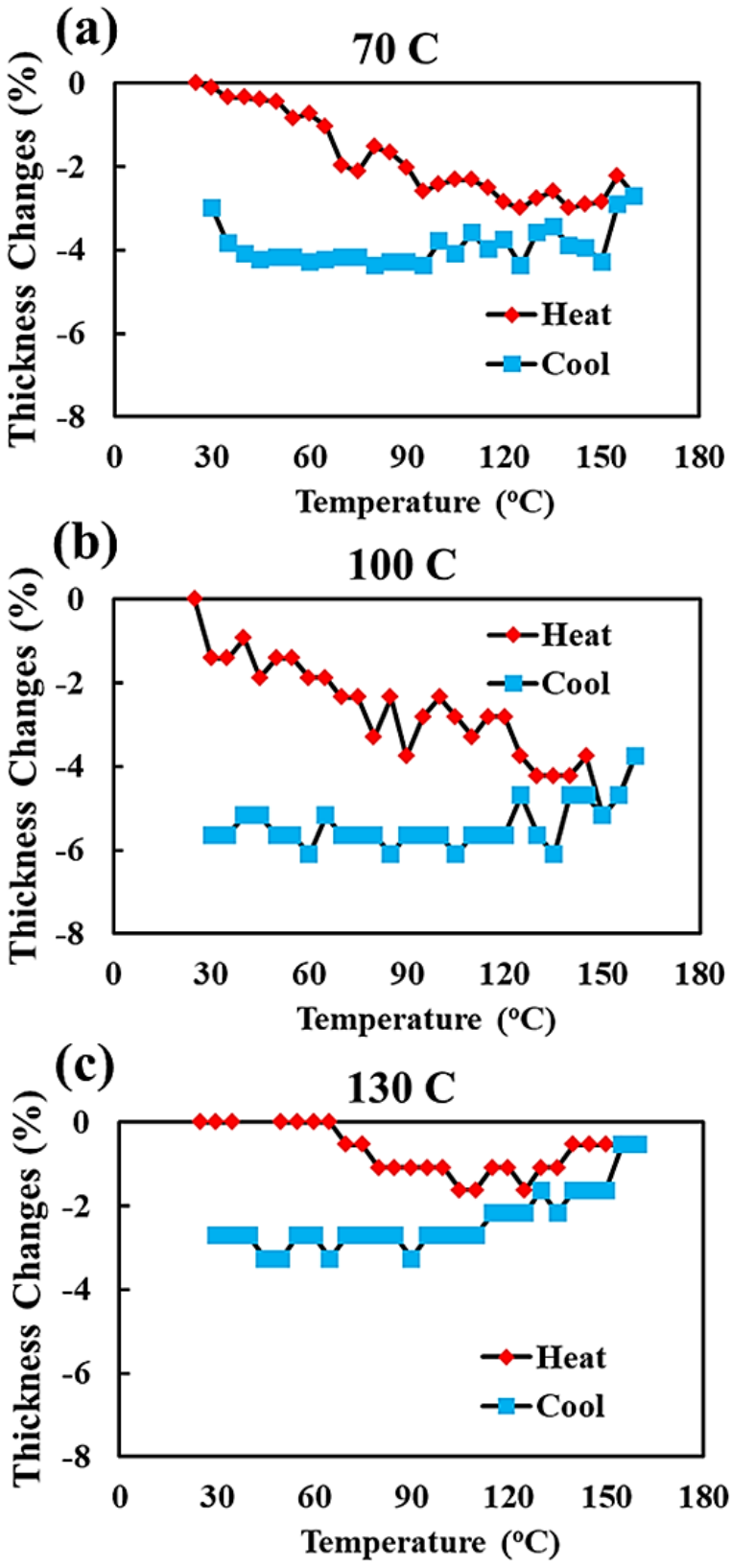
(a)
70 C
Thickness Changes (%)
0
-2
-4
-6
-8
0
30
60
90
120
150
180
Temperature (°C)
Heat
Cool
(b)
100 C
Thickness Changes (%)
0
-2
-4
-6
-8
0
30
60
90
120
150
180
Temperature (°C)
Heat
Cool
(c)
130 C
Thickness Changes (%)
0
-2
-4
-6
-8
0
30
60
90
120
150
180
Temperature (°C)
Heat
Cool

Figure 56: *Temperature dependence of PMMA film fully treated with TMA VPI at 70, 100, and 130 °C. Thickness readings are labeled in red during heating and blue during cooling.*

5.3. VPI Processing on Selectively Reactive Polymers

After TMA infiltration, films of PS-r-PHEA with higher percentages of hydroxyl groups swelled up to 10% of their original thicknesses (**Figure 57**), indicating that TMA infiltrates into the polymer rather than reacting on the surface to form an impenetrable layer. In addition, swelling does not decrease significantly when the films are purged for a longer time after infiltration, meaning that reactions between TMA and hydroxyl groups are irreversible, and almost all TMA molecules that infiltrate into the PS-r-PHEA polymer will chemically react. FTIR difference spectra of PS-r-PHEA 5% treated with TMA VPI at 70 °C and 130 °C are shown in **Figure 58**. At both temperatures, a broad peak around 3400 cm^{-1} indicates the presence of absorbed water due to the presence of infiltrated TMA that have reacted with hydroxyl groups in PS-r-PHEA chains.

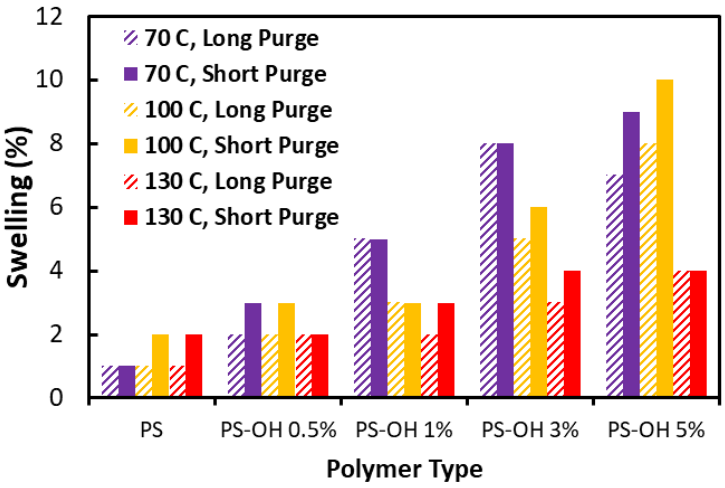

Figure 57: *Thickness changes of PS-r-PHEA films from TMA VPI at 70, 100, and 130 °C with purge times of either 1 minute or 1000 minutes.*

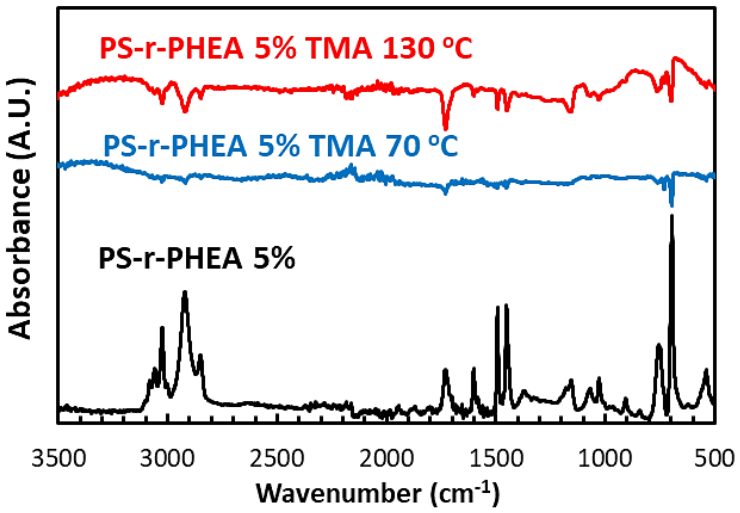

Figure 58: *FTIR spectrum of PS-r-PHEA 5% (black) and FTIR difference spectra of PS-r-PHEA 5% treated with TMA VPI at 70 °C (blue) and at 130 °C (red).*

Because PS-r-PHEA polymers with higher hydroxyl concentrations hold more sites for TMA reactions, they are more easily transformed chemically and structurally during VPI. When immersed in toluene, PS-r-PHEA polymers with hydroxyl percentages lower than 3% dissolve fully within 10 minutes, whereas polymers with hydroxyl percentages of 3% and higher only gradually dissolve over several weeks (**Figure 59**). The dramatic difference suggests a structural change around the 3% level, where the concentration of hydroxyl groups is high enough that crosslinking among polymer chains begins. Crosslinking must be a factor since each TMA molecule that reacts with and binds onto a hydroxyl site only increases the net hydroxyl count at that site by one (the original OH group is transformed to an Al-O bond). That means a PS-r-PHEA 5% should have the same solubility in toluene as a PS-r-PHEA 2.5% fully treated with TMA VPI, but that is clearly not the case since untreated PS-r-PHEA 5% is still very much soluble in toluene, whereas PS-r-PHEA 2.5% fully treated with TMA VPI should show lower solubility similar to that of a fully treated PS-r-PHEA 3%. Therefore, the decrease in solubility of the treated polymers is not primarily caused by an increase in hydroxyl groups from reactions with single TMA molecules, but individual TMA molecules binding together two or three polymer chains through crosslinking. While PS-r-PHEA with 3% or 5%

hydroxyl groups have lower solubility in toluene, the films still gradually decrease in thickness. A possible explanation for this phenomenon is that only some polymer chains have crosslinked, and free polymer chains will slowly make their way out of a loosely crosslinked matrix. When plotted in log time, the film thicknesses of the PS-r-PHEA 3% and 5% films decrease linearly, thus suggesting an exponential decay in the number of free chains inside the treated films.

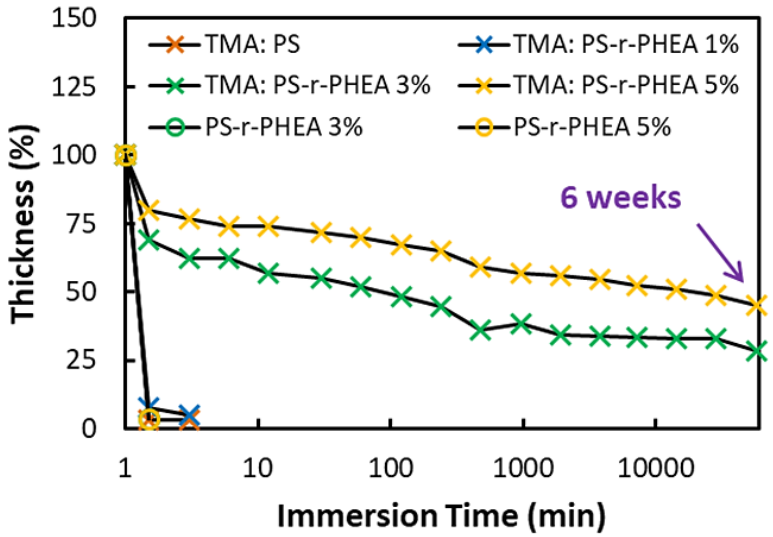

Figure 59: *Thickness changes of treated and untreated PS-r-PHEA films of hydroxyl concentrations of 0% (pure polystyrene), 3%, and 5%. TMA VPI processing temperature was 100 °C for the fully treated films.*

Heating up the treated and untreated PS-r-PHEA films to 160 °C from room temperature also shows differences in the respective materials' coefficients of thermal expansion (CTE) (**Figure 60**). For both treated and untreated PS-r-PHEA 1% films, we measured a CTE of 2.9 x 10^{-4} K^{-1} below the glass transition of polystyrene and a CTE of 6.3 x 10^{-4} K^{-1} above T_g. These values are similar to literature values measured for polystyrene, where CTE above and below T_g are about 5 x 10^{-4} K^{-1} and 2 x 10^{-4} K^{-1}, respectively.[88] TMA VPI did not significantly change the thermal expansion properties of PS-r-PHEA 1% films. However, for PS-r-PHEA 5%, CTE values were very different between treated and untreated films. We measured CTEs of 2.7 x 10^{-4} below T_g and 8.3 x 10^{-4} above T_g for

untreated PS-r-PHEA 5%. For treated films, CTE values were lower: 0.7 x 10^{-4} below T_g and 3.3 x 10^{-4} above T_g. We attribute this difference to crosslinking of treated PS-r-PHEA 5% since crosslinked polymers cannot expand easily with increasing temperature (PS-r-PHEA 3% also exhibited a decrease in CTE when treated with TMA VPI). Because the hydroxyl concentration in PS-r-PHEA 1% is not enough to form a noticeable crosslinked network, solvent resistance and thermal expansion properties did not change between treated and untreated films. PS-r-PHEA 3% and PS-r-PHEA 5% had enough hydroxyl concentrations to significantly increase solvent resistance and decrease CTEs.

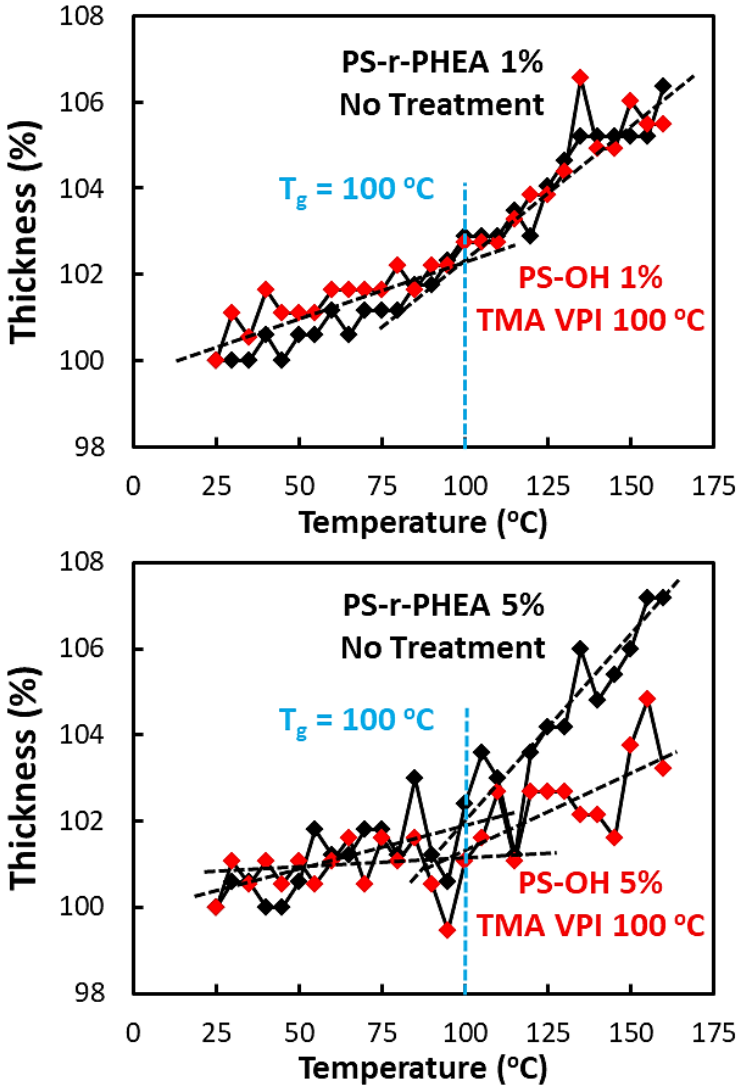

Figure 60: *Thickness changes for treated and untreated PS-r-PHEA 1% and 5% films when heated from 25 ^{o}C to 160 ^{o}C in 5 degree increments. The starting thicknesses of the treated and untreated PS-r-PHEA 1% films were 183 nm and 173 nm, respectively, and 186 nm and 164 nm, respectively, for PS-r-PHEA 5% films.*

6. SUMMARY OF IMPACT & FUTURE WORK

The TMA-PMMA system has interested many research groups since PMMA can react with TMA to create new hybrid materials, but past research has mostly focused on new properties and applications with a few works studying chemical reaction pathways. VPI processing conditions has largely been largely guesswork, and processes tend to follow the multi-cycle nature of ALD due to a lack of understanding about VPI. Better control of the VPI process requires a better understanding of the infiltration rate and amount at various processing conditions. This thesis provides this understanding by taking an in-depth look at the kinetics and thermodynamics of vapor phase infiltration for the TMA-PMMA system. By calculating diffusion coefficients across a range of temperatures, we extract out energy values for sorption, activation energy of diffusion, and reaction enthalpy. We observe a change in diffusion behavior above the glass transition of PMMA, where reactions may be crosslinking the polymer chains. Chemical stability tests of PMMA/AlO_x hybrid films also show increased solvent resistance from higher VPI processing temperatures. In addition, we observe an increase in total TMA sorption at lower processing temperatures, which is contrary to typical gas solubility behaviors. The findings in this thesis not only provide a framework on which to build continued research on the kinetics and thermodynamics of VPI, but they will also help guide future work on applications of VPI processes and hybrid materials.

Additional research on the kinetics of the TMA-PMMA system as well as systems with other polymers and precursors is necessary to better understand the diffusion and reaction mechanisms. Here, we outline several topics that should be studied further.

TMA Reactions with PMMA: Although reaction mechanisms have been proposed by other groups, we still do not yet have a complete understanding of the chemical reaction pathways at different processing conditions. We are fairly confident that TMA crosslinks PMMA at high processing temperatures since the resulting material is very resistant to both polar and organic solvents. However, more chemistry-oriented methods, whether through computational modeling or reaction studies of simpler systems, can help verify such crosslinks.

Precursor Size and Chemistry: TMA is well known to react with PMMA and create hybrid materials via infiltration. Exploring which other precursors may also react with PMMA is the next step toward creating diverse hybrid materials with unique properties. One variable of interest is precursor size. Larger precursors are expected to diffuse more slowly than smaller precursors, but their ligands may also react with polymer functional groups differently. A set of experiments to test size effects would be to compare infiltration kinetics and thermodynamics of TMA with triethylaluminum, which contains ethyl groups as ligands as opposed to the smaller methyl groups in TMA. Precursors with different elements and ligand chemistries such as titanium tetrachloride and diethyl zinc can also be of interest due to the higher refractive indices of titanium oxide and zinc oxide compared to aluminum oxide. Although hybrid materials may not have metal oxide domains, the different metal-oxygen bonds in the hybrid materials can potentially give rise to different properties of the material.

Reactive and Inert Polymers: Polymers such as polycarbonate and polyamide have functional groups that can react with metalorganic precursors such as TMA. The processing theory developed in this thesis can be applied to these polymer systems to extract diffusion coefficients and energy values for thermodynamics and kinetics. Future work can also focus on how precursors can optimally interact with inert polymers, which do not have particular functional groups, to create hybrid or nanocomposite materials. Finding the right processing conditions with potential co-reactant pairs could theoretically create fairly uniform inorganic domains inside inert polymers. A more complete understanding of how precursors interact with both reactive and inert polymers can allow more kinds of hybrid materials to be synthesized for wider ranges of applications.

***In Situ* VPI Processing Analysis:** The *in situ* VPI process characterization is a good start at understanding the kinetics and thermodynamics of VPI during the actual process. However, the QCM system used in this project only tells one part of the picture: mass changes to the film. The system cannot differentiate the types and amounts of substances infiltrating into the film, and therefore we do not know how much nitrogen and other contaminants are diffusing into the films along with TMA precursors. Insight from

desorption is also limited since both unreacted TMA and reaction byproducts could be diffusing out together and at different rates. A residual gas analyzer (RGA) could potentially provide chemical data that can help differentiate the species diffusing into and out of the polymer films during a VPI process. *In situ* reflectometry can also give some information on film thickness changes during infiltration and purge. Future experiments could use all three measurement tools to see if decreases in mass measured by the QCM during purge after infiltration correspond to chemical byproduct gases as measured by the RGA and to a film thickness decrease as measured by the reflectometer.

Additionally, QCM crystals whose frequencies are not affected by temperature in the VPI processing temperature range (~50 to 150 ^{o}C) can be used to test the equilibrium sorption amount of TMA in PMMA when temperature is changed after full infiltration. For example, once PMMA is fully infiltrated with TMA at 70 ^{o}C, will TMA desorb out as temperature is increased to 130 ^{o}C? Likewise, will additional TMA be absorbed into PMMA after the polymer is fully loaded with TMA at a higher temperature and then cooled down to a lower temperature while still maintaining sufficient TMA in the reaction chamber?

Applications of VPI: Because VPI is capable of creating hybrid materials from polymers of arbitrary shapes and sizes, applications can include post-processing of polymer-containing devices for additional chemical stability against harsh environments. VPI can also be used to improve dielectric properties among other things in polymers. The range of applications can be very wide for this new processing method.

REFERENCES

1. Sanchez, C.; Belleville, P.; Popall, M.; Nicole, L., Applications of advanced hybrid organic-inorganic nanomaterials: from laboratory to market. *Chem Soc Rev* **2011,** *40* (2), 696-753.
2. Lee, M. M.; Teuscher, J.; Miyasaka, T.; Murakami, T. N.; Snaith, H. J., Efficient Hybrid Solar Cells Based on Meso-Superstructured Organometal Halide Perovskites. *Science* **2012,** *338* (6107), 643-647.
3. Kuppler, R. J.; Timmons, D. J.; Fang, Q. R.; Li, J. R.; Makal, T. A.; Young, M. D.; Yuan, D. Q.; Zhao, D.; Zhuang, W. J.; Zhou, H. C., Potential applications of metal-organic frameworks. *Coordin Chem Rev* **2009,** *253* (23-24), 3042-3066.
4. Shekhah, O.; Liu, J.; Fischer, R. A.; Woll, C., MOF thin films: existing and future applications. *Chem Soc Rev* **2011,** *40* (2), 1081-1106.
5. Meek, S. T.; Greathouse, J. A.; Allendorf, M. D., Metal-Organic Frameworks: A Rapidly Growing Class of Versatile Nanoporous Materials. *Adv Mater* **2011,** *23* (2), 249-267.
6. Ciriminna, R.; Sciortino, M.; Alonzo, G.; de Schrijver, A.; Pagliaro, M., From Molecules to Systems: Sol-Gel Microencapsulation in Silica-Based Materials. *Chem Rev* **2011,** *111* (2), 765-789.
7. Dash, S.; Mishra, S.; Patel, S.; Mishra, B. K., Organically modified silica: Synthesis and applications due to its surface interaction with organic molecules. *Adv Colloid Interfac* **2008,** *140* (2), 77-94.
8. Ferguson, J. D.; Weimer, A. W.; George, S. M., Atomic layer deposition of Al2O3 films on polyethylene particles. *Chem Mater* **2004,** *16* (26), 5602-5609.
9. Lee, S. M.; Pippel, E.; Gosele, U.; Dresbach, C.; Qin, Y.; Chandran, C. V.; Brauniger, T.; Hause, G.; Knez, M., Greatly Increased Toughness of Infiltrated Spider Silk. *Science* **2009,** *324* (5926), 488-492.
10. Gregorczyk, K. E.; Pickup, D. F.; Sanz, M. G.; Irakulis, I. A.; Rogero, C.; Knez, M., Tuning the Tensile Strength of Cellulose through Vapor-Phase Metalation. *Chem Mater* **2015,** *27* (1), 181-188.
11. Tseng, Y. C.; Peng, Q.; Ocola, L. E.; Czaplewski, D. A.; Elam, J. W.; Darling, S. B., Etch properties of resists modified by sequential infiltration synthesis. *J Vac Sci Technol B* **2011,** *29* (6).
12. Obuchovsky, S.; Deckman, I.; Moshonov, M.; Peretz, T. S.; Ankonina, G.; Savenije, T. J.; Frey, G. L., Atomic layer deposition of zinc oxide onto and into P3HT for hybrid photovoltaics. *J Mater Chem C* **2014,** *2* (42), 8903-8910.
13. Lee, S. M.; Pippel, E.; Moutanabbir, O.; Gunkel, I.; Thurn-Albrecht, T.; Knez, M., Improved Mechanical Stability of Dried Collagen Membrane after Metal Infiltration. *Acs Appl Mater Inter* **2010,** *2* (8), 2436-2441.
14. Tseng, Y. C.; Peng, Q.; Ocola, L. E.; Elam, J. W.; Darling, S. B., Enhanced Block Copolymer Lithography Using Sequential Infiltration Synthesis. *J Phys Chem C* **2011,** *115* (36), 17725-17729.
15. Tseng, Y. C.; Peng, Q.; Ocola, L. E.; Czaplewski, D. A.; Elam, J. W.; Darling, S. B., Enhanced polymeric lithography resists via sequential infiltration synthesis. *J Mater Chem* **2011,** *21* (32), 11722-11725.
16. Segal-Peretz, T.; Winterstein, J.; Doxastakis, M.; Ramirez-Hernandez, A.; Biswas, M.; Ren, J. X.; Suh, H. S.; Darling, S. B.; Liddle, J. A.; Elam, J. W.; de Pablo, J. J.;

Zaluzec, N. J.; Nealey, P. F., Characterizing the Three-Dimensional Structure of Block Copolymers via Sequential Infiltration Synthesis and Scanning Transmission Electron Tomography. *Acs Nano* **2015,** *9* (5), 5333-5347.
17. Gong, B.; Peng, Q.; Jur, J. S.; Devine, C. K.; Lee, K.; Parsons, G. N., Sequential Vapor Infiltration of Metal Oxides into Sacrificial Polyester Fibers: Shape Replication and Controlled Porosity of Microporous/Mesoporous Oxide Monoliths. *Chem Mater* **2011,** *23* (15), 3476-3485.
18. Dandley, E. C.; Needham, C. D.; Williams, P. S.; Brozena, A. H.; Oldham, C. J.; Parsons, G. N., Temperature-dependent reaction between trimethylaluminum and poly(methyl methacrylate) during sequential vapor infiltration: experimental and ab initio analysis. *J Mater Chem C* **2014,** *2* (44), 9416-9424.
19. Akyildiz, H. I.; Lo, M.; Dillon, E.; Roberts, A. T.; Everitt, H. O.; Jur, J. S., Formation of novel photoluminescent hybrid materials by sequential vapor infiltration into polyethylene terephthalate fibers. *J Mater Res* **2014,** *29* (23), 2817-2826.
20. Choy, K. L., Chemical vapour deposition of coatings. *Prog Mater Sci* **2003,** *48* (2), 57-170.
21. Delhaes, P., Chemical vapor deposition and infiltration processes of carbon materials. *Carbon* **2002,** *40* (5), 641-657.
22. George, S. M., Atomic Layer Deposition: An Overview. *Chem Rev* **2010,** *110* (1), 111-131.
23. Parsons, G. N.; George, S. M.; Knez, M., Progress and future directions for atomic layer deposition and ALD-based chemistry. *Mrs Bull* **2011,** *36* (11), 865-871.
24. Puurunen, R. L., Surface chemistry of atomic layer deposition: A case study for the trimethylaluminum/water process. *J Appl Phys* **2005,** *97* (12).
25. Johnson, R. W.; Hultqvist, A.; Bent, S. F., A brief review of atomic layer deposition: from fundamentals to applications. *Mater Today* **2014,** *17* (5), 236-246.
26. Hatanpaa, T.; Ritala, M.; Leskela, M., Precursors as enablers of ALD technology: Contributions from University of Helsinki. *Coordin Chem Rev* **2013,** *257* (23-24), 3297-3322.
27. Profijt, H. B.; Potts, S. E.; van de Sanden, M. C. M.; Kessels, W. M. M., Plasma-Assisted Atomic Layer Deposition: Basics, Opportunities, and Challenges. *J Vac Sci Technol A* **2011,** *29* (5).
28. Kessels, W. M. M.; Putkonen, M., Advanced process technologies: Plasma, direct-write, atmospheric pressure, and roll-to-roll ALD. *Mrs Bull* **2011,** *36* (11), 907-913.
29. Kim, H.; Oh, I. K., Review of plasma-enhanced atomic layer deposition: Technical enabler of nanoscale device fabrication. *Jpn J Appl Phys* **2014,** *53* (3).
30. Sundberg, P.; Karppinen, M., Organic and inorganic-organic thin film structures by molecular layer deposition: A review. *Beilstein J Nanotech* **2014,** *5*, 1104-1136.
31. George, S. M.; Lee, B. H.; Yoon, B.; Abdulagatov, A. I.; Hall, R. A., Metalcones: Hybrid Organic-Inorganic Films Fabricated Using Atomic and Molecular Layer Deposition Techniques. *J Nanosci Nanotechno* **2011,** *11* (9), 7948-7955.
32. Hyde, G. K.; Scarel, G.; Spagnola, J. C.; Peng, Q.; Lee, K.; Gong, B.; Roberts, K. G.; Roth, K. M.; Hanson, C. A.; Devine, C. K.; Stewart, S. M.; Hojo, D.; Na, J. S.; Jur, J. S.; Parsons, G. N., Atomic Layer Deposition and Abrupt Wetting Transitions on Nonwoven Polypropylene and Woven Cotton Fabrics. *Langmuir* **2010,** *26* (4), 2550-2558.

33. Spagnola, J. C.; Gong, B.; Arvidson, S. A.; Jur, J. S.; Khan, S. A.; Parsons, G. N., Surface and sub-surface reactions during low temperature aluminium oxide atomic layer deposition on fiber-forming polymers. *J Mater Chem* **2010,** *20* (20), 4213-4222.
34. Padbury, R. P.; Jur, J. S., Effect of Polymer Microstructure on the Nucleation Behavior of Alumina via Atomic Layer Deposition. *J Phys Chem C* **2014,** *118* (32), 18805-18813.
35. Zhang, L. B.; Patil, A. J.; Li, L.; Schierhorn, A.; Mann, S.; Gosele, U.; Knez, M., Chemical Infiltration during Atomic Layer Deposition: Metalation of Porphyrins as Model Substrates. *Angew Chem Int Edit* **2009,** *48* (27), 4982-4985.
36. Lee, S. M.; Pippel, E.; Moutanabbir, O.; Kim, J. H.; Lee, H. J.; Knez, M., In Situ Raman Spectroscopic Study of Al-Infiltrated Spider Dragline Silk under Tensile Deformation. *Acs Appl Mater Inter* **2014,** *6* (19), 16827-16834.
37. Gong, B.; Spagnola, J. C.; Arvidson, S. A.; Khan, S. A.; Parsons, G. N., Directed inorganic modification of bi-component polymer fibers by selective vapor reaction and atomic layer deposition. *Polymer* **2012,** *53* (21), 4631-4636.
38. McClure, C. D.; Oldham, C. J.; Parsons, G. N., Effect of Al2O3 ALD coating and vapor infusion on the bulk mechanical response of elastic and viscoelastic polymers. *Surf Coat Tech* **2015,** *261*, 411-417.
39. Peng, Q.; Tseng, Y. C.; Darling, S. B.; Elam, J. W., A Route to Nanoscopic Materials via Sequential Infiltration Synthesis on Block Copolymer Templates. *Acs Nano* **2011,** *5* (6), 4600-4606.
40. Padbury, R. P.; Jur, J. S., Comparison of precursor infiltration into polymer thin films via atomic layer deposition and sequential vapor infiltration using in-situ quartz crystal microgravimetry. *J Vac Sci Technol A* **2014,** *32* (4).
41. Gong, B.; Spagnola, J. C.; Parsons, G. N., Hydrophilic mechanical buffer layers and stable hydrophilic finishes on polydimethylsiloxane using combined sequential vapor infiltration and atomic/molecular layer deposition. *J Vac Sci Technol A* **2012,** *30* (1), 01A156.
42. Berens, A. R.; Hopfenberg, H. B., Diffusion of Organic Vapors at Low Concentrations in Glassy Pvc, Polystyrene, and Pmma. *J Membrane Sci* **1982,** *10* (2-3), 283-303.
43. Budd, P. M.; McKeown, N. B.; Fritsch, D., Free volume and intrinsic microporosity in polymers. *J Mater Chem* **2005,** *15* (20), 1977-1986.
44. Barbari, T. A., Dual-mode free volume model for diffusion of gas molecules in glassy polymers. *J Polym Sci Pol Phys* **1997,** *35* (11), 1737-1746.
45. Shelby, J. E., *Introduction to glass science and technology*. 2nd ed.; Royal Society of Chemistry: Cambridge, 2005; p xvi, 291 p.
46. Sun, Y. J.; Padbury, R. P.; Akyildiz, H. I.; Goertz, M. P.; Palmer, J. A.; Jur, J. S., Influence of Subsurface Hybrid Material Growth on the Mechanical Properties of Atomic Layer Deposited Thin Films on Polymers. *Chem Vapor Depos* **2013,** *19* (4-6), 134-141.
47. Padbury, R. P.; Jur, J. S., Temperature-Dependent Infiltration of Polymers during Sequential Exposures to Trimethylaluminum. *Langmuir* **2014,** *30* (30), 9228-9238.
48. Pandey, P.; Chauhan, R. S., Membranes for gas separation. *Prog Polym Sci* **2001,** *26* (6), 853-893.
49. George, S. C.; Thomas, S., Transport phenomena through polymeric systems. *Prog Polym Sci* **2001,** *26* (6), 985-1017.

50. Leng, C. Z.; Losego, M. D., Vapor phase infiltration (VPI) for transforming polymers into organic-inorganic hybrid materials: a critical review of current progress and future challenges. *Mater Horiz* **2017,** *4* (5), 747-771.
51. Crank, J., *The Mathematics of Diffusion*. 2d ed.; Clarendon Press: Oxford, Eng, 1975; p 414.
52. Biswas, M.; Libera, J. A.; Darling, S. B.; Elam, J. W., New Insight into the Mechanism of Sequential Infiltration Synthesis from Infrared Spectroscopy. *Chem Mater* **2014,** *26* (21), 6135-6141.
53. Biswas, M.; Libera, J. A.; Darling, S. B.; Elam, J. W., Kinetics for the Sequential Infiltration Synthesis of Alumina in Poly(methyl methacrylate): An Infrared Spectroscopic Study. *J Phys Chem C* **2015,** *119* (26), 14585-14592.
54. Jur, J. S.; Spagnola, J. C.; Lee, K.; Gong, B.; Peng, Q.; Parsons, G. N., Temperature-Dependent Subsurface Growth during Atomic Layer Deposition on Polypropylene and Cellulose Fibers. *Langmuir* **2010,** *26* (11), 8239-8244.
55. Obuchovsky, S.; Shamieh, B.; Deckman, I.; Ankonina, G.; Frey, G. L., Harnessing ALD to directly map the morphology of organic photovoltaic bulk heterojunctions. *Sol Energ Mat Sol C* **2015,** *143*, 280-283.
56. Wilson, C. A.; Grubbs, R. K.; George, S. M., Nucleation and growth during Al2O3 atomic layer deposition on polymers. *Chem Mater* **2005,** *17* (23), 5625-5634.
57. Sinha, A.; Hess, D. W.; Henderson, C. L., Transport behavior of atomic layer deposition precursors through polymer masking layers: Influence on area selective atomic layer deposition. *J Vac Sci Technol B* **2007,** *25* (5), 1721-1728.
58. Padbury, R. P.; Jur, J. S., Systematic study of trimethyl aluminum infiltration in polyethylene terephthalate and its effect on the mechanical properties of polyethylene terephthalate fibers. *J Vac Sci Technol A* **2015,** *33* (1).
59. Lee, S. M.; Ischenko, V.; Pippel, E.; Masic, A.; Moutanabbir, O.; Fratzl, P.; Knez, M., An Alternative Route Towards Metal-Polymer Hybrid Materials Prepared by Vapor-Phase Processing. *Adv Funct Mater* **2011,** *21* (16), 3047-3055.
60. Akyildiz, H. I.; Padbury, R. P.; Parsons, G. N.; Jur, J. S., Temperature and Exposure Dependence of Hybrid Organic-Inorganic Layer Formation by Sequential Vapor Infiltration into Polymer Fibers. *Langmuir* **2012,** *28* (44), 15697-15704.
61. Gong, B.; Parsons, G. N., Quantitative in situ infrared analysis of reactions between trimethylaluminum and polymers during Al2O3 atomic layer deposition. *J Mater Chem* **2012,** *22* (31), 15672-15682.
62. Oldham, C. J.; Gong, B.; Spagnola, J. C.; Jur, J. S.; Senecal, K. J.; Godfrey, T. A.; Parsons, G. N., Encapsulation and Chemical Resistance of Electrospun Nylon Nanofibers Coated Using Integrated Atomic and Molecular Layer Deposition. *J Electrochem Soc* **2011,** *158* (9), D549-D556.
63. Mahoney, C. M., Cluster Secondary Ion Mass Spectrometry of Polymers and Related Materials. *Mass Spectrom Rev* **2010,** *29* (2), 247-293.
64. McCrackin, F. L.; Passaglia, E.; Stromberg, R. R.; Steinberg, H. L., Measurement of the thickness and refractive index of very thin films and the optical properties of surfaces by ellipsometry. *J Res Natl Inst Stan* **2001,** *106* (3), 589-603.
65. Albert, J. N. L.; Young, W. S.; Lewis, R. L.; Bogart, T. D.; Smith, J. R.; Epps, T. H., Systematic Study on the Effect of Solvent Removal Rate on the Morphology of

Solvent Vapor Annealed ABA Triblock Copolymer Thin Films. *Acs Nano* **2012,** *6* (1), 459-466.
66. Dandley, E. C.; Lemaire, P. C.; Zhu, Z. W.; Yoon, A.; Sheet, L.; Parsons, G. N., Wafer-Scale Selective-Area Deposition of Nanoscale Metal Oxide Features Using Vapor Saturation into Patterned Poly(methyl methacrylate) Templates. *Adv Mater Interfaces* **2016,** *3* (2).
67. Gregorczyk, K.; Knez, M., Hybrid nanomaterials through molecular and atomic layer deposition: Top down, bottom up, and in-between approaches to new materials. *Prog Mater Sci* **2016,** *75*, 1-37.
68. Gu, X. D.; Gunkel, I.; Russell, T. P., Pattern transfer using block copolymers. *Philos T R Soc A* **2013,** *371* (2000).
69. Hawker, C. J.; Russell, T. P., Block copolymer lithography: Merging "bottom-up" with "top-down" processes. *Mrs Bull* **2005,** *30* (12), 952-966.
70. Kim, H. C.; Park, S. M.; Hinsberg, W. D., Block Copolymer Based Nanostructures: Materials, Processes, and Applications to Electronics. *Chem Rev* **2010,** *110* (1), 146-177.
71. Peng, Q.; Tseng, Y. C.; Darling, S. B.; Elam, J. W., Nanoscopic Patterned Materials with Tunable Dimensions via Atomic Layer Deposition on Block Copolymers. *Adv Mater* **2010,** *22* (45), 5129-5133.
72. Mor, G. K.; Varghese, O. K.; Paulose, M.; Shankar, K.; Grimes, C. A., A review on highly ordered, vertically oriented TiO2 nanotube arrays: Fabrication, material properties, and solar energy applications. *Sol Energ Mat Sol C* **2006,** *90* (14), 2011-2075.
73. Vaha-Nissi, M.; Sundberg, P.; Kauppi, E.; Hirvikorpi, T.; Sievanen, J.; Sood, A.; Karppinen, M.; Harlin, A., Barrier properties of Al2O3 and alucone coatings and nanolaminates on flexible biopolymer films. *Thin Solid Films* **2012,** *520* (22), 6780-6785.
74. Han, Y. C.; Jeong, E. G.; Kim, H.; Kwon, S.; Im, H. G.; Bae, B. S.; Choi, K. C., Reliable thin-film encapsulation of flexible OLEDs and enhancing their bending characteristics through mechanical analysis. *Rsc Advances* **2016,** *6* (47), 40835-40843.
75. Guin, T.; Krecker, M.; Hagen, D. A.; Grunlan, J. C., Thick Growing Multi layer Nanobrick Wall Thin Films: Super Gas Barrier with Very Few Layers. *Langmuir* **2014,** *30* (24), 7057-7060.
76. Moshonov, M.; Frey, G. L., Directing Hybrid Structures by Combining Self-Assembly of Functional Block Copolymers and Atomic Layer Deposition: A Demonstration on Hybrid Photovoltaics. *Langmuir* **2015,** *31* (46), 12762-12769.
77. Michaels, A. S.; Barrie, J. A.; Vieth, W. R., Solution of Gases in Polyethylene Terephthalate. *J Appl Phys* **1963,** *34* (1), 1-12.
78. Meares, P., The Diffusion of Gases through Polyvinyl Acetate. *J Am Chem Soc* **1954,** *76* (13), 3415-3422.
79. Ghadimi, A.; Norouzbahari, S.; Mohammadi, T., Heat of Sorption of Gases in Glassy Polymers: Prediction via Applying Physical Properties of the Penetrants and Polymers. *J Chem Eng Data* **2017,** *62* (4), 1433-1439.
80. Koros, W. J.; Paul, D. R., Co2 Sorption in Poly(Ethylene-Terephthalate) above and Below Glass-Transition. *J Polym Sci Pol Phys* **1978,** *16* (11), 1947-1963.
81. Koros, W. J.; Smith, G. N.; Stannett, V., High-Pressure Sorption of Carbon-Dioxide in Solvent-Cast Poly(Methyl Methacrylate) and Poly(Ethyl Methacrylate) Films. *J Appl Polym Sci* **1981,** *26* (1), 159-170.

82. Laubengayer, A. W.; Gilliam, W. F., The Alkyls of the Third Group Elements. I. Vapor Phase Studies of the Alkyls of Aluminum, Gallium and Indium1. *J Am Chem Soc* **1941,** *63* (2), 477-479.
83. McCullough, J. P.; Messerly, J. F.; Moore, R. T.; Todd, S. S., TRIMETHYLALUMINUM: THERMODYNAMIC FUNCTIONS IN THE SOLID AND LIQUID STATES, 0-380°K.; VAPOR PRESSURE, HEAT OF VAPORIZATION, AND ENTROPY IN THE IDEAL GAS STATE1. *The Journal of Physical Chemistry* **1963,** *67* (3), 677-679.
84. Parsons, G. N.; Atanasov, S. E.; Dandley, E. C.; Devine, C. K.; Gong, B.; Jur, J. S.; Lee, K.; Oldham, C. J.; Peng, Q.; Spagnola, J. C.; Williams, P. S., Mechanisms and reactions during atomic layer deposition on polymers. *Coordin Chem Rev* **2013,** *257* (23-24), 3323-3331.
85. Ramesh, N.; Davis, P. K.; Zielinski, J. M.; Danner, R. P.; Duda, J. L., Application of Free-Volume Theory to Self Diffusion of Solvents in Polymers Below the Glass Transition Temperature: A Review. *J Polym Sci Pol Phys* **2011,** *49* (23), 1629-1644.
86. Leng, C. Z.; Losego, M. D., A physiochemical processing kinetics model for the vapor phase infiltration of polymers: measuring the energetics of precursor-polymer sorption, diffusion, and reaction. *Physical Chemistry Chemical Physics* **2018**.
87. Kahle, O.; Wielsch, U.; Metzner, H.; Bauer, J.; Uhlig, C.; Zawatzki, C., Class transition temperature and thermal expansion behaviour of polymer films investigated by variable temperature spectroscopic ellipsometry. *Thin Solid Films* **1998,** *313*, 803-807.
88. Kawana, S.; Jones, R. A. L., Character of the glass transition in thin supported polymer films. *Physical Review E* **2001,** *63* (2), 021501.

VITA

Collen Ziwei Leng was born in China and spent his early childhood in Beijing. In 1999, he and his parents moved to the United States for his father's career in academia. With both parents having backgrounds in the sciences and engineering, Collen quickly became fascinated in these fields as well. Besides getting perfect scores on nearly every math and science SAT subject test, he also accumulated boxes of medals and trophies from math and science competitions and helped his high school Science Olympiad team qualify for the national competition in 2008.

Although not graduating as valedictorian or salutatorian from his high school, Collen still joined the incoming freshman class of 2014 at Princeton, the best college in the US (Harvard is and will always be #2). Majoring in mechanical engineering, Collen developed a passion in renewable energy generation and storage. For his senior thesis, he worked under the guidance of Dr. Craig Arnold and investigated the mechanical properties of polymer separators used in lithium ion batteries. His research was published in two journal articles that have since been cited many times.

At Georgia Tech, Collen was one of the first two graduate students in Dr. Mark Losego's newly formed research group. The young team worked quickly to build up the labs and construct reactors for atomic layer deposition and vapor phase infiltration. Utilizing his background in mechanical engineering, Collen focused his Ph.D. thesis project on the kinetics of VPI and applied differential equations to describe the processing theory of metalorganic precursors infiltrating into polymers to create hybrid organic-inorganic materials. After graduation, Collen plans to continue making the world a slightly better place using his science and engineering expertise.